Title	Measurement of charged particle emission rates and energy spectra after muon nuclear capture in Aluminium
Author(s)	Wong, Ming Liang
Citation	大阪大学, 2018, 博士論文
Version Type	VoR
URL	https://doi.org/10.18910/69332
rights	
Note	

PhD Thesis

Measurement of charged particle emission rates and energy spectra after muon nuclear capture in Aluminium

Author:
WONG Ming Liang

Supervisor:
Prof. Yoshitaka KUNO

February 2, 2018

Abstract

Precision measurement of the spectrum and rate of charged particle emission especially protons after nuclear muon capture in aluminium is necessary for muon normalization using proton counting in muon to electron conversion experiments like the COMET Phase-I experiment. This method compliments the muonic x-ray measurements and is less prone to being blinded by the beam flash. These protons also contribute to the noise signal hits of the COMET drift chamber as those with energy more than 2.5 MeV could reach the detector and cause difficulty in observing signal tracks created from the 105 MeV/c electrons.

In order to achieve those goals, the AlCap R2015b experiment was performed. We measured low energy charged particle emissions after nuclear muon capture in aluminium over a total measurement period of 25.7 hours. The emission rate per muon capture for protons is $3.33 \pm 0.20\%$, for deuterons $0.74 \pm 0.05\%$, and for tritons $0.15 \pm 0.02\%$. A total of 1.03×10^8 muons from the πE1 beamline in PSI, Switzerland were stopped in $100\,\mu$m thick aluminium target. The 2p-1s and 3p-1s transition signatures of the stopped muons were measured with a high purity germanium detector. The charged particle convoluted energy spectra measured by two counter telescopes are deconvoluted using the Bayesian iterative method. This work also confirmed the previous result (AlCap 2013) of the proton emission rate of $3.5 \pm 0.2\%$ besides reporting the first low energy ($< 18\,$MeV) measurements of deuteron and triton emission rates and energy spectra from aluminium.

Contents

List of Figures

List of Tables

Chapter 1

Introduction

1.1 Issues with the standard model

The Standard Model(SM) has been largely successful in explaining the particles and their interactions that we have observed so far. As recently as five years ago in 2012 the Higgs boson was discovered by the largest particle accelerator in history and it is the missing piece that was needed to complete the SM. The standard model is not without its problems, however as the history of science has showed us that our theories and models are always incomplete and current theories are always superseded with more general and better ones. There are still many unexplained physical phenomena, for example the observation of dark matter, dark energy, non-convergence of running couplings, naturalness problem, and particle-antiparticle asymmetry amongst others. Several new physics theories have been proposed to solve these problems, some of them are Supersymmetry(SUSY), extra-dimensions and Grand Unified Theories(GUT). These theories are being tested in the 14 TeV high energy particle accelerator in CERN. But even with the high collision energy of the Large Hadron Collider(LHC) we have yet to see any hint of Beyond Standard Model(BSM) physics. An alternative way to that would be to increase the intensity of the particle beam to probe rare processes that would provide the clue for (BSM physics. This involves building megawatt particle accelerators and highly sensitive particle detectors.

1.2 Lepton flavour violation

Leptons are part of fermions which make up all of known matter in the universe. They may be assigned lepton flavour quantum numbers as shown in Table.1.1.

This assignment is useful as lepton number is a conserved quantity in SM. For

	L_e	L_μ	L_τ
(e, ν_e)	+1	0	0
(μ, ν_μ)	0	+1	0
(τ, ν_τ)	0	0	+1

Table 1.1: Lepton flavour quantum number assignment. Antileptons gain a minus sign.

example in muon proton interactions, $\mu + p \rightarrow n + \nu_\mu$, L_μ is equal to 1 on both the left and right sides of the equation.

In 1998, neutrino oscillation was observed in the 33.0 kiloton Super-Kamiokande detector[5] after a total measurement time of 535 days. The result showed that lepton flavour is not a conserved quantum number. This also means that neutrinos are not massless as assumed by the SM, but their absolute masses are also not known but are thought to be below 0.120 eV. The minimal SM could not explain these observations and it had to be modified to accomodate these new results.

1.3 Charged lepton flavour violation

Neutral lepton flavor quantum number is no longer conserved and it begs the question whether charged lepton flavour is also not a conserved quantity. A classic example of Charged Lepton Flavour Violation(CLFV) is the reaction $\mu^+ \rightarrow e^+ + \gamma$ where the quantum numbers L_μ and L_e are not equal. So far, CLFV has yet to be observed although efforts to measure it started much earlier. CLFV is effectively forbidden in the SM as it is strongly suppressed with a branching ratio of $\mathcal{O}(10^{-54})$[6] in the neutrino mixing version of the model. Equation.1.1 describes the branching ratio for the above $\mu^+ \rightarrow e^+ + \gamma$ in SM.

$$B(\mu \rightarrow e\gamma) = \frac{3\alpha}{32\pi} \left| \sum_{i=2,3} U^*_{\mu i} U_{ei} \frac{\Delta m^2_{i1}}{M^2_W} \right|^2 < 10^{-54} \tag{1.1}$$

where U_{li} are elements in the neutrino mixing matrix, α the fine structure constant, Δm^2_{i1} the mass difference between the oscillating neutrinos. SUSY, extra-dimensions and little Higgs models predict CLFV processes at rate accessible with current techniques. The observation of CLFV events at currently accessible branching ratios will provide strong evidence for BSM physics, while a null result will strongly constrain theory parameters. The SM and SUSY loop diagrams for CLFV are shown in Figure.1.1. The $\Delta m^2_{\widetilde{\mu}\widetilde{e}}$ term represents the magnitude of the off-diagonal matrix element for slepton mixing.[7].

1.4 Muon to electron conversion

In the SM, muons typically decay into electrons, anti electron neutrinos and muon neutrinos in free-field

$$\mu^- \rightarrow e^- + \bar{\nu}_e + \nu_\mu \tag{1.2}$$

or if they are in the nuclear-field, transmutes a proton and a free muon neutrino.

$$\mu^- + N(A, Z) \rightarrow N(A, Z-1) + \nu_\mu \tag{1.3}$$

Both of these processes produce neutrinos and conserves lepton flavour quantum number. Neutrinoless muon to electron conversion however, does not.

$$\mu^- + N(A, Z) \rightarrow e^- + N(A, Z); \tag{1.4}$$

The neutrinoless muon to electron conversion process has a sensitivity to BSM physics from both dipole (loop) and non-dipole interactions. This is in contrast

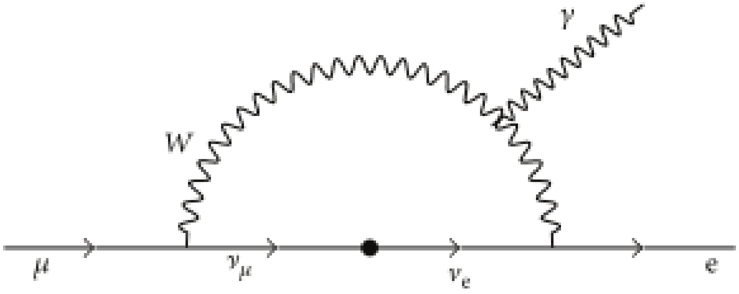

(a) $\mu^+ \rightarrow e^+ + \gamma$ in SM

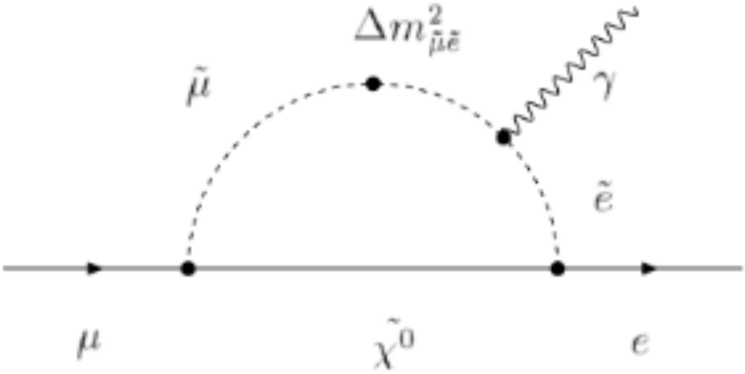

(b) $\mu^+ \rightarrow e^+ + \gamma$ in SUSY

Figure 1.1: Possible processes that might lead to $\mu^+ \rightarrow e^+ + \gamma$ in both the SM and SUSY.

to the $\mu \to e\gamma$ process which is only sensitive to dipole interactions. In simple BSM dipole interactions [6] the rate of the $\mu \to e\gamma$ process is 389 times that of the neutrinoless muon to conversion process (for an aluminium target). An effective Lagrangian describing both of these contributions was developed in [8] where a parameter, κ, defines the relative strength of the dipole and non-dipole interactions and Λ is the effective scale of new physics in the tree diagram.

$$\mathcal{L} = \frac{m_\mu}{(\kappa+1)\Lambda^2}\bar{\mu}_R\sigma_{\mu\nu}e_L F^{\mu\nu} + \frac{\kappa}{(\kappa+1)\Lambda^2}m\bar{u}_L\gamma_\mu e_L(\bar{q_L}\gamma^\mu q_L) \tag{1.5}$$

The current MEG and SINDRUM[9] limits on κ and Λ are shown in Figure 1.2 and highlight the high effective (tree level) energy scales probed. In most BSM models the mass scales probed, *e.g.* when the tree-level BSM operators are loop-suppressed by a factor of $1/16\pi^2$, are typically in the TeV range.

1.5 Past experiments of CLFV

Right after the discovery of the muon, it was believed that it decays into an electron and a neutral particle. Also if the muon were simply a heavy electron it would also decay into an electron and a γ ray. The first search for $\mu^+ \to e^+\gamma$ was made by Hincks and Pontecorvo in 1947 using cosmic-ray muons. Its negative result set an upper limit on the branching ratio to less than 10%. In 1948, the continuous spectrum of electrons was established, suggesting a three-body decay giving rise to a final state of an electron accompanied by two neutral particles. Soon afterwards, the search for the process of neutrinoless muon nuclear capture ($\mu N \to eN$, where N is a nucleus capturing the muon) was also carried out, but with a negative result.

After the discovery of parity violation, it was suggested that the weak interaction took place through the exchange of charged intermediate vector bosons. In 1958, Feinberg pointed out that the intermediate vector boson, if it exists, would lead to $\mu^+ \to e^+\gamma$ at a branching ratio of $\mathcal{O}(10^{-4})$[10]. The absence of any experimental observation of the $\mu^+ \to e^+\gamma$ process with $B(\mu^+ \to e^+\gamma) < 2 \times 10^{-5}$ led directly to the two-neutrino hypothesis in which the neutrino coupled to the muon differs from that coupled to the electron, and the $\mu^+ \to e^+\gamma$ process is forbidden. The two-neutrino hypothesis was verified experimentally at Brookhaven National Laboratory (BNL) by observing muon production but not electron production from the scattering of neutrinos produced from pion decays[11]. This introduced the concept of a separate conservation law for individual lepton flavors, electron number (L_e) and muon number (L_μ) as introduced in an earlier section.

The SINDRUM II experiment in 2013 obtained the upper limits to the $\mu - e$ conversion for the Ti and Au nuclei. For Ti, the upper limit for conversion is 6.1×10^{-13} and for Au, 7×10^{-13} both with 90% confidence levels. The MEG experiment which ran from 2009–2013 stopped a total of 7.5×10^{14} muons on target reported an upper limit to the branching ratio of the $\mu^+ \to e^+\gamma$ decay to be at 4.2×10^{-13} with 90% confidence level[12]. Both experiments ran in PSI.

1.6 COMET experiment

In the advent of stronger, more intense muon beams at the order of 10^{18} muons per year at the (J-PARC) in Tokai, Japan, the COherent Muon to Electron Transi-

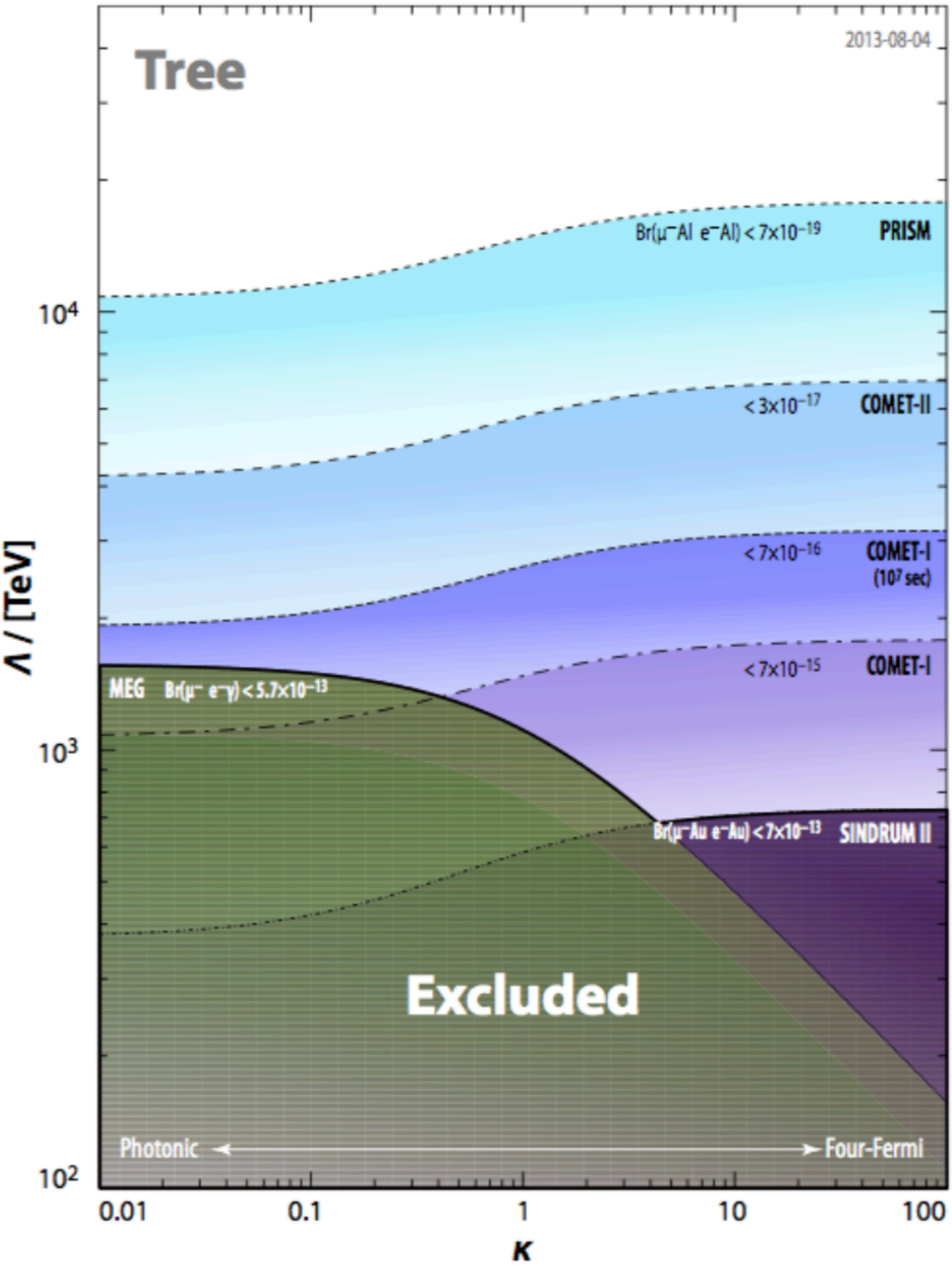

Figure 1.2: Past and future experimental limits of $\mu - e$ conversion experiments exploring the new physics Λ energy scale as a function of κ.

tion(COMET) experiment was conceived as an attempt to obtained better physics sensitivity compared to the previous experiment in an attempt to discover CLFV via neutrinoless muon to electron conversion. In a nutshell, the observation of a statistically significant amount of the 105 MeV signal electrons from muon conversion would provide what COMET is searching for. The conversion electron is monoenergetic, and its energy, $E_{\mu-e}$, is given by

$$E_{\mu-e} = m_\mu - B_\mu - E_{recoil} \tag{1.6}$$

where m_μ is the muon mass, and B_μ is the binding energy of the 1s-state muonic atom. E_{recoil} is the nuclear recoil energy. The COMET Phase-I experiment will use aluminium as a muon stopping material, for which $E_{\mu-e}$ is 104.97 MeV. Since the initial and final nuclei are the same, the transition to the ground state in the final nucleus is a coherent process, so the transition rate is enhanced, roughly scaling with the number of nucleons in the nucleus. This ultimate sensitivity goal is a factor of about 10,000 better than the current experimental limit of $B(\mu^- + Au \rightarrow e^- + Au) \leq 7 \times 10^{-13}$ from SINDRUM-II at PSI[9]. A schematic layout of the COMET experiment is shown in Figure1.3. The experiment will be carried out in the Hadron Hall of J-PARC using a bunched 8GeV proton beam that is slow-extracted from the J-PARC main ring. Muons will be produced from the pions produced after collisions of the 8 GeV proton beam with a production target. The yield of low momentum muons transported to the experimental area is enhanced using a pion capture superconducting solenoid surrounding the proton target in the pion capture section in Figure1.3. Muons are momentum- and charge-selected using curved superconducting solenoids in the muon transport section, before being stopped in an aluminium target. The signal electrons from the muon stopping target are detected by instrumentation in the detector section.

COMET Phase-I aims for a Single Event Sensitivity(SES) of 3×10^{-15} where the SES is given by

$$B(\mu^- + \text{Al} \rightarrow e^- + \text{Al}) = \frac{1}{N_\mu \cdot f_{cap} \cdot f_{gnd} \cdot A_{\mu-e}} \tag{1.7}$$

where N_μ is the number of muons stopped in the aluminium target, $f_{cap} = 0.61$ is the fraction of muons captured by the nucleus, $f_{gnd} = 0.9$ [13] the fraction of $\mu - e$ conversion to the nuclear ground state and $A_{\mu-e} = 0.041$ is the net signal acceptance. The achievement of the above stated SES requires $N_\mu = 1.5 \times 10^{16}$ or total number of Protons On Target(POT) of 3.2×10^{19}. With a proton beam current of 0.4μA, a total of 146 days is required. The number of stopped muons during the total run time is required in order to determine the branching ratio of the muon to electron conversion process. This muon normalization method has not been finalized yet, as there are several ways with their advantages and disadvantages. A viable option was to measure the total x-ray photons from the muonic aluminium transition from the 2p to the 1s state.

1.6.1 Muon stopping target

Since the signal process is coherent, its cross section grows roughly as the square of the number of nucleons until the muon is contained almost completely within the nucleus, at which point the rate levels off. It is therefore desirable to use a high-Z

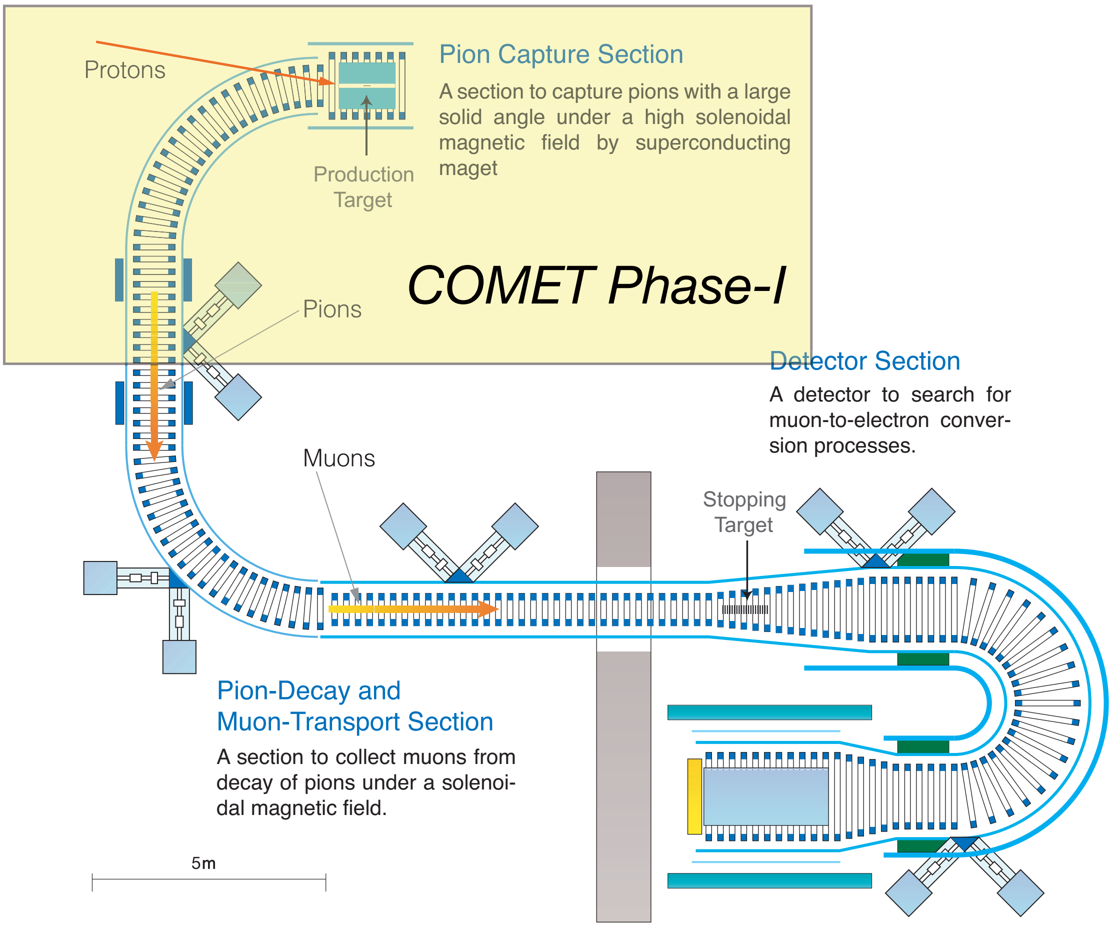

Figure 1.3: Schematic layout of COMET (Phase-II) and COMET Phase-I (not to scale).

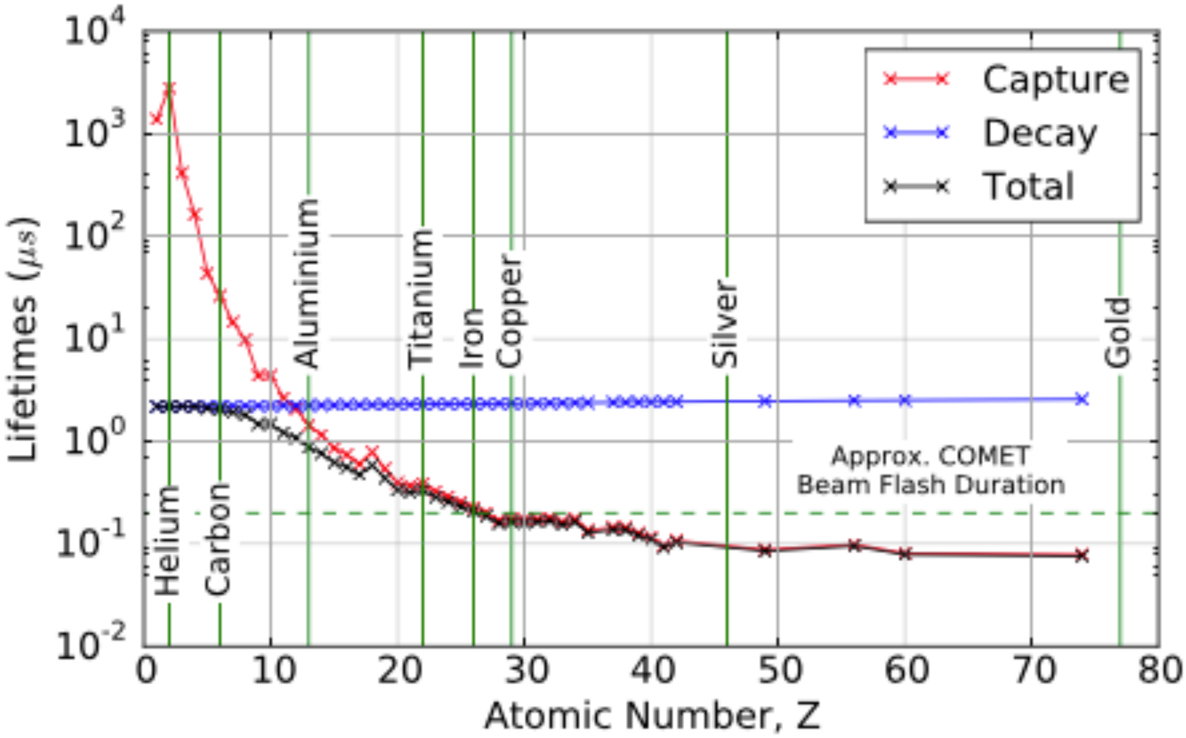

Figure 1.4: Lifetimes of muonic atoms.

target in order to increase the probability of conversion and indeed SINDRUM-II used both lead and gold targets, with its most stringent limit set on a gold target. However, as the nucleus gets larger, the lifetime of the muonic atom falls steeply due to the increase in the nuclear capture rate. This is illustrated in Figure.1.4 where it can be seen that for elements heavier than Fe ($Z > 26$) the muon lifetime is less than 200 ns. Accordingly, aluminium is considered for COMET Phase-I since it achieves this balance of muon lifetime and the increase of conversion probability.

1.6.2 Cylindrical detector

The Cylindrical Detector(CyDet) consists of a Cylindrical Drift Chamber(CDC), trigger hodoscope and a detector solenoid. It is the main detector system for COMET Phase-I. The CDC is a low mass gaseous detector using He:iC_4H_{10} 90:10 mix with 20 layers of sense wires. Its low mass would help to reduce instances of multiple scattering that would reduce the momentum resolution. It is connected to the muon source via curved superconducting solenoid that selects muons with the right momentum that can hit the aluminium stopping targets located right in the center of the CDC. A gain of more than 1850 V is applied to the sense and field wires. In total, the intrinsic momentum resolution of the CDC of about 200 keV can be achieved. A high momentum resolution is crucial for signal and background separation. The trigger hodoscope is located on both the upstream and downstream inner wall of the CDC provides the trigger for signal-like events. Tracks from charged particles that are positively identified by the trigger hodoscope will be recorded.

A key feature of COMET is to use pulsed beam structure that allows for elim-

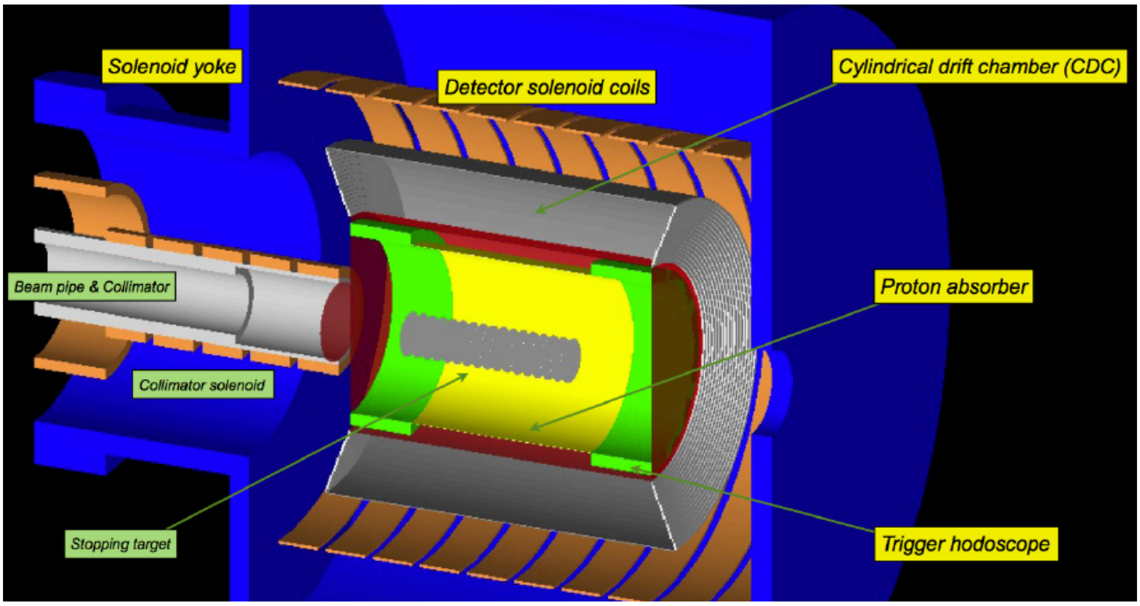

Figure 1.5: Cutout of the CDC.

ination of prompt beam backgrounds by looking only at tracks that arrive after the beam pulse. The CDC is capable of withstanding the large incoming flux of gammas, neutrons and charged particles that come right after the beam flash. The time window for the measurement of electrons from $\mu - e$ conversion in COMET will start 700 ns after the beam spill.

1.6.3 Intrinsic physics backgrounds

Muons trapped in the Coulomb field of the aluminium atom is known to undergo two main decay paths, (DIO) and nuclear muon capture. Muon from DIO is a Michel decay, $\mu^- + N \to e^- + \nu_\mu + \bar{\nu}_e + N$, of muons that are bound in a muonic atom by the Coulomb potential of the nucleus. In a free muon decay the electron momentum is shared with the neutrinos, but in atomic orbit the nuclear recoil from the Michel decay allows the electron to carry much more energy. This causes the maximum energy of the e^- to exceed the end point energy of the ordinary Michel decay energy at rest of 52.8 MeV, extending it to the vicinity of the $\mu - e$ conversion signal.

The energy spectrum of protons emitted after negative muon capture in aluminum has been measured by the AlCap experiment at PSI, a collaboration between COMET and Mu2e. A preliminary analysis shows that the proton emission probability per muon capture in aluminum in the energy range of 4 to 8 MeV is 0.017. Fitting the measured spectrum and extrapolating the fitted function gives a total emission rate per muon capture of 0.035. The proton emission rate eliminated the need for a proton absorber for the inner wall of the CDC since the rates are much lower than previously estimated using the emission rate of silicon. These backgrounds limit the maximal usable beam intensity of the COMET Phase-I experiment since they occupy the detector hit cells.

Chapter 2

Nuclear muon capture

2.1 Muonic atom formation

Before negative muons can be captured by the nucleus of any atom, it must first be in the orbit of an atom, or rather the muonic K-shell in order to have the highest possibility of interacting with a proton in the nucleus. An early description of the muon being trapped in the Coulomb field of an atom or stopped in an atom is described in [14]. Starting from free muons travelling with kinetic energy greater than the ionization energy of the atom, it scatter and slow down in the material until its kinetic energy is low enough to start orbiting around the atom. Typically, the muon first occupies the n=14 state displacing the ground state electron of the atom. It quickly cascades down to the muonic K-shell in femtosecond timescales. During this time, multiple x-ray photons and probably some Auger electrons are emitted. The muon orbital radius is 205 times smaller compared to that of the electron with the same orbital quantum number since it is about 205 times more massive. This results in a higher muon nuclear wavefunction overlap and a very good opportunity for using the muon as a probe for studying nuclear properties such as nuclear moments and charge distribution.

2.2 Nuclear capture

Muons can decay, be captured by the nucleus or it can undergo conversion into electrons. Muon conversion to electrons are not observed yet but is the current subject of cutting edge research in particle physics, and as described in the previous chapter, will provide hints to BSM physics. Muon decay and nuclear capture however, are observed and they are two competing processes whose rates depends on the atomic mass, A. For aluminium, th decay rate is 39% and 61% for capture [15] with a muonic lifetime of 864 ± 2ns[16]. The capture rate increases if a heavier nuclei is considered as shown in Table.2.1. It is calculated based on the effects of the nuclei on the lifetime of the muon in the atom.

$$\Lambda_t = \Lambda_c + Q\Lambda_d \tag{2.1}$$

where Λ_t is the total rate, Λ_c the capture rate, Λ_d the decay rate and finally the Huff factor Q[17]. The capture rate can be compared to the Primakoff formula[18],

$$\Lambda_c(A, Z) = Z_{\text{eff}}^4 X_1 \left[1 - X_2 \left[\frac{A - Z}{2A}\right]\right] \tag{2.2}$$

μ Z(Z_{eff})	Element	Mean lifetime	Capture rate ($\times 10^3$)ns	Huff factor
6(5.72)	^{12}C	2026(2)	3.9(5)[16]	1.00
13(11.48)	^{27}Al	864(2)	705(3)[16]	0.993
14(12.22)	^{28}Si	767(2)	850(3)[16]	0.992
26(10.59	^{56}Fe	206(1)	441(2)[16]	0.975
82(34.18)	^{208}Pb	74.9(4)	12.98(10)[20]	0.844

Table 2.1: Muonic lifetime and capture rates for selected nuclei which are interesting for the AlCap experiment.

Element	Average multiplicity
^{27}Al	1.262(59)
^{28}Si	0.864(72)
^{56}Fe	1.125(41)
^{208}Pb	1.709(66)

Table 2.2: Average neutron emission of after muon capture.

where $X_1 = 170\text{s}^{-1}$ is the muon capture rate in hydrogen and $X_2 = 3.125$ which includes contributions from the Pauli exclusion principle in nuclear environments. Essentially the X_2 is a measure of difficulty for muons to convert a proton to a neutron when there are many neutrons occupying lower energy levels. The effective charge, Z_{eff} was calculated from [19] where the nuclear charge distribution of a muonic atom was considered. Neutrons and other charged particles can be knocked out of the nucleus after nuclear capture, creating prompt gamma rays as well as delayed gamma rays from activation. Table.2.1 shows muon lifetimes and capture rates in selected atoms which are interesting to the AlCap experiment, specifically because those elements exists in the experimental setup.

2.3 Neutron emission

Neutron emission is a mode of radioactive decay in which one or more neutrons are ejected from a nucleus. Equation.2.3 is an example of single neutron emission. For light nuclei, most neutron gain enough kinetic energy after muon capture to escape the nucleus.

$$\mu^- + N(A,Z) \to \nu_\mu + n + N(A-1, Z-1) \tag{2.3}$$

It occurs in the most neutron-rich/proton-deficient nuclei, and also from excited states of other nuclei as in photoneutron emission and beta-delayed neutron emission. As a consequence of the Pauli exclusion principle, nuclei with an excess of protons or neutrons have a higher average energy per nucleon. Nuclei with a sufficient excess of neutrons have a greater energy or Q value than the combination of a free neutron and a nucleus with one less neutron, and therefore can decay by neutron emission. As only a neutron is lost by this process the number of protons remains unchanged, and an atom does not become an atom of a different element, but a different isotope of the same element.

After muon capture, some which acquire sufficient energy are directly emitted via the direct emission process. Others go through an indirect process where the energy of the capture muonis transferred statistically to all nucleons. The total energy that is transferred is 5.2 MeV provided the initial capture proton is at rest. The energy from muon capture is statistically shared with all the nucleons to form an intermediate compound nucleus. The nucleus would then try to lose neutrons or charged particles or both in an attempt to reach an equilibrium state. For light and intermediate nuclei $N < 40$ there is a higher chance of charged particle emission. For heavy nuclei, neutron emission would dominate since the Coulomb barrier reduces the chances of charged particles from escaping.

2.4 Proton emission

Proton emission is a rare type of radioactive decay in which a proton is ejected from a nucleus. Proton emission can occur from high-lying excited states in a nucleus following a beta decay, in which case the process is known as beta-delayed proton emission, or can occur from the ground state (or a low-lying isomer) of very proton-rich nuclei, in which case the process is very similar to alpha decay.

$$^{A}_{Z}X_N \rightarrow ^{A-1}_{Z-1} Y_N + p \tag{2.4}$$

For the reaction described in Equation.2.4 to happen, the Q-value must be positive, which means that the proton acquires sufficient energy to escape the strong nuclear force creating a daugther nuclei that is has lower binding energy per nucleon, thus more stable. The proton however, might still be trapped inside the Coulomb potential and would have to tunnel through that similar to alpha decay. For a proton to escape a nucleus, the proton separation energy must be negative - the proton is therefore unbound, and tunnels out of the nucleus in a finite time. Proton emission is not seen in naturally occurring isotopes; proton emitters can be produced via nuclear reactions, usually using linear particle accelerators.

Although prompt proton emission was observed from an isomer in ^{53}Co as early as 1969[21], no other proton-emitting states were found until 1981, when the proton radioactive ground states of ^{151}Lu[22] and ^{147}Th[23] were observed at experiments at the GSI in West Germany. Research in the field flourished after this breakthrough, and to date many isotopes have been found to exhibit proton emission [24] [25]. The study of proton emission has aided the understanding of nuclear deformation[26], masses and structure, and it is a wonderfully pure example of quantum tunneling.

In 2002, the simultaneous emission of two protons predicted by Goldansky[27] was observed from the nucleus ^{45}Fe in experiments at GSI[28] and GANIL[29]. In 2005 it was experimentally determined (at the same facility) that ^{54}Zn can also undergo double proton decay[30].

Muon induced charged particle emission started early in 1953, where Morinaga and Fry [31] studied muon tracks obtained in photographic emulsion after muon stops in AgBr. Sobottka and Wills [32] stopped muons in a Si(Li) detector. The proton emission rate was measured to be 15% which is a lot higher than aluminium. The spectrum is given in Figure.2.2 which has been corrected for electrons from muon decay and for protons which escaped. The spectrum shape is fitted with an empirical model given in Equation.2.5 with parameters, $A = 0.105\text{MeV}^{-1}$, T_{th} =1.4 MeV, $\alpha =$ 1.328 and T_0 =3.1 MeV. The function rises from the threshold, T_{th}, its rising edge is governed by the parameter α. The exponential decay component, T_0 dominates after reaching the peak value. Protons with higher energies are technically easier

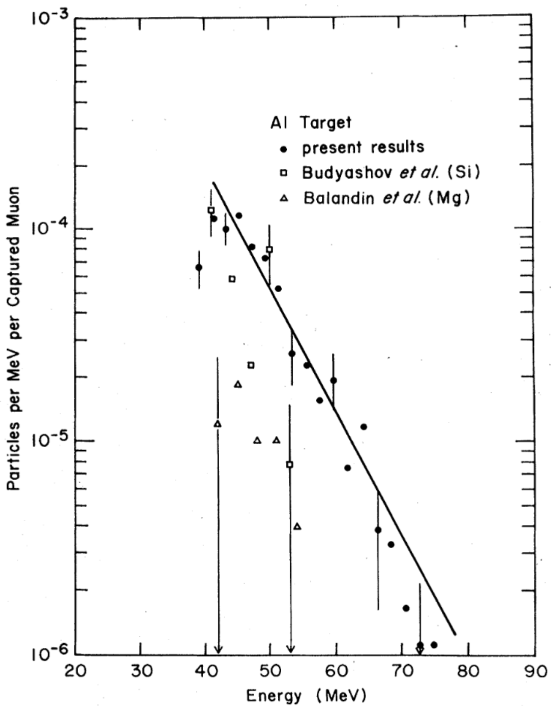

Figure 2.1: Charged particle yield after muon capture in aluminium shown as black circles. The square and triangle data points are from [1] and

to measure, but because of the much lower rate, they can only be studied at meson facilities. Krane[33] measured proton emission from aluminium, copper and lead in the energy range above 40 MeV and found a consistent exponential shape in all targets. The integrated yields above 40 MeV are in the 10^{-4}-10^{-3} range, a minor contribution to total proton emission rate.

Later in 1971, the deuteron spectrum for ^{28}Si was reported[1].

$$p(T) = A\left(1 - \frac{T_{th}}{T}\right)^{\alpha} e^{-\frac{T}{T_0}} \tag{2.5}$$

Theoretical attempts at understanding the charged particle emission spectra have been done where the contributions from the weak interaction are neglected. This approximation was done by considering the nucleons as a Fermi gas at different nuclear temperatures [34] for proton and alpha emissions. Following the Boltzmann distribution, particles in the nucleus gaining enough energy would evaporate leaving behind a more stable 'cooler' daughter nuclei. However, this process does not account for the whole proton energy spectrum so some form of direct emission may also produce more proton emission, therefore Singer [35] suggested a model of two-proton cluster muon capture process that explains the statistical calculation discrepancy.

This later work, using activation data[3] provided the ratio of charged particle emission, (μ, p), (μ, pn), $(\mu, p2n)$, $(\mu, p3n)$ = (1:6:4:4) as shown in Figure.2.3. It is plot again the classical Coulomb barrier,

$$V = \frac{zZe^2}{r_0\sqrt{A} + \rho} \tag{2.6}$$

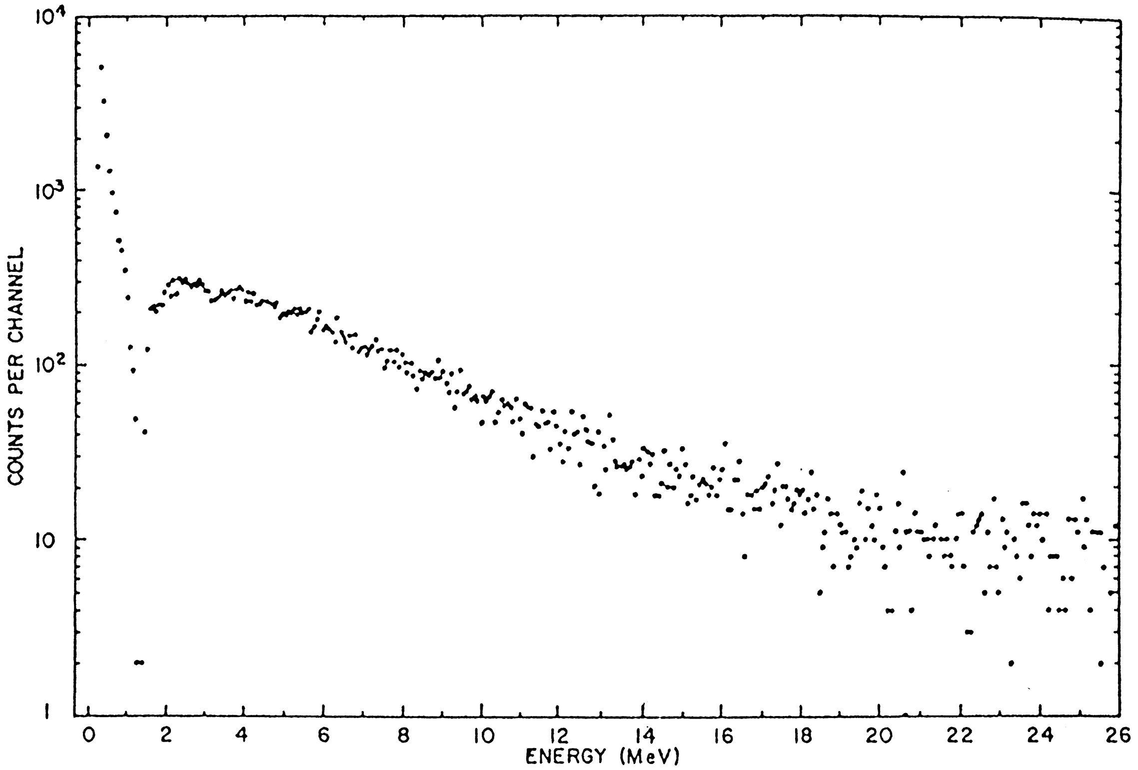

Figure 2.2: Charged particle energy spectrum after muon capture in Silicon

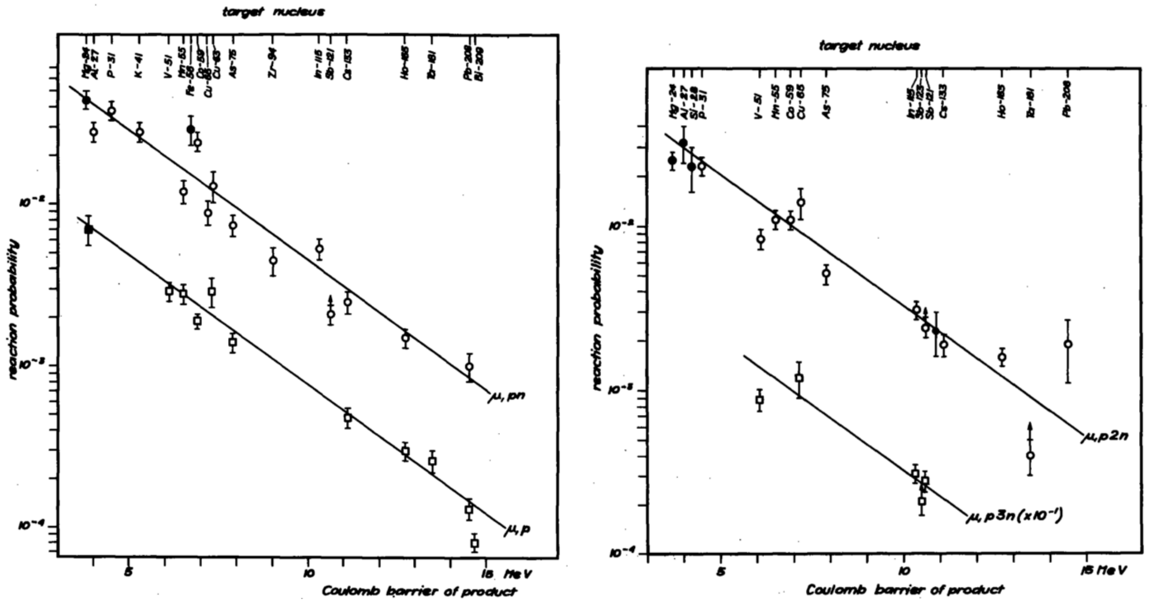

(a) (μ^-, p) and (μ^-, pn) reaction probabilities (b) $(\mu^-, p2n)$ and $(\mu^-, p3n)$ reaction probabilities

Figure 2.3: Probabilities for charged particle reactions including aluminium.

Element	$(\mu, \nu p)$	$\Sigma(\mu, \nu p(xn))$
^{27}Al	3.5(2)	28(4)
^{28}Si	53(10)	150(30)
^{208}Pb	0.13(2)	3.0(0.8)

Table 2.3: Proton emission probabilities (10^{-3}) per muon capture[2, 3, 4].

For low energy proton emission, the previous work done by AlCap[2, 36] reports a 3.5% total emission rate with a peak at 3.7 MeV and a exponential constant at 2.6 MeV.

2.4.1 Further study of aluminium capture rate

As mentioned, protons from muon capture on aluminium might cause a very high rate in the COMET Phase-I CDC. The detector is designed to accept particles with momenta in the range of 75 to 120 MeV. Protons with kinetic energies larger than 2.5 MeV could hit the CDC. Such events are troublesome due to their large energy deposition. Deuterons, tritons and alphas at the same momentum are not of concern because they have lower kinetic energy compared with protons and higher stopping power, thus are harder to escape the muon stopping target.

The previous AlCap which reported a rate of 3.5% eliminated the need for a thin, low-Z proton absorber that could have degraded the momentum resolution. The rate is low enough such that it is no longer a major problem. Now, with finer knowledge of the proton emission rate could be used to get a number of stopped muons in the COMET Phase-I muon stopping target.

Chapter 3

AlCap experiment

3.1 Introduction

The AlCap experiment is a join collaboration between Mu2E and COMET, which aims to measure

- emitted charged particle rates and energy spectra from as low as 2.5 MeV with a 5-10% resolution
- x-ray and gamma spectra and the relative intensities in the various peaks
- emitted neutron rates and spectra from 1 to 10 MeV.

after muon nuclear capture in ^{27}Al, ^{28}Si and ^{50}Ti.

The experiment was organized into three separate work packages,

- Protons emitted after nuclear muon capture in the stopping target dominate the single-hit rates in the tracking chambers for both the Mu2e and COMET Phase-I experiments. It was planned to measure both the total rate and the energy spectrum to a precision of 5% down to proton energies of 2.5 MeV.
- A germanium detector will be used to measure x-rays from the muonic atomic cascade, in order to provide the muon-capture normalization for proton emission after muon capture, and is essential for very thin stopping targets. It is also the primary method proposed for calibrating the number of muon stops in the Mu2e and COMET experiments. Two additional calibration techniques will also be explored; detection of delayed gamma rays from nuclei activated during nuclear muon capture, and measurement of the rate of photons produced in radiative muon decay. The first of these would use a germanium detector and the second a NaI detector. The NaI calorimeter will measure the rate of high energy photons from radiative muon capture (RMC), electrons from muon decays in orbit (DIO), and photons from Radiative Muon Decay(RMD), as potential background sources for the conversion measurement. As these rates are expected to be extremely low near the conversion electron energy, only data at energies well below 100 MeV will be obtained.
- Neutron rates and spectra after capture in Al and Ti are not well known. In particular, the low energy region below 10 MeV is important for determining backgrounds in the Mu2e/COMET detectors and veto counters as well

as evaluating the radiation damage to electronic components. Carefully calibrated liquid scintillation detectors, employing neutron-gamma discrimination and spectrum unfolding techniques, will measure these spectra. This neutron measurement will attempt to obtain spectra as low or lower than 1 up to 10 MeV.

Previous work measuring the proton energy spectra of aluminium, copper and lead was done in 1979. The results for aluminium were obtained for energy range above 40 MeV was $(1.38 \pm 0.09) \times 10^{-3}$ per muon capture [33]. Protons that have kinetic energy of 5 MeV would share the same trajectory as the 105 MeV conversion electron and introduce uncertainties. Similarly, 3 MeV deuterons would also create such noise hits in the COMET CDC. Charged particle emission rates would be important in estimating the systematic uncertainties of the COMET/Mu2E experiments. The normalization method involves the measurement of photon emission spectra, which includes muonic x-rays, capture gamma-rays and gamma rays from activated nuclei. The primary suggested method to obtain the normalization is to use the muonic aluminium K-α x-ray transition at an energy of 346.8 keV[37], as this is the peak with the highest signal-to-noise ratio. Other alternative photopeaks are also considers such as the 844keV peak from ^{27}Al or 1808keV from ^{26}Mg, which may need additional semiprompt $200 < t < 4000$s time cuts to improve the signal-to-noise ratio. The results are used for general detector design optimization of the COMET/Mu2E experiments.

In the low energy region relevant to COMET and Mu2e, there is no data relating to the products of muon nuclear capture, for example the ratio of protons to deuterons and alphas, the absolute proton rate and the energy spectra for aluminium, and titanium. Ti is a promising candidate and is possible to be used for future $\mu - e$ conversion experiments. Active silicon was also used for consistency checks and systematics studies, possibly to be used as an active target for stopped muon optimization. Both $\mu - e$ conversion experiments are presently using proton emission spectrum obtained from the silicon 1968 data but updated with the previous R2013 run.

Several improvements to the experimental setup are as follows:

- Preamplifiers for silicon are now located inside the vacuum chamber and are shielded to further reduce the noise in the readout.
- More lead shielding was added near the germanium detector. The detector itself was also changed to the Canberra model which does not have any occlusion effect.

3.2 Muon beam line

The Swiss muon source provides a continuous beam of 590 MeV protons at a current of 2.2 A [38] equivalent to a beam power of 1.18 MW. It is currently the world's most intense continous beam muon source. Protons are pre-accelerated with a Cockcroft-Walton generator to an energy of 870 keV and then further accelerated to 72 MeV with a 4-sector Injector 2 cyclotron. Finally the protons reach the target energy with a larger 8-sector ring cyclotron. The proton beam hits a thick carbon target that acts as pion production targets. Pions and muons are then directed to the many

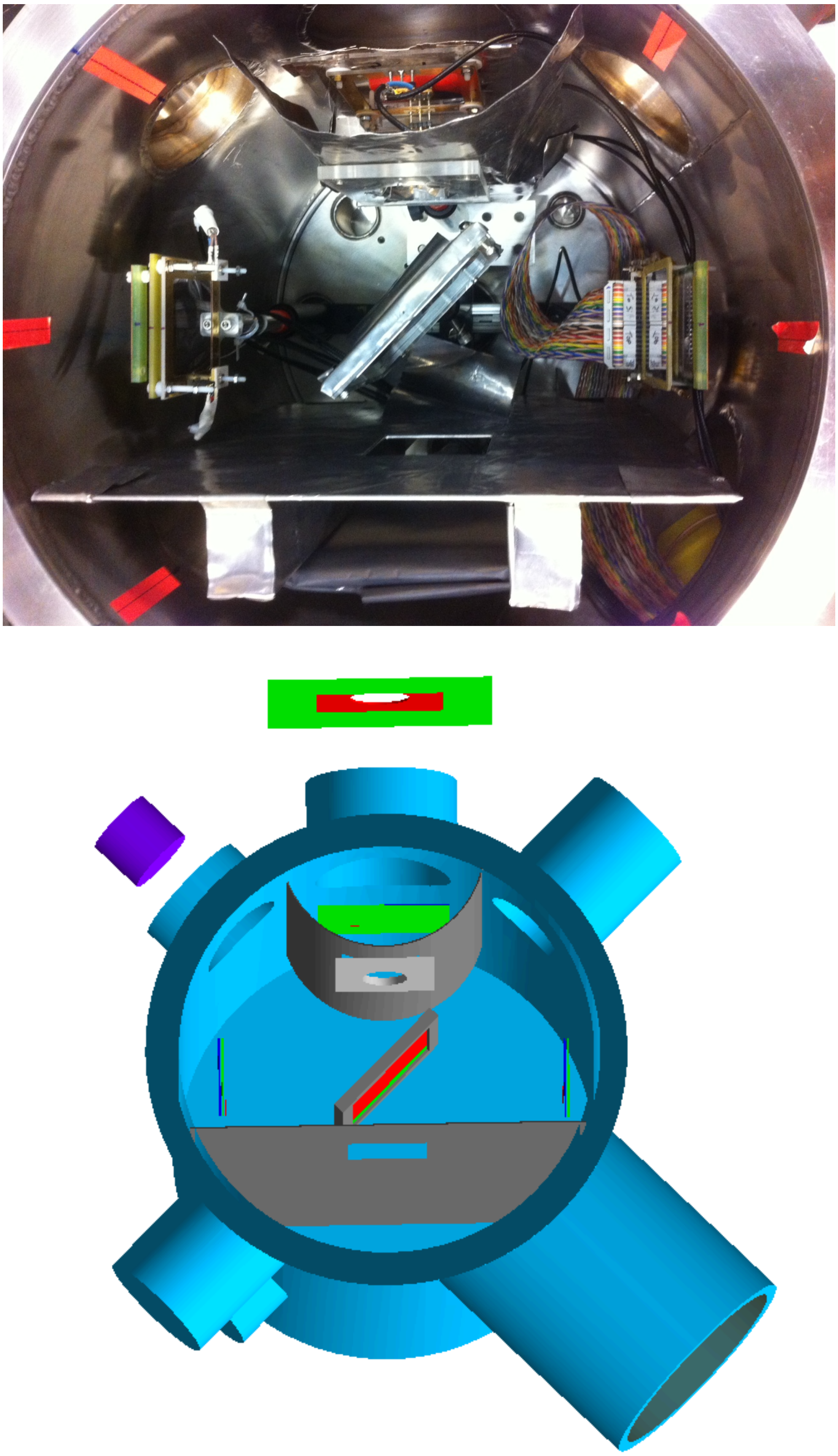

Figure 3.1: Photo and GEANT4 visualization of the vacuum chamber layout for aluminium 100 μm runs.

Target material	Thickness [μm]	Run time [hr]
^{27}Al	50 μm	50
^{27}Al	100 μm	25.7
^{28}Si	50 μm	8.5

Table 3.1: R2015B target and run time used for charged particle emission study.

beam lines are experimental use. The beam line was designed to deliver muons with momenta ranging from 10 to 500 MeV and momentum spread from 0.26 to 8.0%[39]. The AlCap experiment used the πE1 beam line and specifically, runs with aluminium 100 μm target used the 31.9 MeV beam momentum.

3.3 Muon stopping target

Negative muons created from from the beam are stopped in the vacuum chamber, Figure.3.1 by a stopping target after passing through a plastic scintillator and a thin silicon entrance detector placed inside the vacuum chamber. These stopping target are of known material and thickness as noted in Table.3.1.

The stopping target is placed at 45^o tilt to the beam to reduce the amount of material the emitted particle would have to pass through before reaching the left and right counter telescopes. The target holder was wrapped with lead to minimize contacts with the plastic target holder which would result in higher background. Muon x-rays from lead would have minimally contaminate, since the muonic lifetime in lead is only 75 ns as shown in Table.2.1. The silicon target in addition to being used as a muon stopping material can also provide muon beam profile measurements. Titanium data is also obtained as there is not much information relating to charged particle emission in the literature. It may also be used as a muon stopping target material in future muon to electron conversion experiments.

3.4 Data acquisition

The CAEN TDC V1290A was used to record the fast timing information from the detectors which includes the germanium detector. Fast digitiser DT5730 500 MHz for silicon fast pulses, but the threshold for the digitiser was set too high so they could not be used. The Germanium detector is connected to the V1724, two channels were available, one with low gain and another with high gain. For the R2015b the AlCap frontend electronics was upgraded with five 8-channel 12 bit 100 MHz Struck waveform digitizers model SIS3300 and two 4-channel 12 bit 500 MHz Struck waveform digitizers model SIS3350. The electronics layout is shown in Figure.3.2 They are responsible for getting ADC pulse information, with low noise so it is good for energy measurement. Dynamic range was set to 0-5 V with 12 bit ADC (0-4096). A special synchronization pulse was fanned out and sent to a dedicated channel of each digitizer and TDC to control digital jitter and to ensure synchronization between different DAQ components.

The MIDAS data acquisition system[40] was used as the main acquisition software. The Data Acquisition System (DAQ) of the AlCap experiment, so-called AlCapDAQ, provided the readout of front-end electronics, event assembling, data

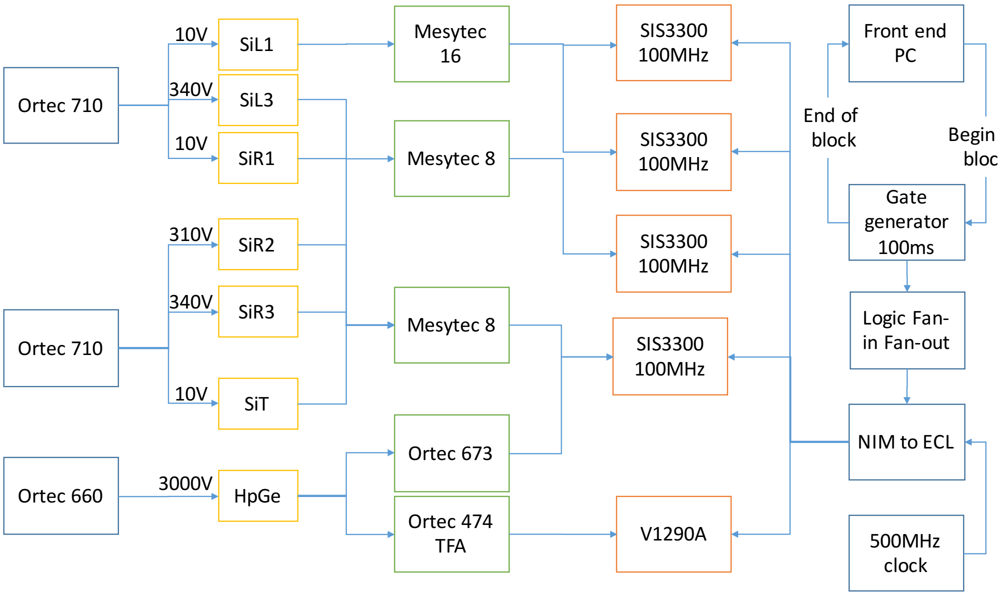

Figure 3.2: The figure shows the electronics schema of the AlCap experiment. The detector elements are in yellow boxes, pre-amplifiers in green, and ADC modules are in orange.

logging, hardware monitoring and control, and the run database of the experiment Data was collected almost continuously in a 98 ms block structure, where each block is stored in a single MIDAS event. All the events from a single run are collected into MIDAS (.mid) files which has a default size limit of 2 GB.

3.5 Germanium detector

The detector's primary purpose is the count and identify x-rays and gamma-rays that were emitted after muon interactions with the target nuclei. Accounting for the detector geometrical and energy efficiencies, it is possible to obtain a good estimate of the number of stopped and nuclear captured muons. Several x-ray peaks from the atomic cascade of aluminium and gamma-ray peaks from nuclear decay after muon capture could be observed and they can be used in concert to provide validation to the muon normalization. The germanium detector has very good timing and energy resolution. Many peaks can be separated properly. Two channels with low and high gain which extended the measureable energy range of the detector are available for cross-validation. Two different gain settings were used. A higher gain at 6000 V DC is used for obtaining good waveform digitizer bit resolution below 3 MeV and a lower gain at 3000 V DC is for getting wider dynamic energy range. The germanium crystal is a closed end coaxial, p-type detector marketed under the name Canberra GC-2018. The crystal diameter is 53 mm, length 44 mm and the distance from the outside window is 5 mm. The distance of this window to the center of the muon stopping target is 237 mm. There is a space of 30 mm between the Al window of the chamber and the germanium detector window.

Energy [keV]	GeLoGain [ADC]	GeHiGain [ADC]
244.7	612.74(0.05)	1321.73(0.08)
344.3	862.00(0.03)	1859.43(0.05)
411.1	1029.12(0.14)	2219.95(0.26)
444.0	1111.63(0.12)	2397.92(0.22)
778.9	1950.73(0.08)	4207.38(0.17)
867.4	2172.55(0.19)	4685.98(0.41)
964.1	2414.69(0.09)	5207.77(0.20)
1085.9	2721.16(0.14)	5868.42(0.30)
1112.1	2785.77(0.12)	6007.69(0.25)
1408.0	3527.48(0.10)	7606.54(0.24)
898.0	2248.86(0.09)	4851.24(0.18)
1836.0	4600.69(0.18)	9921.60(0.42)

Table 3.2: Germanium energy calibration points. Statistical errors are generally less than 0.1% of the measurement ADC values.

	Offset	Gradient
GeLoGain	0.24	0.40
GeHiGain	0.12	0.19

Table 3.3: Germanium energy calibration parameters.

3.5.1 Energy calibration

The energy calibration points used are shown in Table.3.2. The calibration points are fit with a linear function.

$$E = m * \mathrm{ADC} + c \tag{3.1}$$

where m is the gradient and c the offset.

3.5.2 Energy resolution

Energy resolution is defined as the (FWHM) of a signal peak in the energy spectrum. The signal peak can be thought of as gaussian so the FWHM can be written as 2.355σ. The total FWHM is a quadrature sum of the FWHM values from various sources of fluctuation, The resolutions for the germanium detector is shown in Figure.3.4. The detector resolution at 1.33 MeV was tested with ^{60}Co to be 1.8keV and this test was conducted in 17 years prior to the date of the experiment. The resolution has doubled over the years due to its age and radiation damage from being used in other experiments.

$$\mathrm{FWHM}(E) = \sqrt{w_i^2 + w_e^2 + w_p^2 + w_c^2} \tag{3.2}$$

where $w_i << 0.1$eV is the intrinsic width of the gamma peak which is negligible. w_e is the electronic noise contribution. The Equivalent Noise Charge (ENC) is the number of electrons which would need to be collected in order to obtain a signal with the amplitude of the eletronic noise RMS.

$$w_e = 2.355 \cdot \frac{\eta}{e} \mathrm{ENC}^2 \tag{3.3}$$

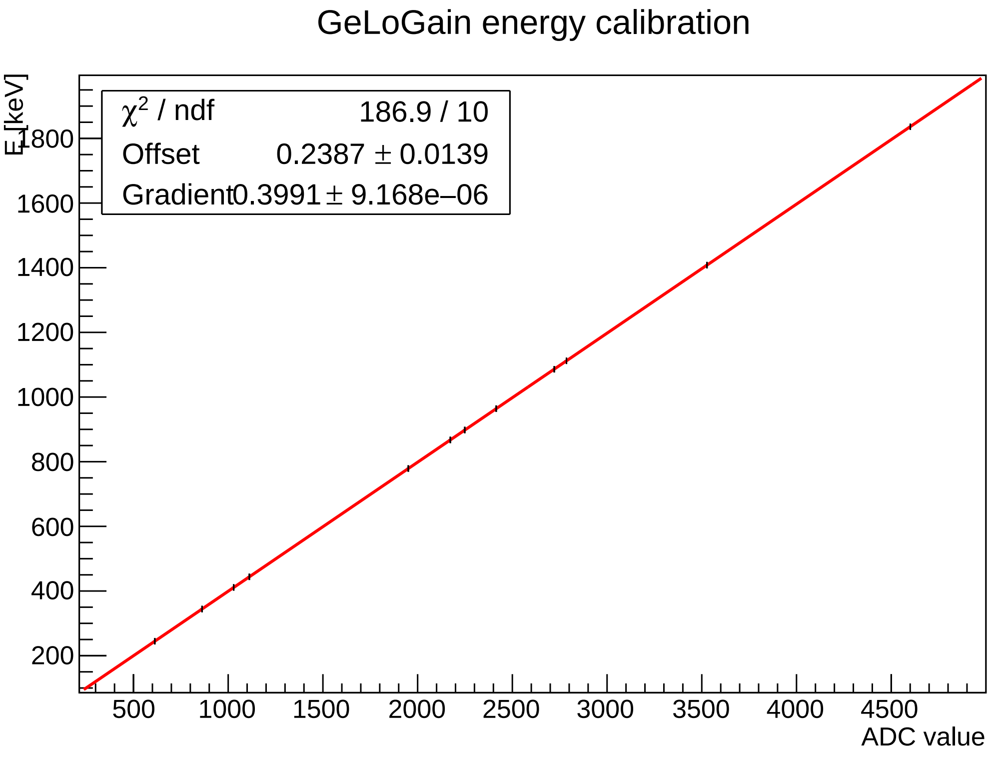

(a) Low gain

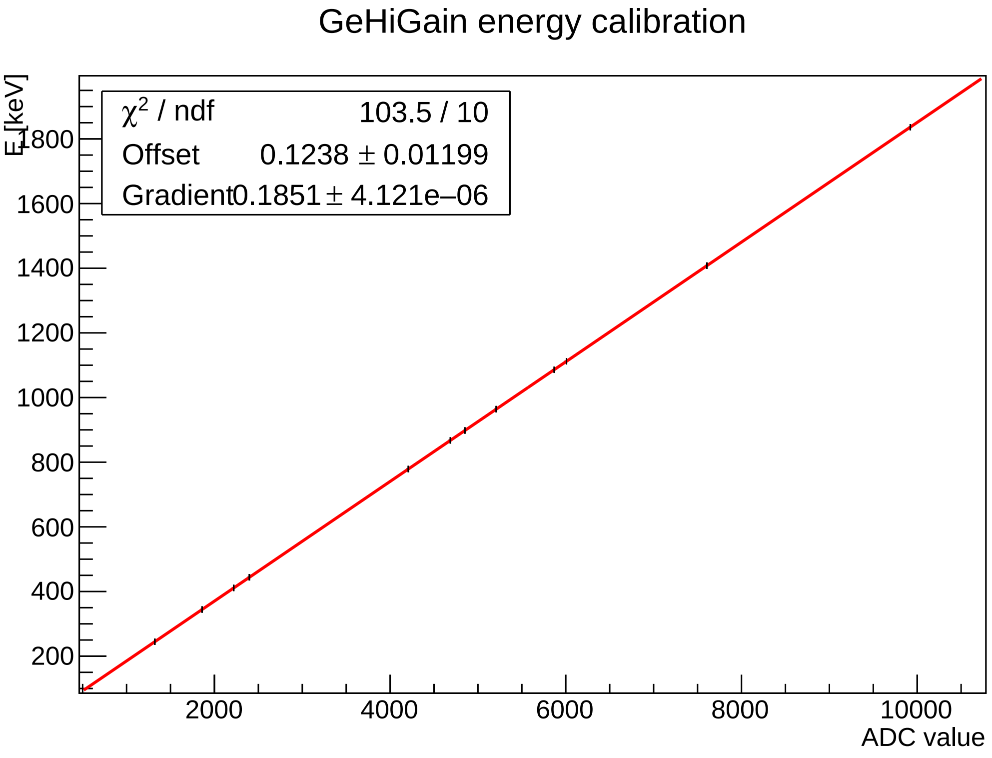

(b) High gain

Figure 3.3: Germanium energy calibration

Series noise, which contributes to the ENC is about 0.1 keV for semi-coaxial germanium detectors. Parallel noise is about 0.6 keV. 1/f noise from 0 to several keV, depending on the situation. In total $w_e \geq 0.65(0.75)$keV for BEG (semi-coaxial) detectors. All quoted numbers depend on filter shape and shaping time.

w_p is the term responsible for charge production in the germanium detector. $\eta = 2.96$eV and is the average energy necessary for the creation of a electron-hole pair in the crystal. Given a deposited energy, E is it expected to produce a total of $N = \frac{E}{\eta}$ electron-hole pairs. The Fano factor for germanium is about 0.11 [41, 42]. $w_p = 2.355 \cdot \sqrt{\eta \mathrm{FE}}$. This is an intrinsic property of the germanium detector and there is no way to reduce this contribution.

Presence of strong crystal imperfections can cause charge trapping, which means not all charge is collected. w_c is difficult to model, but empirically $w_c = 2.355\sqrt{c^2E^2}$.

$$\mathrm{FWHM}(E) = 2.355\sqrt{(\frac{\eta}{e}\mathrm{ENC})^2 + \eta F \cdot E + c^2E^2} \tag{3.4}$$

3.5.3 Efficiency calibration

Germanium energy and efficiency calibration was done using ^{125}Eu and ^{88}Y which had activities of 2.3 kBq and 855 kBq respectively during the time of the experiment. The final two points in Figure.3.5 are from ^{88}Y. It is very convenient to do calibration with ^{125}Eu since it has many energy peaks and calibration with ^{88}Y extending the energy range up till about 2000 keV. This was useful in identifying the 1808 keV peak. Calibration using radioactive samples was done in the following standard way. The activity, A_t of the radioactive material was known beforehand. The detected number of emitted particles, E is recorded for a total measurement time T. The only unknown is then the efficiency η. For ^{152}Eu, the efficiency is calculated for ten peaks and for ^{88}Y, it is done for two peaks.

$$A_t = \frac{E}{\eta T} \tag{3.5}$$

where the activity at experimental time, $A_t = A_0 \times 0.5^{\frac{t}{t_{1/2}}}$. The live measurement time is obtained by counting the number of measurement MIDAS blocks of the run, which is 98ms long. The following efficiency calibration points are used.

The efficiency points are fit to an exponential function,

$$\epsilon = Ae^{-Bx} \tag{3.6}$$

where A is the constant and B the exponential slope.

3.6 Silicon detectors

Several types of silicon detectors are used. A 14-strip detector[1] 52 μm thick is used for the left counter telescope, 4-quadrant detector 50 μm thick is used for the right counter telescope and also the entrance detector. Three 1.5 mm thick detectors are

---

[1] It was originally manufactured as a 16-strip silicon but two strips near the edges are defective.

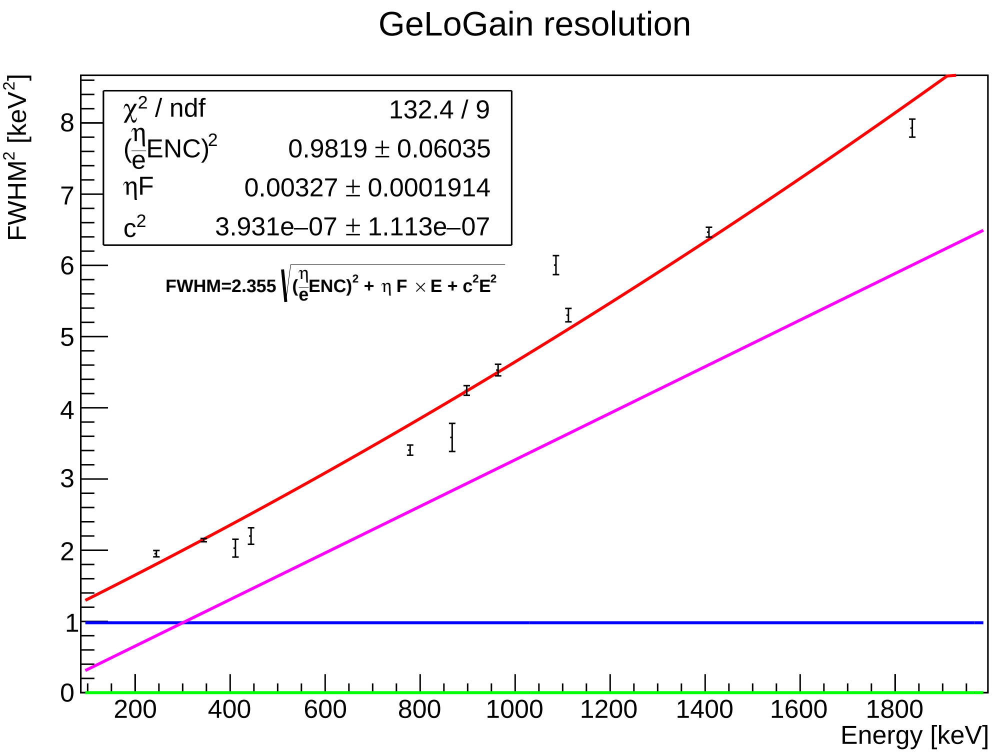

(a) Low gain

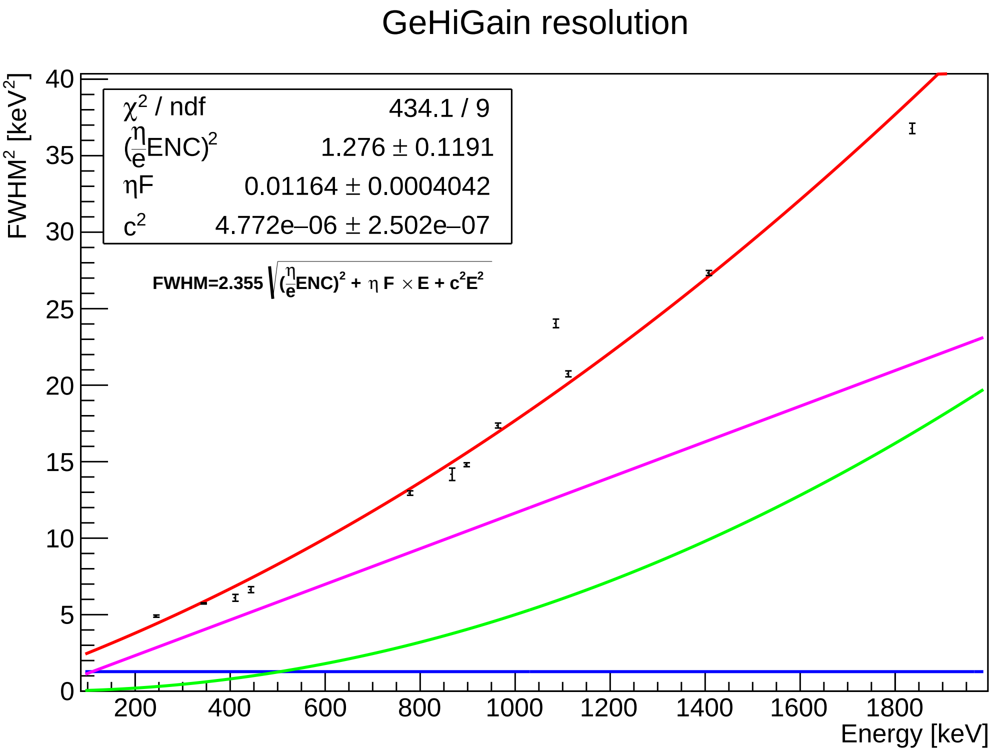

(b) High gain

Figure 3.4: Germanium energy resolution

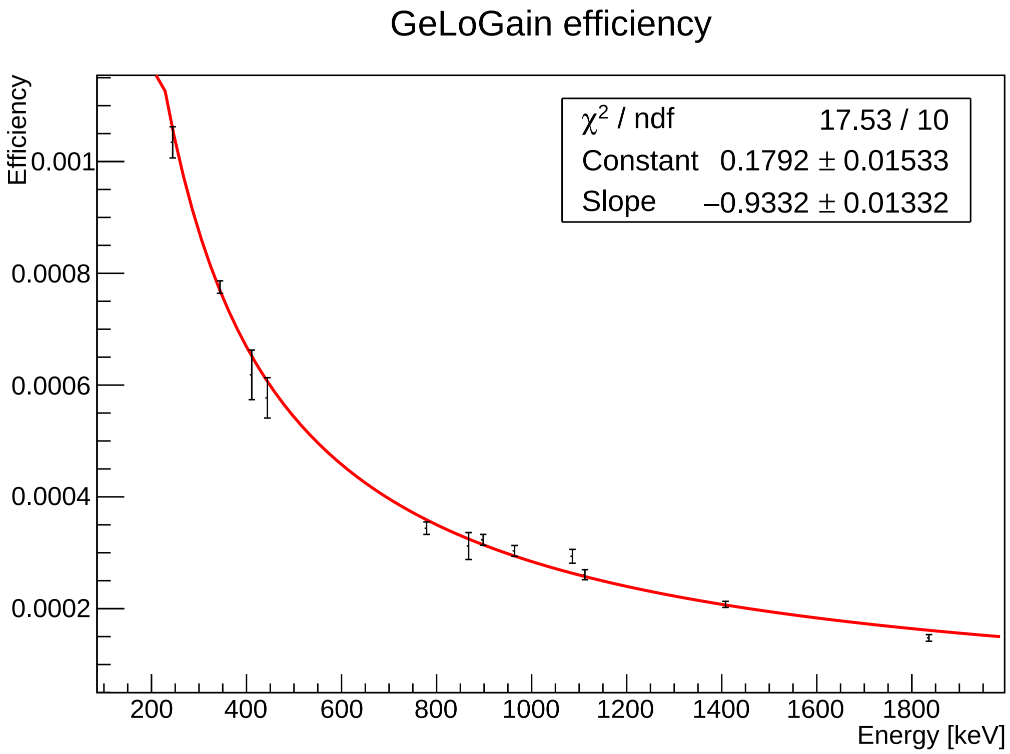

(a) Low gain

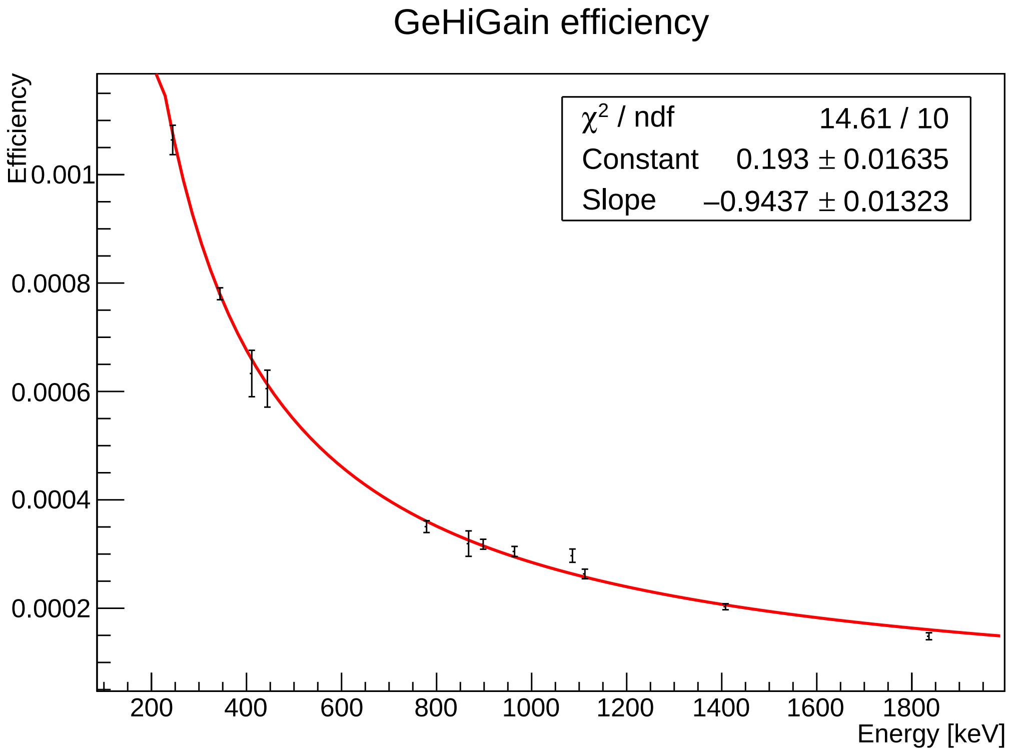

(b) High gain

Figure 3.5: Germanium efficiency calibration

Energy [keV]	GeLoGain ($\times 10^{-4}$)	GeHiGain ($\times 10^{-4}$)
244.7	10.34(0.28)	10.64(0.27)
344.3	7.75(0.11)	7.80(0.11)
411.1	6.18(0.44)	6.33(0.43)
444.0	5.77(0.36)	6.05(0.34)
778.9	3.44(0.11)	3.51(0.11)
867.4	3.12(0.24)	3.19(0.234)
964.1	3.03(0.097)	3.05(0.09)
1085.9	2.94(0.12)	2.97(0.12)
1112.1	2.61(0.90)	2.63(0.09)
1408.0	2.08(0.54)	2.03(0.55)
898.0	3.23(0.97)	3.18(0.92)
1836.0	1.48(0.59)	1.48(0.64)

Table 3.4: Germanium efficiency calibration points from ^{125}Eu. Statistical errors are about the range of 1%.

	Constant	Slope
GeLoGain	0.179(0.015)	-0.933(0.013)
GeHiGain	0.193(0.016)	-0.944(0.013)

Table 3.5: Germanium efficiency calibration parameters

also for the left and right detectors to form the ΔE-E measuring left and right counter telescopes. Using the left 14-strip detector, it is also possible to measure the angular distribution of charged particles emitted from the target.

The detector positions are relative to the incoming beam direction and are noted as left and right counter telescopes. The detectors are manufactured by Micron Semiconductor Works, England. The left detector consists of a 52 μm thin detector and a 1.5 mm thick detector. Both detectors have a dead layer of 0.5 μm thick. Active surface area facing the target is $50\times$ 50 mm. The thin detector is 137.1 mm away from the center of the target. Spacing between the left thin and left thick detector is 10 mm.

The right detector consists of a 58 μm thin detector and two thick detectors, which are 1.545 mm and 1.5 mm thick. The dead layer for all right detectors are also 0.5 μm. The thin detector facing the target is 120.8 mm away. The spacing between the right thin and middle thick is 5 mm and between the middle thick and the last thick detector is 8 mm.

There is a entrance silicon detector which is split into quadrants used for counting muons that enter the experiment. It is 122.6 mm away from the center of the target.

3.6.1 Energy calibration

Silicon energy calibration was done in a variety of ways, using injected pulses with known charge and also using ^{241}Am radioisotope which provides the alpha peak 5486 keV, but with dead layer, the alpha particle emitted with an energy of 5341 keV. The activity of the radioisotope at the time of the experiment was 3.12 kBq. Known charges are injected into the preampflier TEST IN and the output is read out in the DAQ. However, there were problems with saturation and nonlinearity, the test pulse

Detector	Constant	Slope
SiT	-8.01 ± 18.7	2.02 ± 0.02
SiR2	72.02 ± 10.90	4.41 ± 0.04
SiL1	1.09 ± 42.26	2.15 ± 0.47
SiR1	-48.81 ± 18.84	1.81 ± 0.02
SiL3	11.07 ± 18.33	4.47 ± 0.04

Table 3.6: Various silicon detector's energy calibration numbers. Pulses measured by the SiL1 detector above 2MeV showed signs of nonlinearity and saturation.

amplitudes cannot be higher than 2 MeV equivalent. A controlled charge injection circuit with known capacitance and attenuation is used to inject known charges into the Mesytec-16 preamplifier. Square pulses of peak-to-peak height 50 mV, 100 mV and 150 mV is provided as input to the circuit producing charges of 47 fC, 94 fC and 141 fC corresponding to 1.056 MeV, 2.112 MeV and 3.224 MeV equivalent energy deposit in a silicon detector. The preamplifier readout is then converted into 12-bit ADC and read into the DAQ system.

Chapter 4

Event Selection

4.1 Online event selection

This experiment uses self triggering so most of the data collected is stored. No veto systems were used. There were dead time due to electronics where there is 10ms time intervals between two measurement blocks used to extract data from the frontend boards. This maximizes the data readout efficiency since during the 110ms measurement block, the data is recorded into on-board memories. This method was inherited from the MuLan, MuCap and MuSun experiments in PSI[43]. The silicon and germanium detectors had ADC threshold set to reduce data from noise and electrons so the DAQ will only record interesting data from muons. Main event selection is done offline.

4.2 Offline event selection

Since the AlCapDAQ is a trigger-less system, it stored all waveforms of the hits occured in 98 ms long blocks without considering their physics significance. The analysis code therefore must be able to extract parameters of the waveforms, then organises the pulses into the physics events correlated to stopped muons.. In addition, the analyser is intended to be usable as a real-time component of a MIDAS DAQ, where simple analysis could be done online for monitoring and diagnostic during the run.

The analysis framework of AlCap consists of two separate programs. A MIDAS based analyser framework, called alcapana, processes the raw data and passes its ROOT data output to the second stage, called rootana, where most of the physics analysis is performed. Both of the programs were designed to be modularised, which allowed us to develop lightweight analysis modules that were used online to generate plots quickly, while more sophisticated modules can be applied in online analysis.

The DAQ system generated MIDAS files which stores the data as a stream of MIDAS banks. In the AlCap DAQ, each bank corresponds to a single channel on a digitizer and was named according to a predefined convention. The mapping between detector channels and MIDAS bank names was stored in the MIDAS Online Database(ODB), along with other settings such as sampling frequencies, timing offsets, thresholds and calibration coefficients of each channel.

The first step of the analysis framework is to convert the raw MIDAS data into waveforms, series of digitised samples continuous in time corresponding to pulses from the detector. The waveform is called TPulseIslands(TPI), which contain the bank name, the ADC values of the samples and the time stamp of the first sample. This conversion is performed in alcapana and the resulting objects are stored in a ROOT output file as a TTree.

The next step of the analysis is to obtain summary parameters of the pulses from the digitized samples. The parameters of primary interest are the amplitude and time of the peak and the integral of the pulse. This extraction of parameters is done by a rootana module, and the objects produced by this stage are called TAnalysedPulses(TAP). Currently, we have a usable and simple algorithm that takes the pulse parameters from the peak of the waveform. In parallel, a pulse finding and template fitting code is being developed because it would provide more accurate pulse information. The first iteration of this code has been completed and is being tested.

4.2.1 High level analysis packages

From the digitized waveform we can extract the amplitude and time information. It is at this stage that we also perform the energy calibration and add any time shifts that we've measured. Currently, we define the amplitude as the maximum sample of the waveform minus the pedestal. The pedestal is determined from taking the average of the first 5 samples of waveforms in each channel for each run. The time of the pulses is determined using the constant fraction method with a fraction of 20%. In addition, there is currently a time cut of $t < 10 \times 10^3$ns and $t > 96 \times 10^3$ns. This is done to remove the sync pulses. There are currently plans to develop a template fitting algorithm so that identification of pile-up and removal of synchronization pulses without removing genuine pulses that occur at the same time could be done.

4.2.2 Muon centered tree data structure

After obtaining all the TAPs, valid pulses from the SiT channels are defined as a central muon, the time for subsequent events in other detectors will refer to this muon as $t = 0$s. We then look in all the other detectors (including all the SiT channels) and collect all pulses that are within $\pm 15\mu$s of the central muon.

Finally, we create a TTree from the pulses' information in the TMuonEvent (amplitude, energy, time, etc.) including whether a given pulse has been put into one or more TMuonEvents and perform the final analysis on that.

4.3 Run time and beam momentum

The muon beam momentum for the Al100 dataset ranged from 25.7 MeV to 30.9 MeV with variation in between.

Total run time is 25.7 hours (92531.1s, see Figure.4.3), which is calculated based on the total number of MIDAS blocks which is 944195 and the time length of each block being 98 ms.

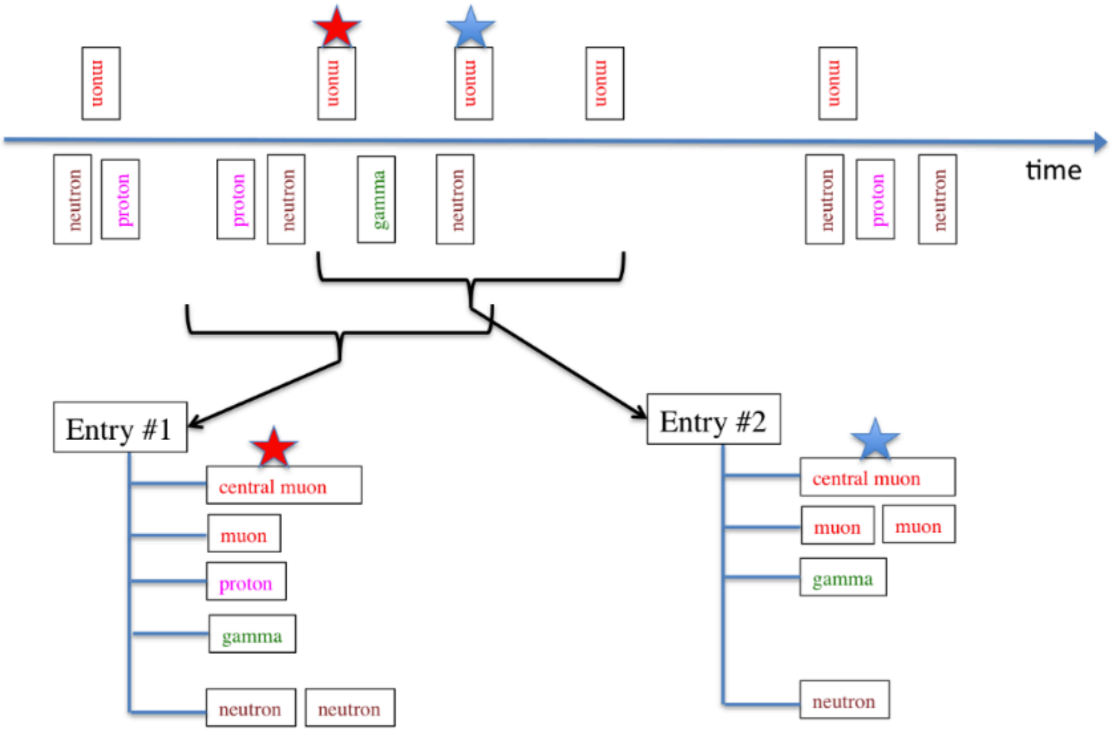

Figure 4.1: The muon centered data format.

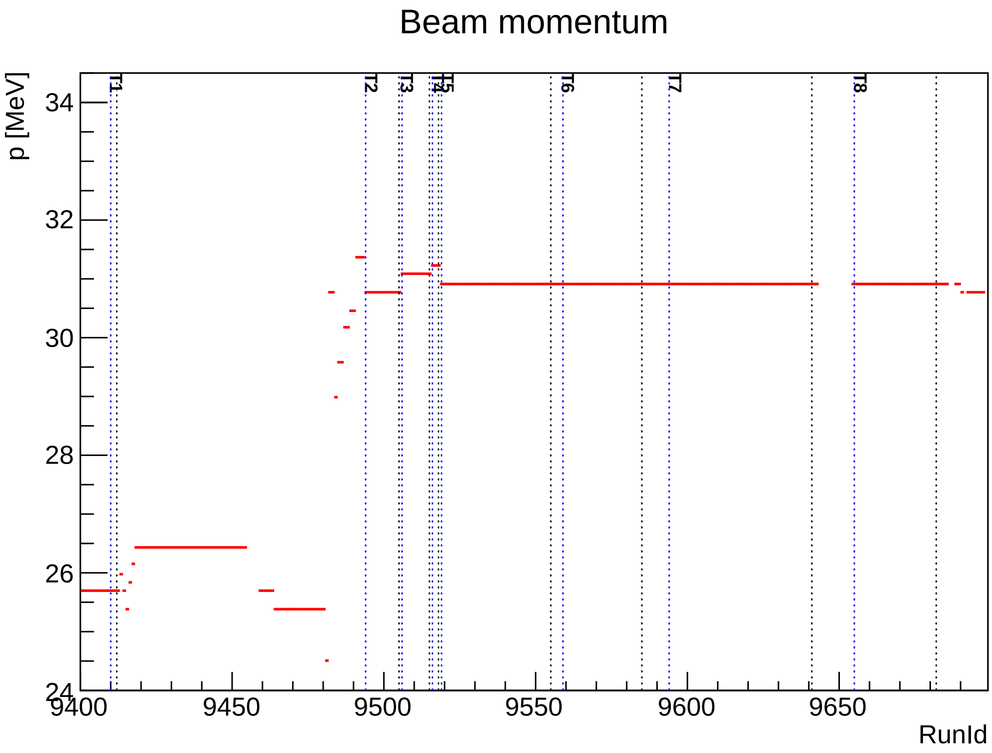

Figure 4.2: Beam momentum during the runs

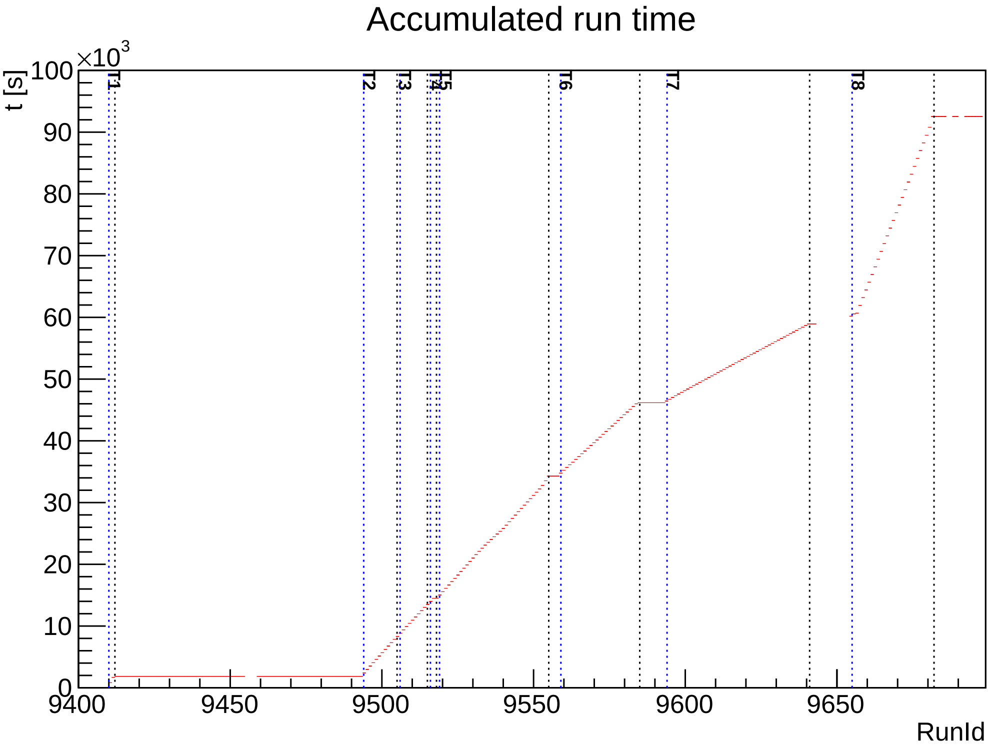

Figure 4.3: Accumulated run time for aluminium 100 μm target. The production quality data was taken in tranches marked T1 to T8 where beam scans and calibrations were done in between the tranches.

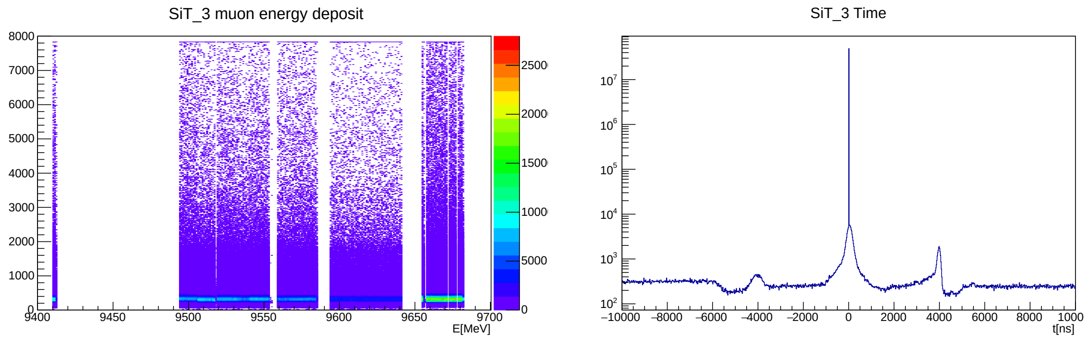

(a) Energy trend

(b) Time structure

Figure 4.4: Data from the muon beam in all aluminium 100 μm runs. This also includes electrons from the beam and other contaminants. The strongest band near 400 keV is from punch through muons.

4.4 Data quality

Much time has been spent in making sure the data that being used is has correct and consistent calibration factors applied and that they contain analyzable data. These data shown are pedestal subtracted and are aligned to the central muon time. The main peak centered at zero is from the main event. The time structures in the plots show two smaller peaks on each side, where the troughs are due to a 4 μs dead time and a second peak in the muon time window and the peaks due to the constant fraction algorithm being fooled into picking a time which is earlier than it actually is. This can happen when two pulses overlap, making it wider than it actually is.

In Figure.4.4, the plot shows consistently that the energy of the muon entering the vacuum chamber depositing the same amount of energy of about 400 keV. The entrance detector is a silicon quadrant detector so plots for other quadrants look similar except for the number of muons detected which is asymmetric since the muon beam is not directed on the center of the detector. The start time of the muon centered tree is based on the time a muon passes through this detector.

A sample of a channel from the thin left counter telescope is shown in Figure.4.5. It is part of a 14-strip silicon, and together with the thick left silicon detector, with the trend data in Figure.4.6, form the left counter for identifying charged particles. They are both shown to be working well. It is possible to also obtain the muon decay time from the time structure of the thick detector. However, before particle selection, it include decay times for all charged particles from aluminium, background material such as lead and steel and scattered muons. Similarly for right counter telescopes, which are shown in Figures.4.8.

The germanium detector has two separate channels for high resolution readout and wider energy range. Both channels detect strong signals from the 346 keV which is from the 2p-1s muonic aluminium transition and 511 keV from pair-produced positron annihilation. Similarly the muonic lifetime can also be measured using germanium detector time data.

Figure.4.11 shows the summary of the number of pulses measured for each channel for all runs in aluminium 100 μm.

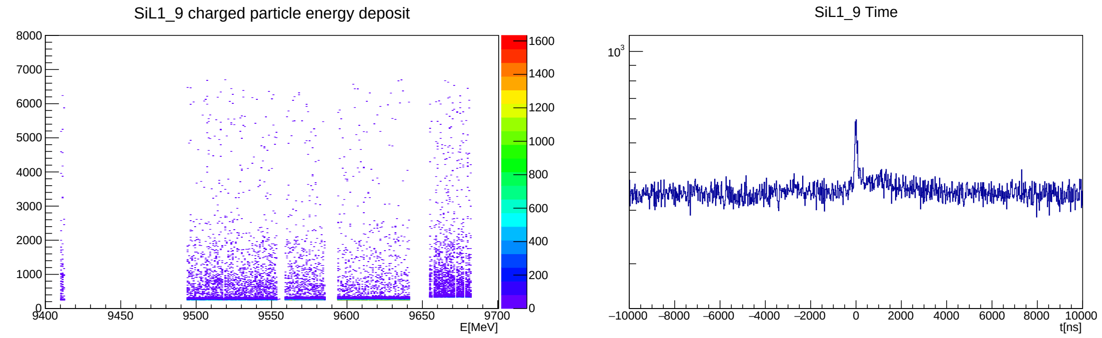

(a) Energy trend (b) Time structure

Figure 4.5: Data from one of the stripped silicon in the thin silicon of the left telescope counter.

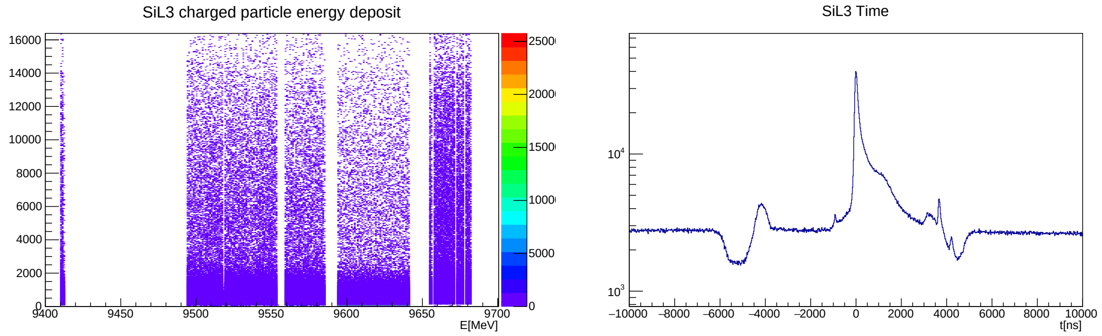

(a) Energy trend (b) Time structure

Figure 4.6: Left counter telescope thick silicon energy deposit and time structure of the data for each run.

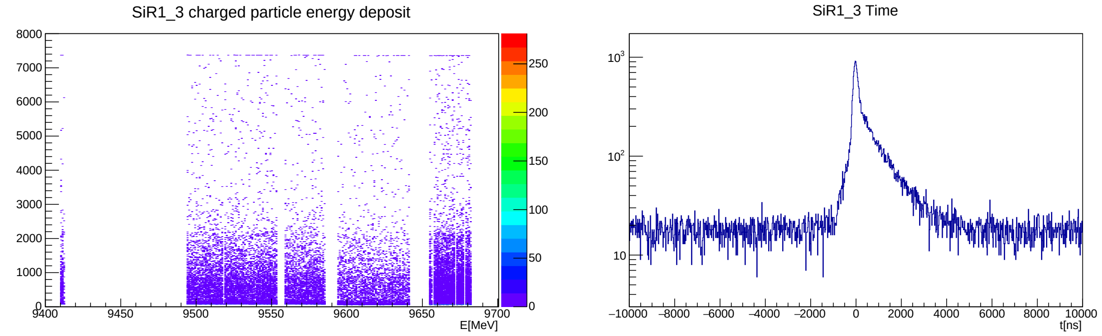

(a) Energy trend (b) Time structure

Figure 4.7: Data from one of the quadrant from the thin silicon in the right telescope counter.

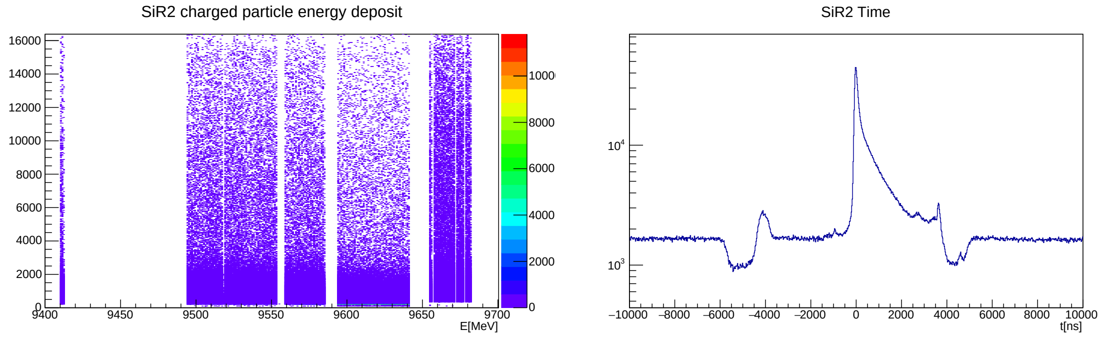

(a) Energy trend

(b) Time structure

Figure 4.8: Energy and time structure recorded in the thick silicon in the right counter telescope for every aluminium 100 μm run.

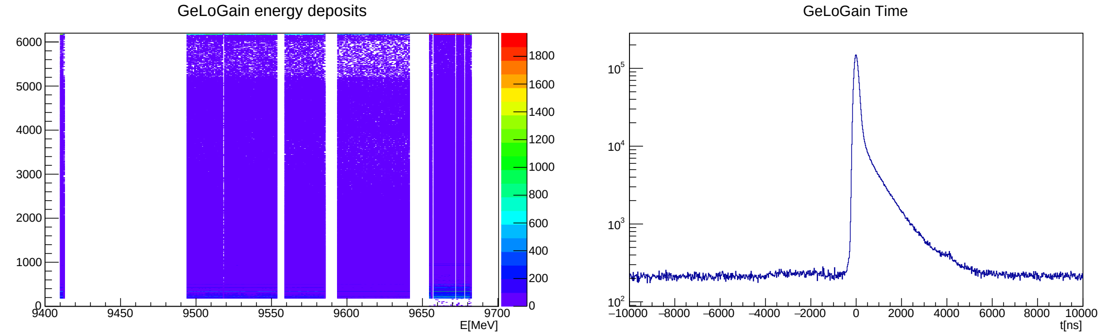

(a) Energy trend

(b) Time structure

Figure 4.9: Germanium low gain channel data for each run.

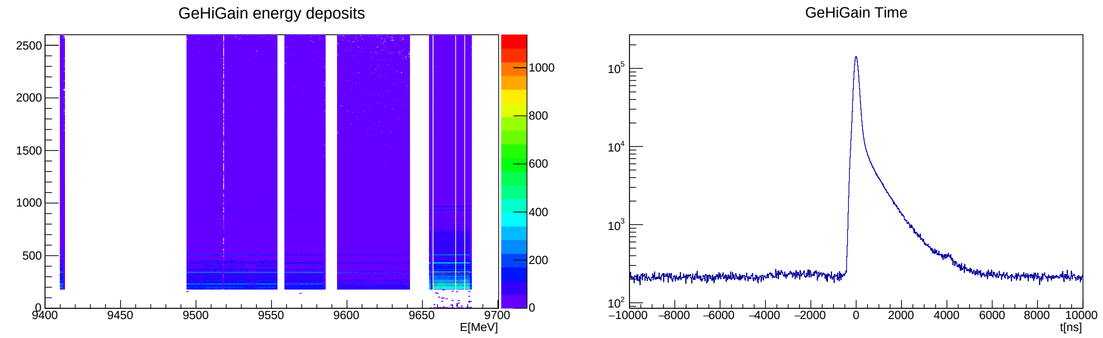

(a) Energy trend

(b) Time structure

Figure 4.10: Germanium high gain channel data for each run.

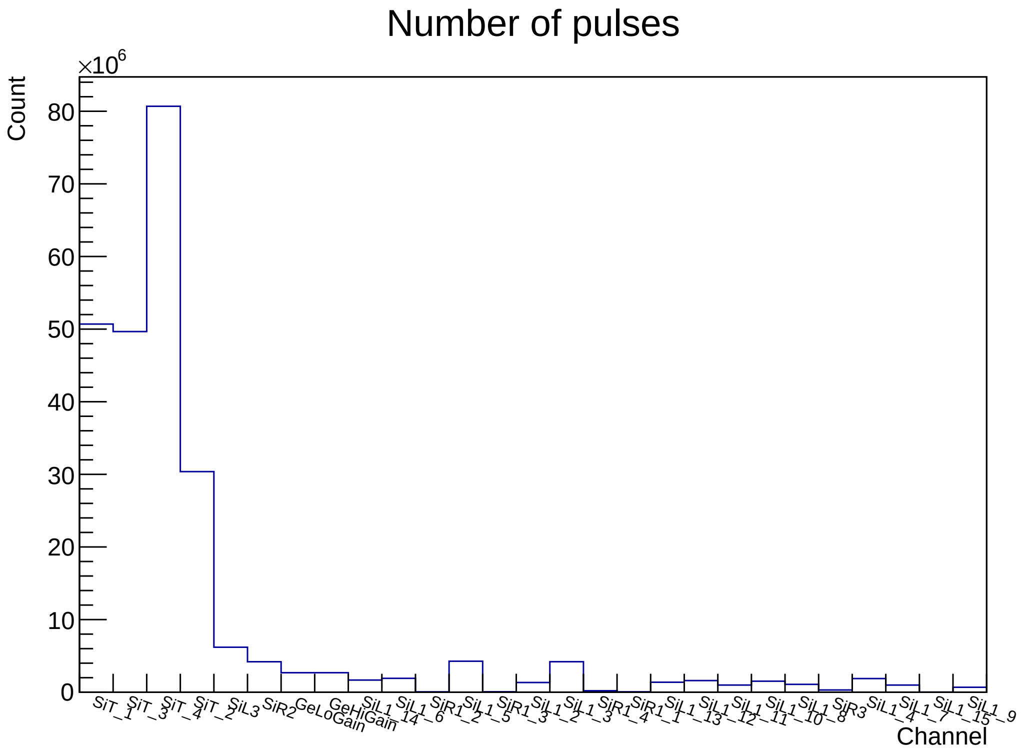

Figure 4.11: Number of pulses per channel for all runs.

4.4.1 Pulse structure

The pulse time is taken to be the detector measurement dead time, since if a signal is being processed by the electronics, it effectively blocks the measurement of the next signal if it happens to arrive during the measurement of the previous signal. The pulses have very short time as can be seen from Figures4.12. This is in comparison to the muon centered time window.

4.5 Photon events

Data was collected by using a high purity germanium detector to measure all x-ray and gamma radiation. The next few sections show the full spectrum measured by the germanium detector split into various energy ranges. They are categorized according to different times as shown in Figure.4.13. Figure.4.14 show the good agreement between the low and high gain channels which shows that calibration was done correctly.

- Prompt, $-200 < t < 200$ns, for identifying muonic x-rays.
- Semiprompt, $200 \leq t < 4000$ns, for identifying gammas that came from nuclear muon capture.
- Delayed, $t \geq 4000$ns, for identifying long-lived sources, possibly from activation and/or ambient radiation.

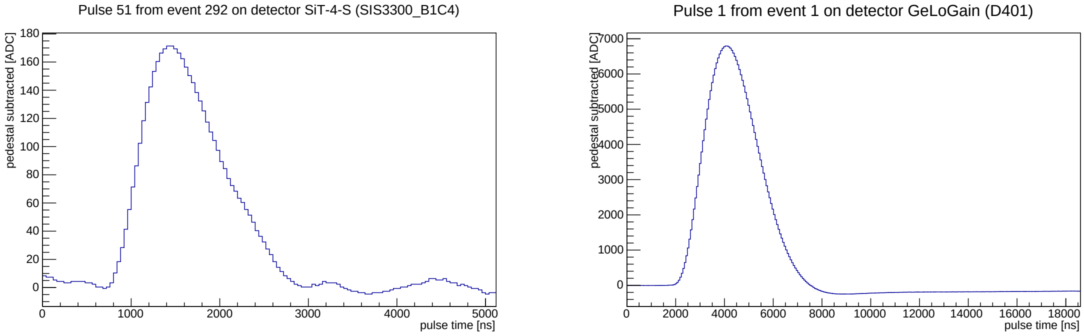

(a) Entrance detector, $t_{avg} \approx 2000$ns.

(b) Low gain germanium detector, $t_{avg} \approx 6000$ns.

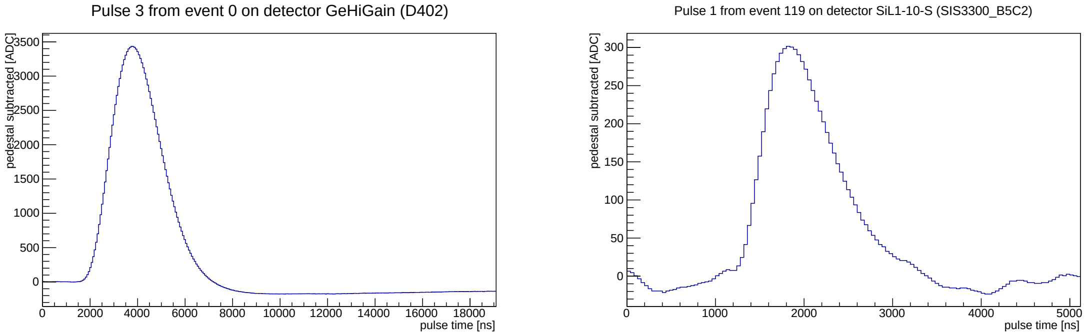

(c) High gain germanium detector, $t_{avg} \approx 6000$ns, pulse height is half that of GeLoGain pulses.

(d) Left counter, typically containing more noise but pulse is still easily resolvable, $t_{avg} \approx 3000$ns.

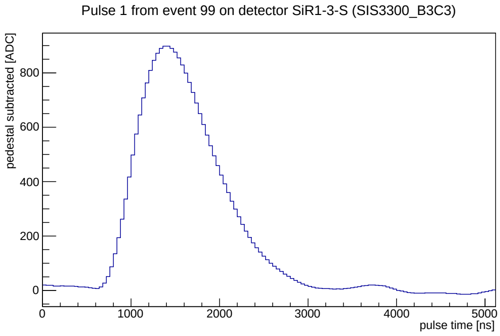

(e) Right counter. less noise and sharing the same pulse time of 2000 ns.

Figure 4.12: Sample pulses from all representative channels in all silicon and germanium detectors.

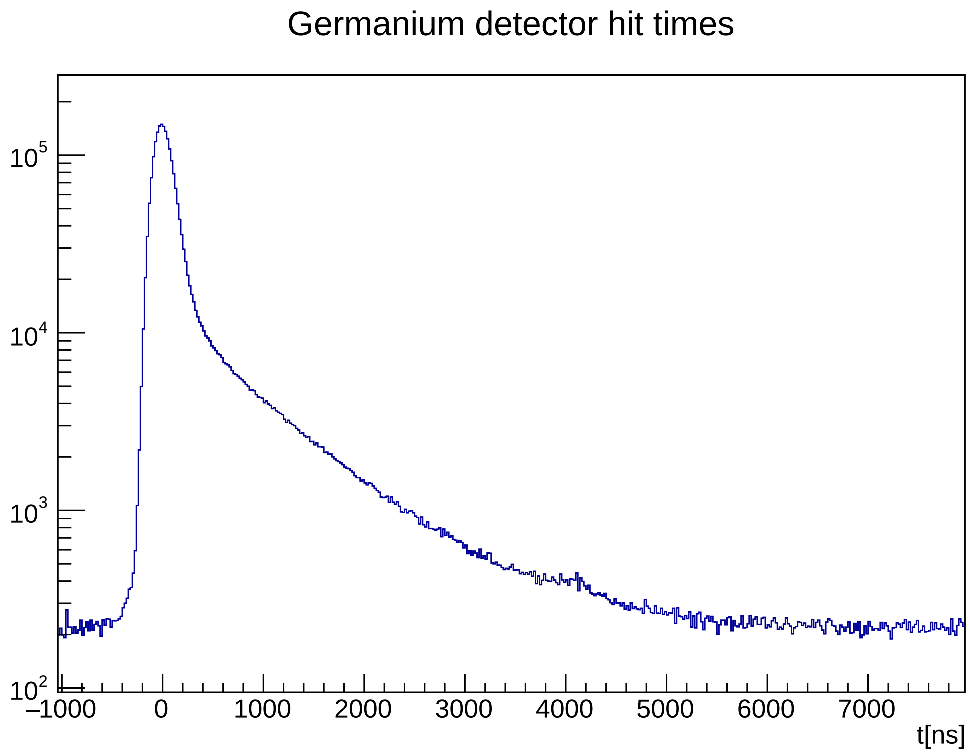

Figure 4.13: Germanium detector timing profile.

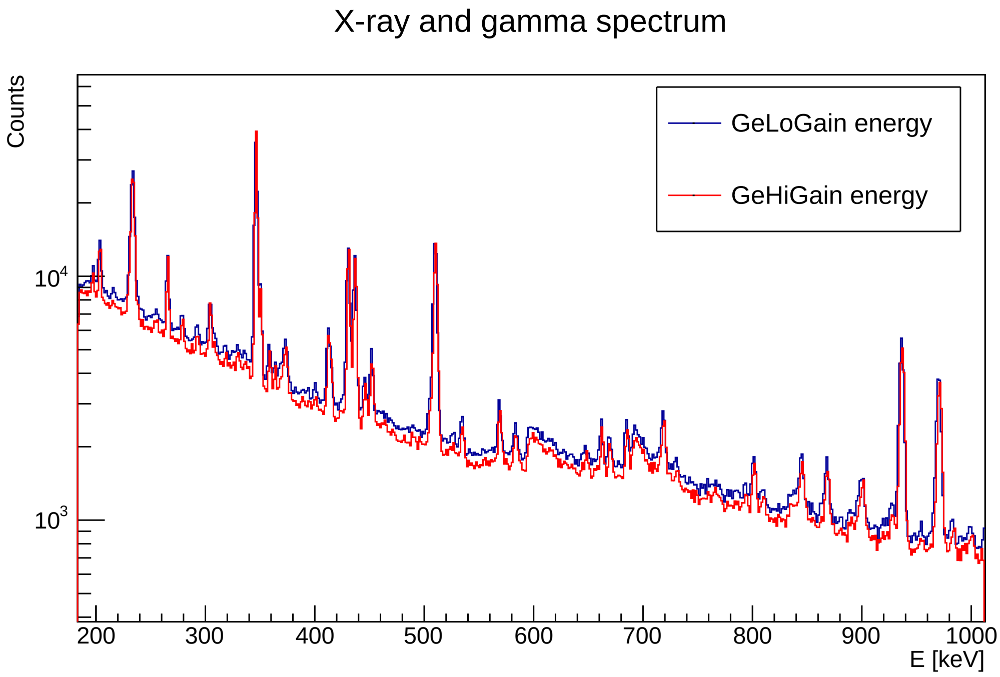

Figure 4.14: Overlap between the low gain and high gain channels for energides less than 1 MeV.

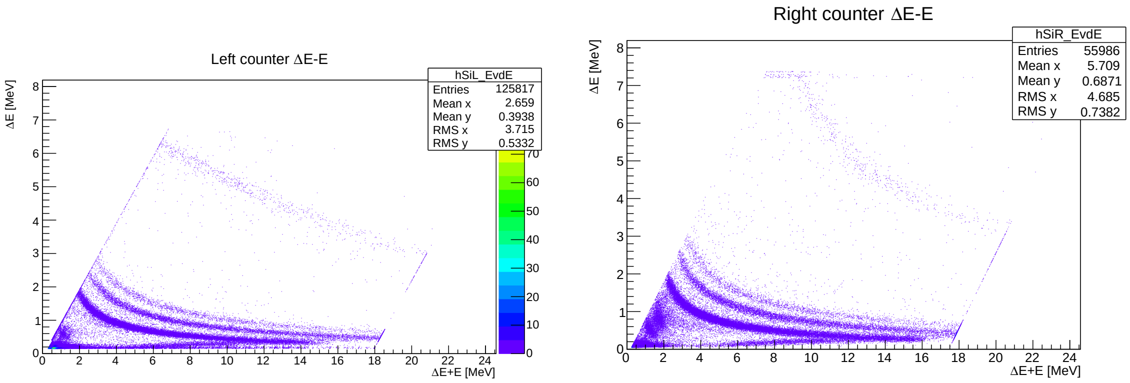

(a) Left counter

(b) Right counter

Figure 4.15: Raw ΔE-E plots from the counter telescopes

4.6 Charged particle events

Counter telescopes are used to identify particles based on their energy deposit signatures. Due to nonlinearity and saturation of the left thin silicon, the alpha energies are not properly measured and thus cannot be used. The left counter is also much more noisier so the raw plots shows more counts than the right counter. Both plots show clear proton, deuteron and triton particle band separation.

4.6.1 Background cuts

The pulse times in the silicon detectors are all aligned to the muon entrance time. To remove some of the noise, a time cut is apply to select signals that appear to be created from charged particles. It is possible to apply this cut because time between pulses in the thin and thick detector would be very close together. The time difference between two pulses in thin and thick silicon is chosen to be within a $2\,\mu$s. It is desirable to select signals by choosing a suitable time range where most of the background can be reduced. There are many sources of backgrounds that are recorded by the silicon detectors. Muons that scatter directly to the detectors themselves, either depositing energy and/or creating other charged particles like electrons. Muons also can be captured by surrounding lead and iron and emit background x-rays. These muons also may create charged particles that can be recorded by the silicon detectors, but the excited lead or iron nuclei have a much shorter lifetime of about 75ns.

In Figure.4.16, the combined time between the all thin channels and the corresponding thick silicon is shown. The left counter has a rather significant bump near -1000 ns as it is noisier and also the thin silicon itself is divided in 14 strips. In comparison to the right counter which has a much better profile since it has only four separate channels. Therefore a $2\,\mu$s cut would include the signals that are further away from the peak value at zero.

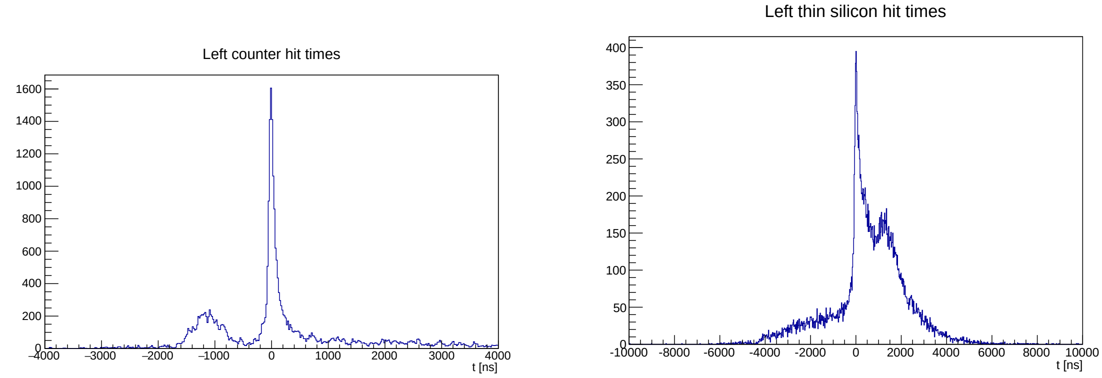

(a) Left counter hit times

(b) Left thin silicon time

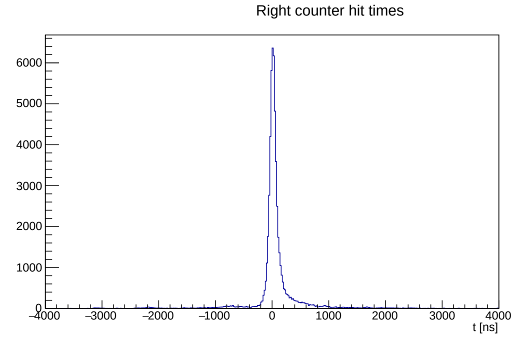

(c) Right counter hit times

Figure 4.16: The entrance detector provides the start time for the time measurement of a hit in each detector. The times shown in the plots are time since the initial muon hit.

Chapter 5

Analysis

5.1 Muon beam

Muons arrive at the vacuum chamber from the πE1 beam line continuously. Some pions might also reach together with electrons from beam muon decays. These particles will pass through the silicon entrance detector. Electrons after muon decay in the beam transfer away a wide spectrum of energy, shared with the electron neutrino. There is a distinct electron peak in the low energy region of Figure.5.1 which was partially cut away by setting a higher ADC threshold since we are primarily interested in muons only. The small bump at about 900 keV is due to muon pile-ups with a maximum value of double pulse height. The next small peak at about 1700 keV is due the stopped muon peak. On the rare occasion, the muon loses all its kinetic energy and it gets stopped in the silicon atom Coulomb potential. From Figure.5.1, this happens at a rate of less than 0.1% per detected muon that passes through the entrance detector. The continuous spectrum after this is thought to be the contribution from charged particles after muon capture in silicon. The protons that are produced are less than 1% of the muons which is consistent with the stopping rate in silicon. Near 5 MeV, there is a statistical fluctuation due to histogram binning issues. Therefore a good muon selection cut would be to remove the remaining electron partial peak up till the beginning of the muon stopping peak. Figure.5.2 shows the energy loss of muons in silicon according to Bethe. The plot is drawn based on the thickness of the entrance detector is 58 μm. An approximate calculation of determining the energy deposit is done by taking the average integral of

$$\int dx \frac{dE}{dx} = \rho \frac{dE}{dx} dx \tag{5.1}$$

Free muons have a lifetime of 2.2 μs and while traveling from the pion production target, statistically some of them would have decayed into electrons. Pions have a lifetime of 29 ns and would have all decayed away so the amount of pions in the beam would be negligible at about 4×10^{-4}.

5.2 Beam profile

The beam profile was measured in dedicated runs using the 16 strip silicon detector as shown in Figure.5.3. After fitting, the vertical beam profile has $\mu = 8.80 \pm 0.02$ and $\sigma = 7.37 \pm 0.05$. The horizontal beam profile has $\mu = 9.96 \pm 0.02$ and $\sigma = 4.86 \pm 0.05$.

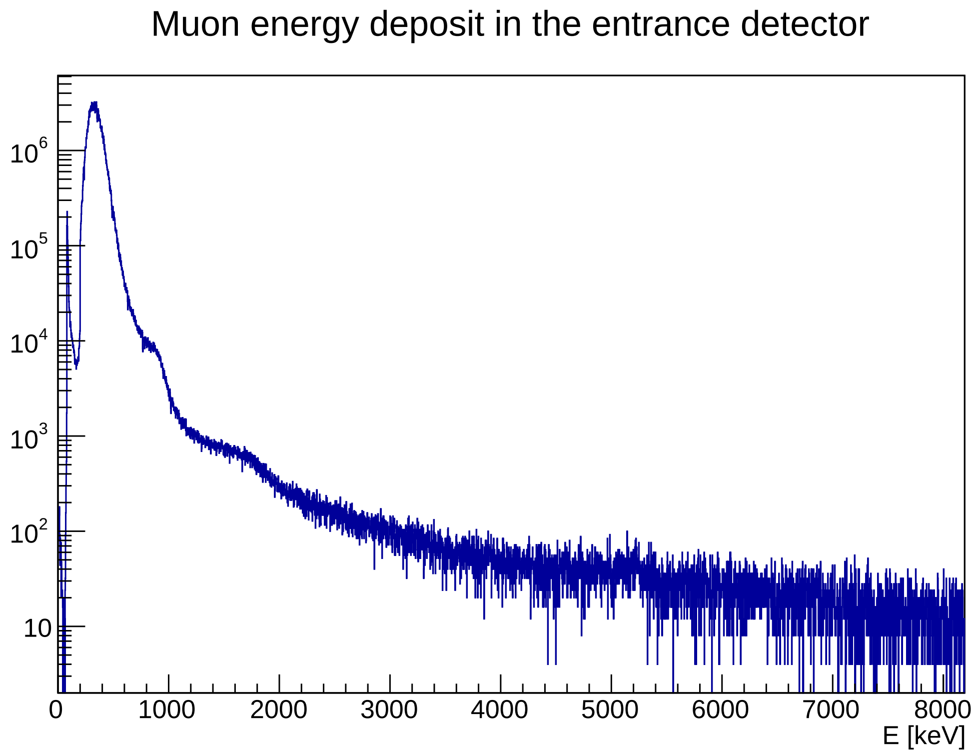

Figure 5.1: Based on the main energy deposition peak with peak value of 331 keV, it is estimated that the incoming muon energy is about 1700keV calculated from the Bethe formula for μ^- in Silicon. Total muons detected is 2.10×10^8 with an uncertainty of less than 1%.

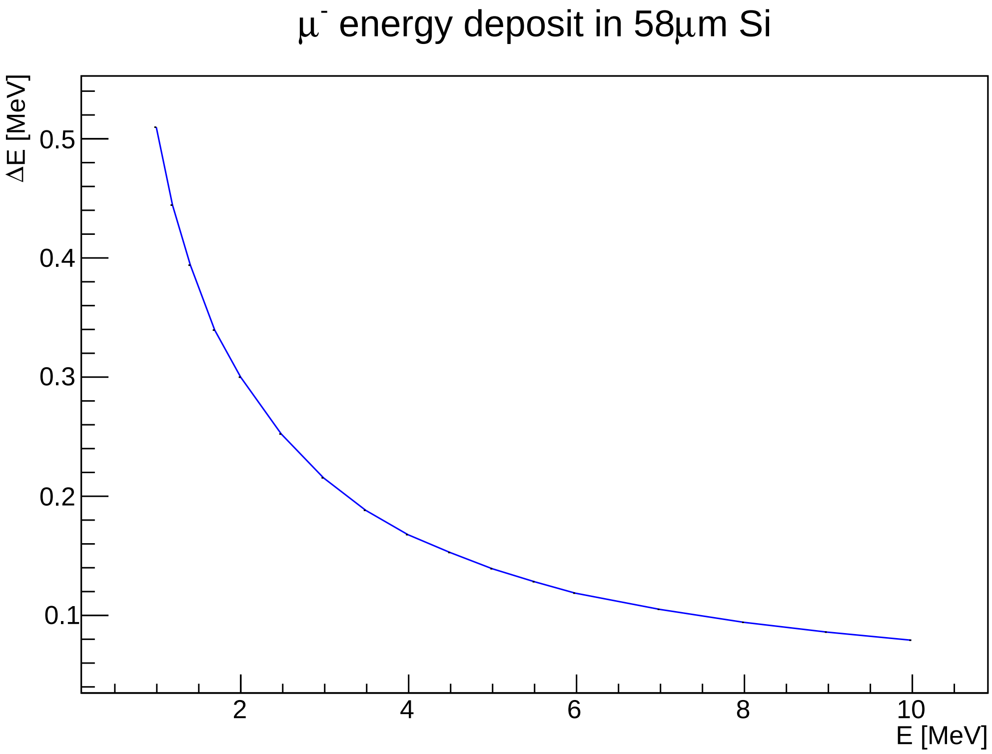

Figure 5.2: Bethe dE/dx plot for low energy μ^- in silicon.

These values would be used in simulating the beam profile for generating a response matrix so it needs to be converted to the respective coordinate system.

- x-direction: μ =6.31 mm and σ =15.66 mm
- y-direction: μ =2.40 mm and σ =23.36 mm

The center of the stopping target is defined to be $(0, 0)$ in the simulation. Muons would travel along the z-direction into the vacuum chamber. x-direction would be connecting the left and right counter telescopes and the y-direction up and down.

5.3 Stopped muon normalization

The goal of the AlCap experiment is to get the proton emission rate per stopped muon, hence it is required to know the number of muons that stopped in the aluminium target.

5.3.1 200keV to 500keV

A germanium detector with an active region of 9 cm^2 surface area is used for detecting and measuring with high accuracy of up to 1 keV resolution the various x-rays and gamma-rays emitted when muons interact with material in the experimental chamber. The germanium detector has a dynamic energy range of up to 3000 keV and 6000 keV for the low gain and high gain channels respectively. The energy spectrum starts from about 200 keV after the discriminator cut. In Figure.5.4, the

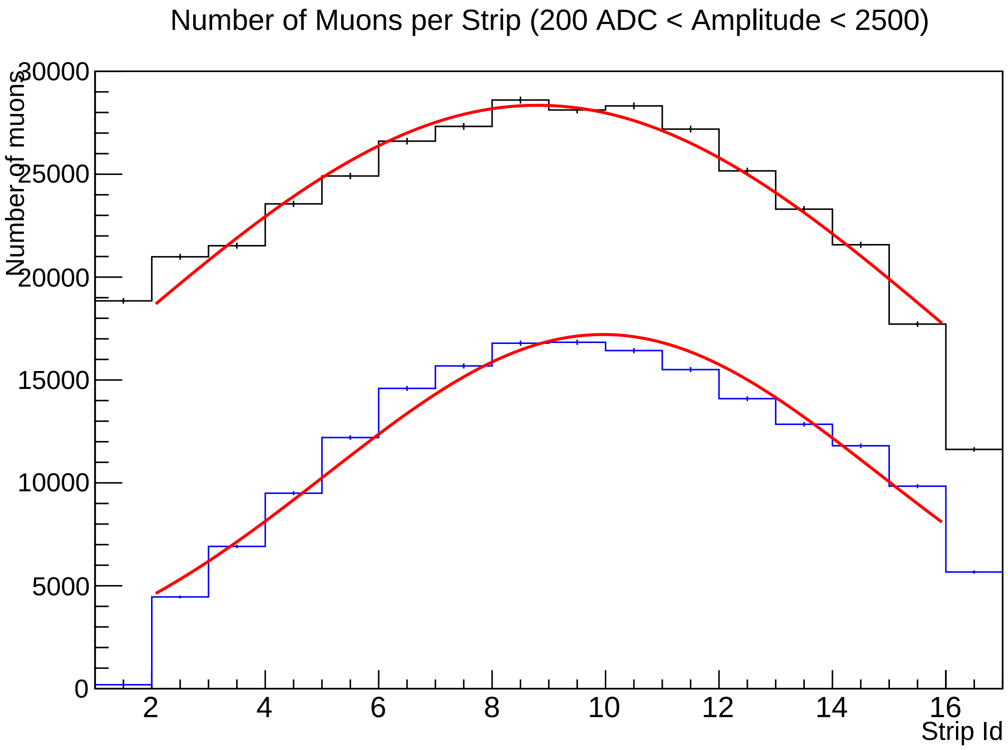

Figure 5.3: Muon beam profile as measured using a 14-stripped silicon placed in the stopping target holder. The blue histogram is the profile from horizontally placed stripped silicon and the black histogram from vertically placed stripped silicon.

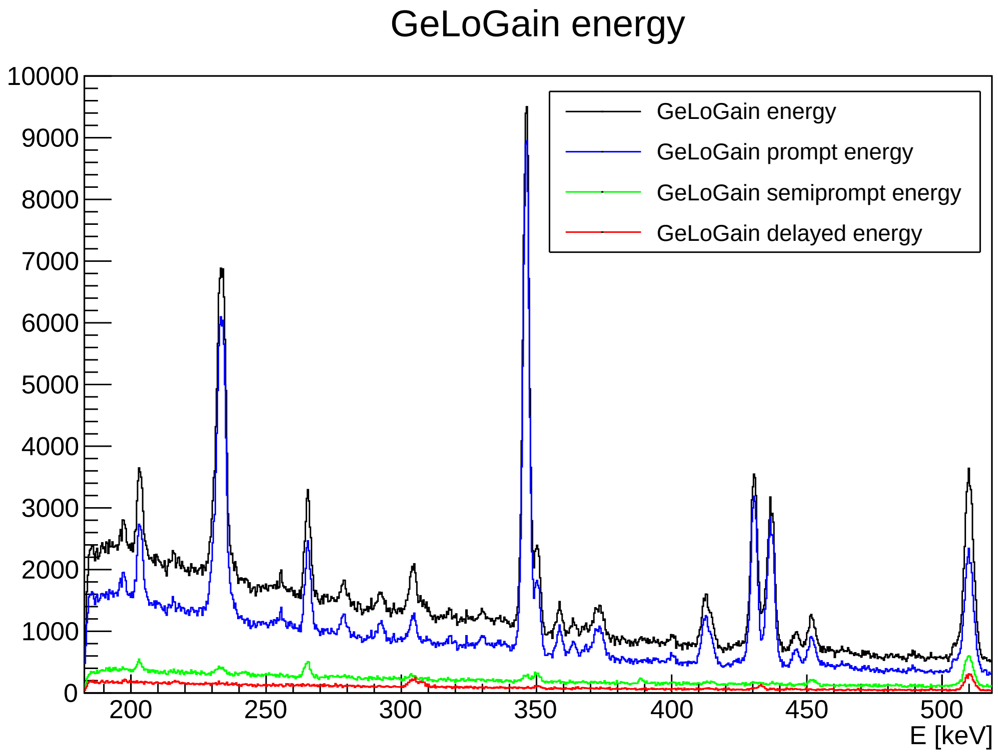

Figure 5.4: Energy spectrum as seen by the germanium detector between energies of 200 to 500keV. Several time cuts are applied to help distinguish between atomic transitions and nuclear transitions which are sometimes due to beta decays. However, in this plot, the energy region is mainly populated by peaks that are from muonic x-rays.

muon Al 2p-1s transition unsurprisingly produces the strongest peak in the measurement with an energy of 346.13 keV. There is a background peak from ^{214}Pb at 351 keV. It comes from the ^{238}U decay chain which needs to be considered when counting photons. In addition to the 351 keV peak, within this energy region, the other peaks are the 415 keV and 430 keV, which are from nuclear captures and the 5g-4f Pb transition. The 415 keV Pb peak is very close to the Al 3p-1s with the peaks overlapping each other. The 430 keV is also very close to the next Al 4p-1s transition although still resolvable by eye. The Al 4p-1s is at 435.96 keV and is very close between the Al 3p-1s and the other Pb 5g-4f line at 438 keV. There is nothing else that could be resolved up until the 511 keV single escape peak. On the other side of the Al 2p-1s peak is the ^{206}Pb capture peak of 203 keV and 266 keV. The other peaks are of atomic x-ray origin but remains unidentified for now.

5.3.2 500keV to 1000keV

For energies well above 1022 keV, the dominant photon scattering process in matter is pair production. As it is known, pair production only contributes to the full energy peak when both electron and positron stop in the sensitive volume of the Ge crystal and when the positron annihilation gamma rays are also totally absorbed. Since sometimes one or both of the (usual) two positron annihilation gamma rays escape

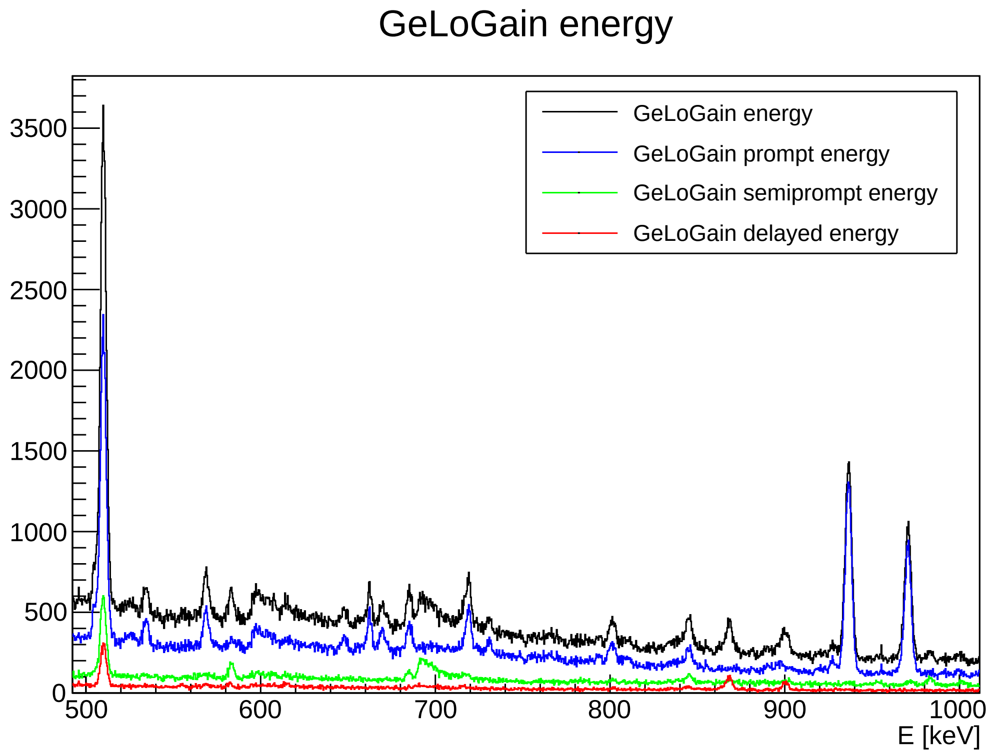

Figure 5.5: X-ray from 500 keV to 1000 keV

the detector, high energy gamma rays typically have first and second escape peaks at 511 and 1022 keV lower than the main peak. The 511 keV peak can be reliably used for calibration. This energy region is also dominated by many prompt x-rays from muon stops in lead. 536.5 keV is a lead peak. There is a semiprompt peak from ^{25}Mg at 580 keV. Another semiprompt peak from excited ^{27}Al is at 844 keV. This peak originates from the process $^{28}\mathtt{Si}(\mu, n\gamma)^{27}$Al. It is not a very intense peak and can only be resolved if the prompt peaks are removed. A high intensity peak at 937.8 keV is from Pb 4f-3d. Another peak at 984.9 keV is from aluminium muon capture from the reaction $^{27}\mathrm{Al}(\mu^-, \nu\gamma)^{27}\mathrm{Mg}$. The neutrino in the muon capture process took a significant amount of momentum in the interaction therefore the neutron did not have enough energy to escape the confines of the nucleus.

5.3.3 1000keV to 2000keV

Several clear and interesting observed peaks are from ^{26}Mg which are from the muon capture in Al, $^{27}\mathtt{Al}(\mu, n\gamma)^{26}$Mg. The 1460 keV peak is a well-known background from ^{40}K. The transition from the first excited to the nuclear ground state emits a 1808 keV gamma. This provides a chance to measure the number of captured muons since it has an intensity of about 51(5)%. The 1130 keV is from the second to the first excited state. It is possible to reach even higher energy levels as we can actually see the transition from the first 3^+ state to the second 2+ state with gamma energy of 1003 keV.

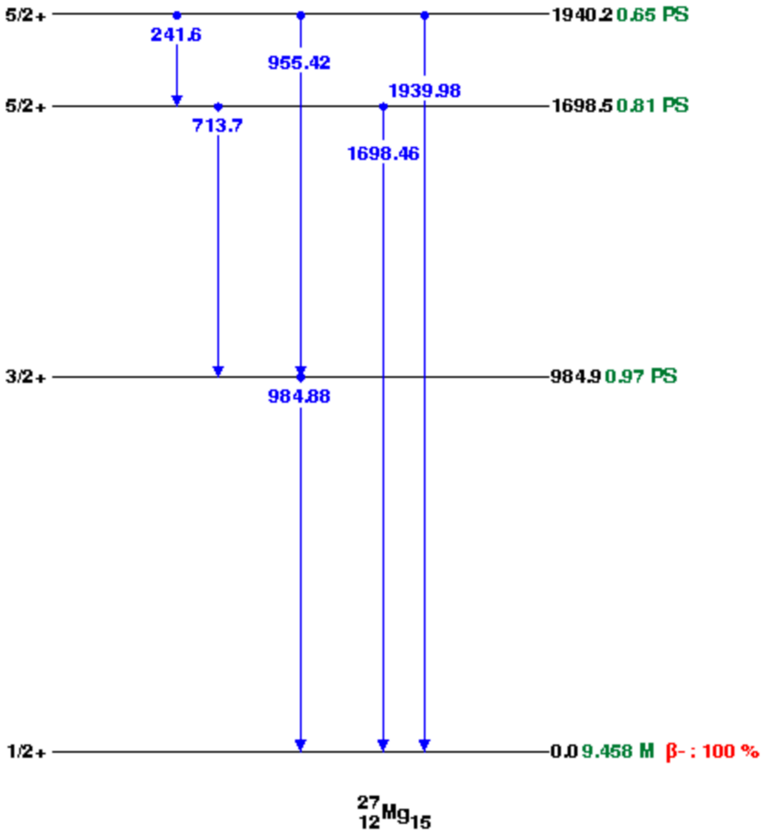

Figure 5.6: ^{27}Mg transitions

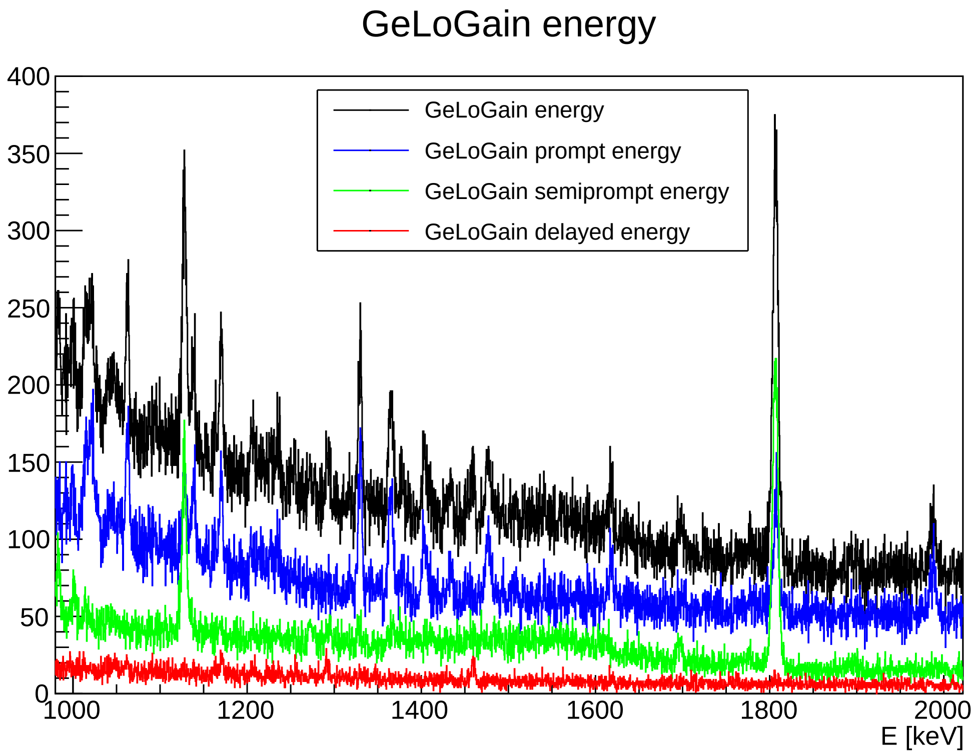

Figure 5.7: Peaks between 1000 keV and 2000 keV.

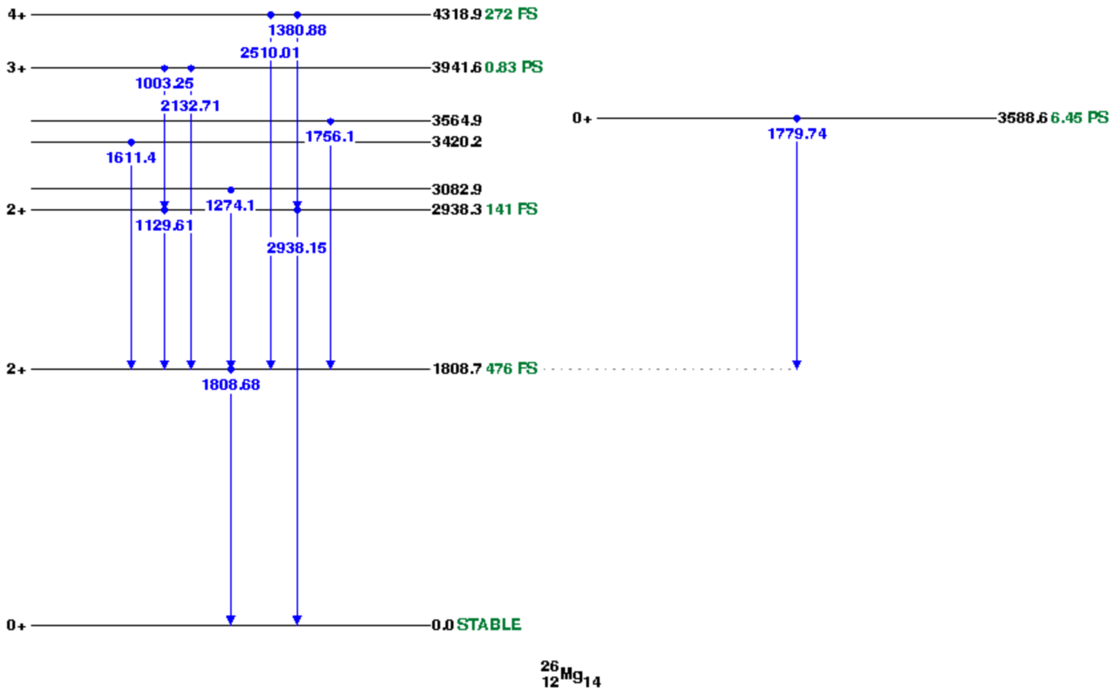

Figure 5.8: ^{26}Mg transitions

5.3.4 2000keV to 3000keV

The other peak that could be observed from ^{26}Mg was the 2510 keV peak which is the transition from the 4^{+} state to the 2^{+} state. Together with the other observed peaks from the lower energies, we have a somewhat good picture of the pathway the nuclei took to be in the ground state.

This peak can be clearly resolved and accounted for during fitting giving an accurate account of the number of x-rays from the muon 2p-1s Al peak minus the background contribution from that particle ^{208}Pb bump.

5.4 Photon counting

The number of x-rays, prompt, semiprompt and delayed photons emitted are taken from the germanium low and high gain channels. These photons may come from atomic or nuclear transitions depending on the time the measurement was made. Typically, the muon when cascading down the atomic energy levels, will emit x-rays. These x-rays may be directly visible by the detector or produce Auger electrons. Here Auger electron emission is assumed to be negligible as aluminium is not a heavy nuclei. The number of muons stopped as seen by the germanium detector is defined to be

$$N_{\mu} = \frac{F_{i \to j}}{A \cdot I \cdot \epsilon} \tag{5.2}$$

where N_{μ} represents the number of stopped muons. The area under the muonic x-ray peak, A is obtained after Gaussian fitting and the detector efficiency, ϵ at that particular energy is from earlier efficiency calibration. $F_{i \to j}$ is the number of counts

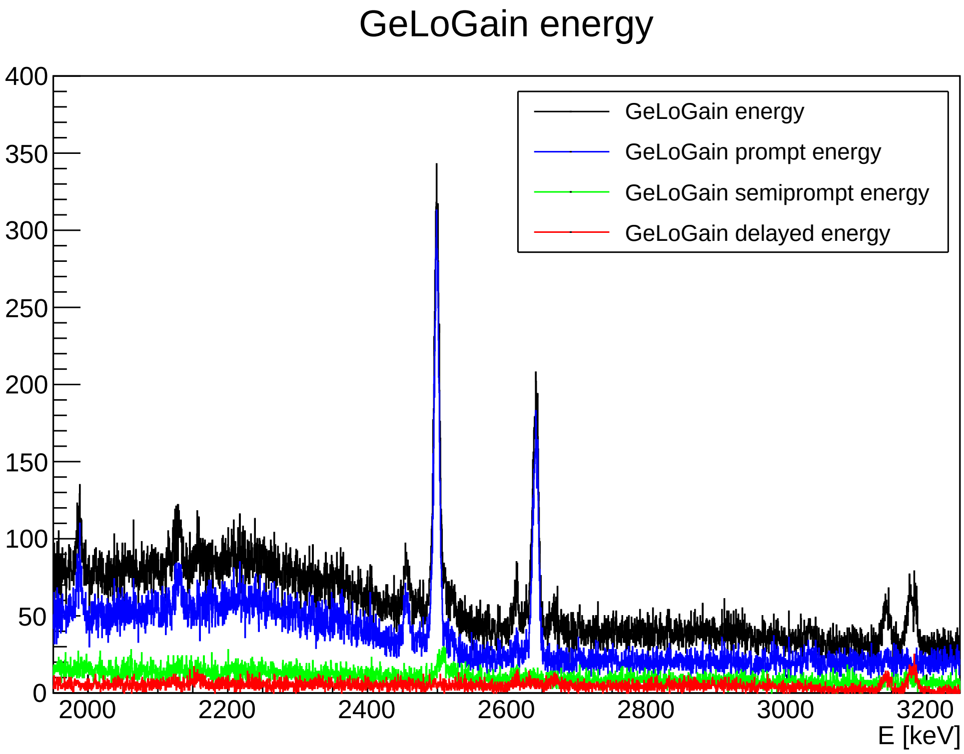

Figure 5.9: X-ray and gamma spectrum from 2000 to 3000keV

obtained from the particular muonic x-ray transitioning from the i-th energy state to the j-th energy state. For ^{27}Al, we look at the muonic 2p-1s peak at 346.828 keV, with intensity 0.798 for getting the number of stopped muons. In addition to that the detector resolution is good enough such that it is possible to resolve several other peaks transitioning down to the muonic 1s state. Atomic transition typically occur in the picosecond frame, so with the application of a very short time cut, e.g. $-200 < t < 200$ns we should still be able to see these photon peaks while reducing semiprompt and delayed contributions. It is however, not possible to identify the 3d-2p transition peak for aluminium since the ADC threshold for the germanium detector was set at 200 keV. The backgrounds in that energy range is also expected to be very complicated and it is not the goal of this experiment to identify those weaker peaks as they would not provide unambigious methods for counting x-rays or gammas from stopped and captured muons. Most of the peaks are contaminated with lead background, so it is necessary to identify all peaks for transitions to the 1s state to provide an accurate number of photons from stopped muons. The muonic x-ray counts from the transitions are also consistent with each other as shown in Table.5.1.

5.4.1 X-rays from muonic atom cascades

Typically the most intense x-ray comes from the 2p-1s transition and for muonic aluminium, is about 346 keV in energy. This is the primary candidate peak for muon normalization. Other peaks are also visible and evaluated in Figures.5.10, 5.11, 5.12 and 5.13. A summary of the results are shown in Table.5.1

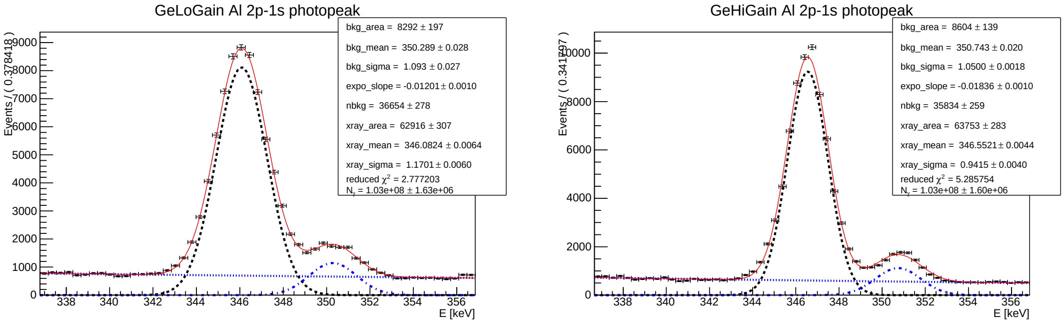

Figure 5.10: The Al 2p-1s peak together with the small 351keV lead background.

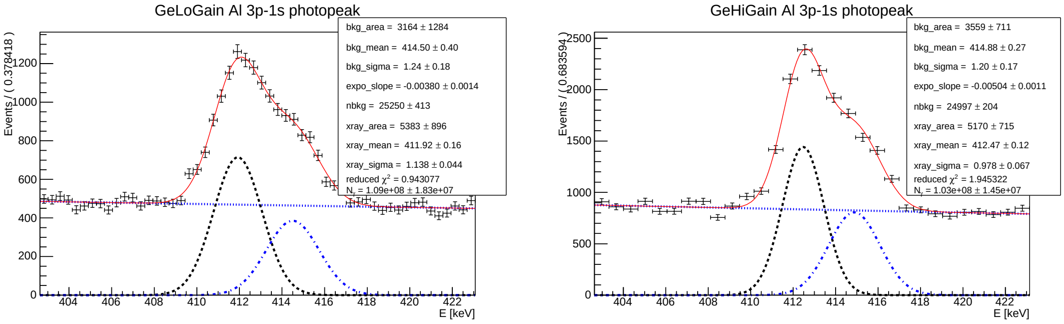

Figure 5.11: Here the lead background is very close to the Al 3p-1s peak.

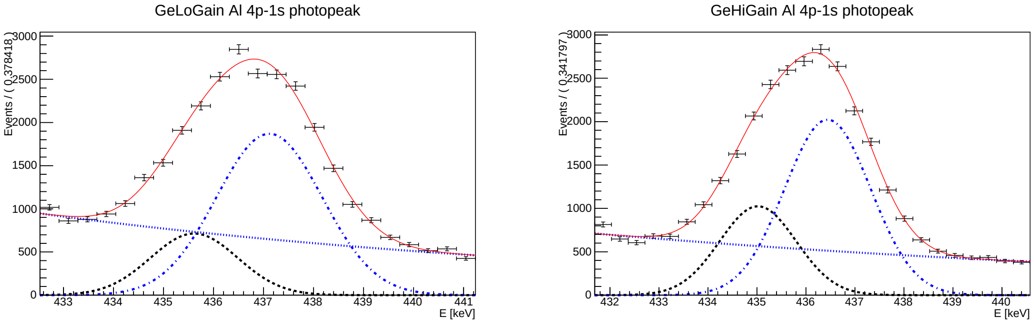

Figure 5.12: The Al 4p-1s peak with the lead background relatively close by.

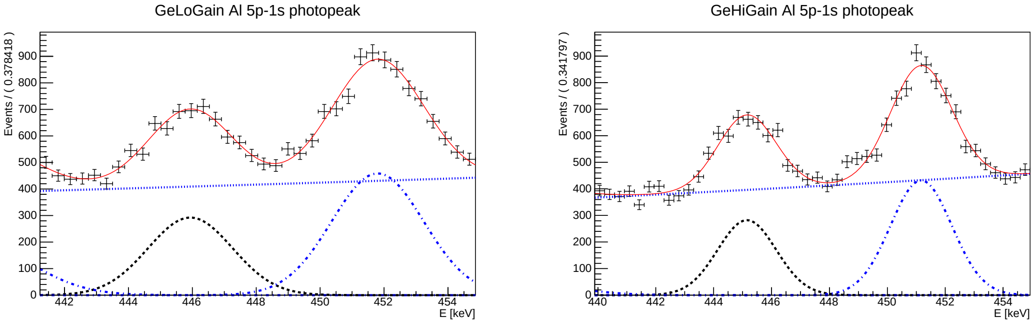

Figure 5.13: The Al 5p-1s peak with the lead background relatively close by.

μ x-ray	Energy [keV]	Intensity [4]	GeLoGain counts ($\times 10^8$)	GeHiGain counts ($\times 10^8$)
2p-1s (Figure.5.10)	346.1759(62)	0.798(8)	1.04(0.02)	1.04(0.02)
3p-1s (Figure.5.11)	412.32(15)	0.0762(15)	1.25(0.14)	1.44(0.05)
4p-1s (Figure.5.12)	435.61(27)	0.0487(10)	1.37(0.83)	1.93(0.57)
5p-1s (Figure.5.13)	445.94(08)	0.0386(10)	1.10(0.32)	0.89(0.13)

Table 5.1: Number of stopped muons derived from the muonic x-ray peak area obtained from gaussian fit function for various energy levels with statistical errors are included in the brackets.

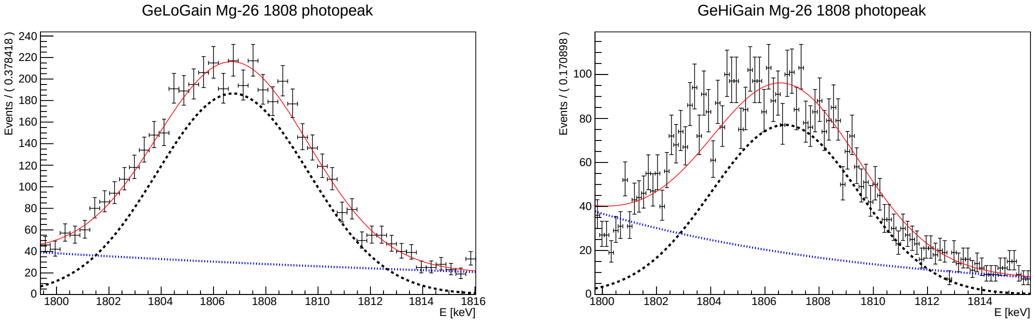

Figure 5.14: The 1808 keV from excited ^{26}Mg transition to the nuclear ground state.

5.4.2 Gamma rays from nuclear transitions

We consider this muon nuclear capture process where the muon reacts with a proton in the nucleus producing a neutron via the weak interaction.

$$^{27}Al + \mu^- \rightarrow ^{26} Mg^* + n + \nu_\mu \tag{5.3}$$

In this case the ^{27}Al will usually turn into an excited state of the ^{26}Mg. This ^{26}Mg is an unstable isotope and has a half-life of about 9 mins. The muon has a reduced lifetime when it is trapped inside an atom. Gamma ray emissions following the capture of muons is delayed by the lifetime of the muon. The semiprompt time cut of $200 < t < 4000$ns is applied to reduce the background from prompt photons which has very high statistics compared to the capture gammas. The prompt photons from muonic cascade can reduced to a very low level, for example, in Figure.5.4.

It may be important to identify the peaks belonging to ^{26}Mg and ^{27}Mg so as to show that there really was neutron emission after muon nuclear capture. The formed daughter nuclei may not necessarily be in the ground state and so, cascades to this ground state will provide more gamma photons for nuclear identification. In this R2015b run, it is not possible to conclusively say anything about neutron emission rates but the first step in charged particle emission involves the interaction of the muon in the atomic orbital with a proton in the aluminium nuclei. Only the R2013 and R2015a runs were equipped with neutron detectors. The ^{26}Mg 1808 keV transition contains a significant amount of statistics however, it is somewhat doppler shifted so the peak energy has a higher uncertainty.

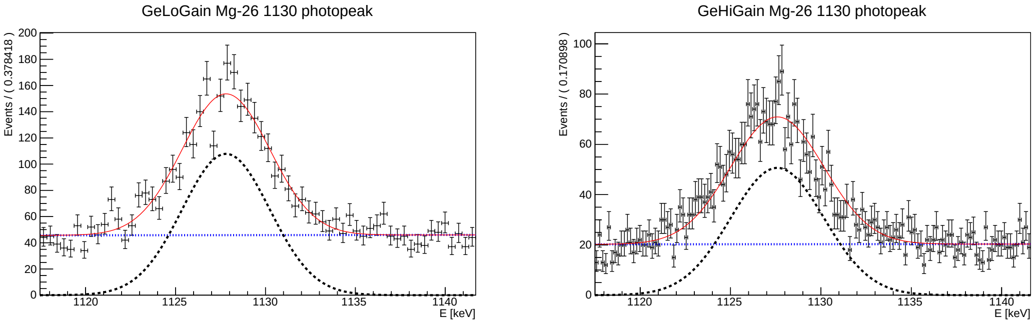

Figure 5.15: The 1130 keV from excited ^{26}Mg transition to the first excited state.

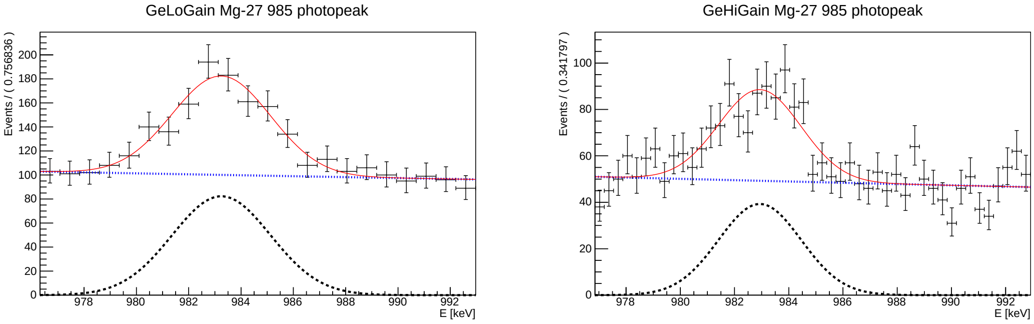

Figure 5.16: The 983 keV from excited ^{27}Mg transition to the first excited state.

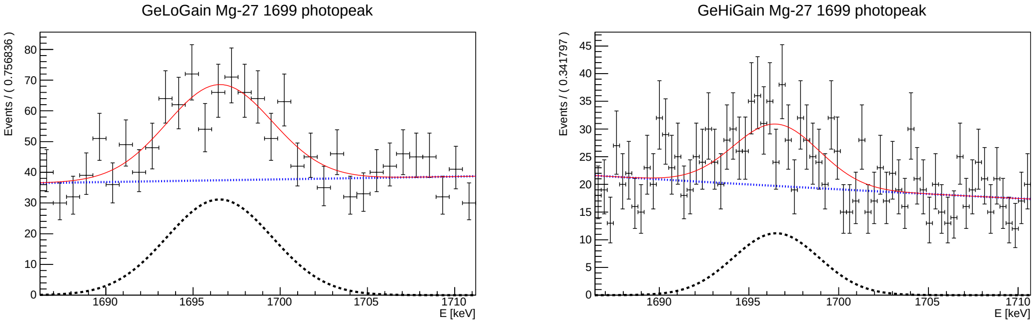

Figure 5.17: The 1696 keV from excited ^{27}Mg transition to the first excited state.

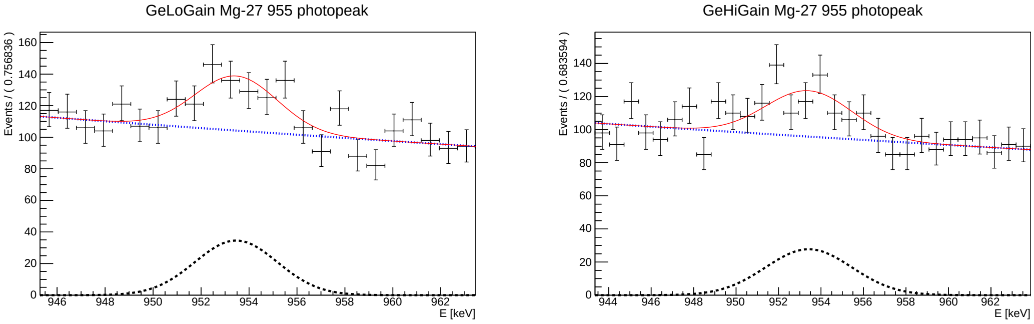

Figure 5.18: The 953 keV from excited ^{27}Mg transition to the first excited state.

Energy [keV]	Intensity [4]	GeLoGain counts ($\times 10^7$)	GeHiGain counts ($\times 10^7$)
^{26}Mg 1806.740(25)	0.51(5)	4.27(0.45)	3.67(0.04)
^{26}Mg 1127.804(99)	0.148(15)	4.64(0.52)	5.10(0.06)
^{27}Mg 983.25(20)	0.032(2)	5.56(0.08)	4.74(0.76)
^{27}Mg 1696.52(51)	0.020(2)	8.98(1.79)	5.67(1.59)
^{27}Mg 953.46(85)	0.0126(6)	5.26(1.34)	5.52(1.51)

Table 5.2: Observed γ-ray yields from selected ^{26}Mg and ^{27}Mg transitions with low backgrounds.

5.5 Number of stopped muons

The muonic x-ray peak from the 2p-1s transition of Figure.5.10 has the least statistical error and from there we obtain a total stopped muon count of $1.04(0.02) \times 10^8$. The muon capture probability of the aluminium nuclei is 0.609[15] and from this the number of captured muons is $6.33(0.10) \times 10^7$.

5.6 Charged particle emission

In addition to neutrons, protons and other charged particles such as deuterons, tritons and alphas could be emitted when a muon interacts with the nucleus of an atom. They can be identified using counter telescopes, a thin and thick detector where the particle deposits some energy in the thin and stops in the thick detector. Every charged particle with different momentum deposits different amounts of energy and so it is possible to identify the particle species from their energy loss profile. Figure.5.19 shows the profile for protons in 1.5 mm silicon. If the momentum of the particles are high such that they do not stop in the thick detector, their ΔE-E profile would not match those that stop.

5.7 PID and selection

First, events from thick detectors are searched for. For such events, the algorithm then tries to find a pulse from the thin detector that occurs within $\pm 2\,\mu$s. This should reduce the amount of noise hits that do not come from charged particles although it is still possible to record charged particles that comes from muon capture in lead or muon scattering. Figure.5.20 shows the results of those cuts. The bands in the figure are identified by comparing with Monte Carlo. The top most band overlaid with the green line are made up of tritons. Going down, the next band overlaid with a blue line are deuterons. Next, overlaid in red are protons. Note that the punch through protons and deuterons mix and they make up the band below the proton band, decreasing in count at lower energies.

Once the bands are identified, cut selection can begin. In Figure.5.21, an ΔE+E slice is taken from 4 to 5 MeV and projected on the ΔE axis. It is clear that the profiles are Gaussian distributed with some mean, μ and spread σ. There is also some overlap between the particle species. For example, choosing a 3σ cut for selecting protons with this method would also select about 2% of deuterons.

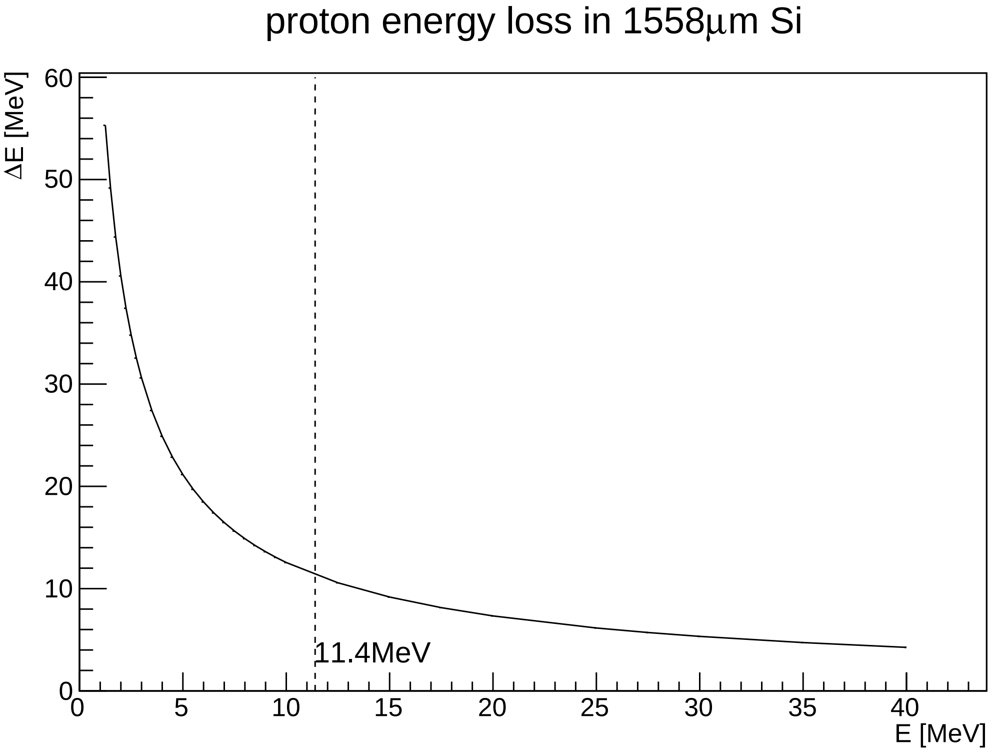

Figure 5.19: Proton energy loss in silicon. The dashed line marks the beginning of punch through protons.

In each energy E bin, particles that lie within ΔE of

$$P = \frac{1}{\sigma\sqrt{2\pi}} e^{(\frac{\Delta E-\mu}{\sigma})^2} < 3\sigma \tag{5.4}$$

are identified as a particular particle type depending on the Monte Carlo. The width of ΔE is set to match the resolution of the silicon thick detector, which was measured to be 85.11 keV using the ^{241}Am alpha source at 5.6 MeV. For protons the method works as expected between the energy ranges of 2.5 to about 10 MeV. Protons with energy of more than 11.4 MeV will begin to be able to pass through the thick silicon detector thus depositing less energy than expected, as shown in Figure.5.19 This is because of the detector resolution for protons at that energy region is a limiting factor for the maximum cut energy. This creates a turning point in the ΔE-E plots. At this limit, the punch through band touches the proton band thus identification of protons at that particular energy becomes uncertain.

Figure.5.23 shows the folded spectra, or measured from the left and right counter telescopes. Figure.5.24 shows the time structure of pulses detected by the left and right counter telescopes when only the proton band is selected. It is fitted with a double exponential and a background where adding the extra exponential fit improves the χ^2 value and also results in obtaining separately the decay constants for muon lifetime in aluminium, 892 ns and also another compound decay constant for both lead and steel, 163 ns.

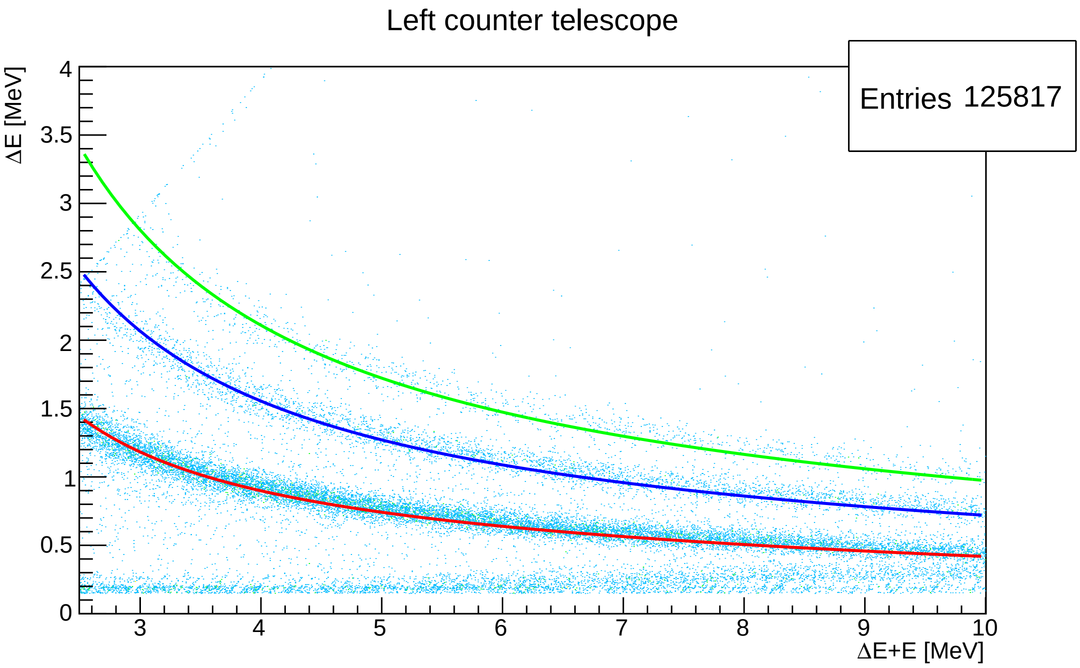

(a) Left counter telescope

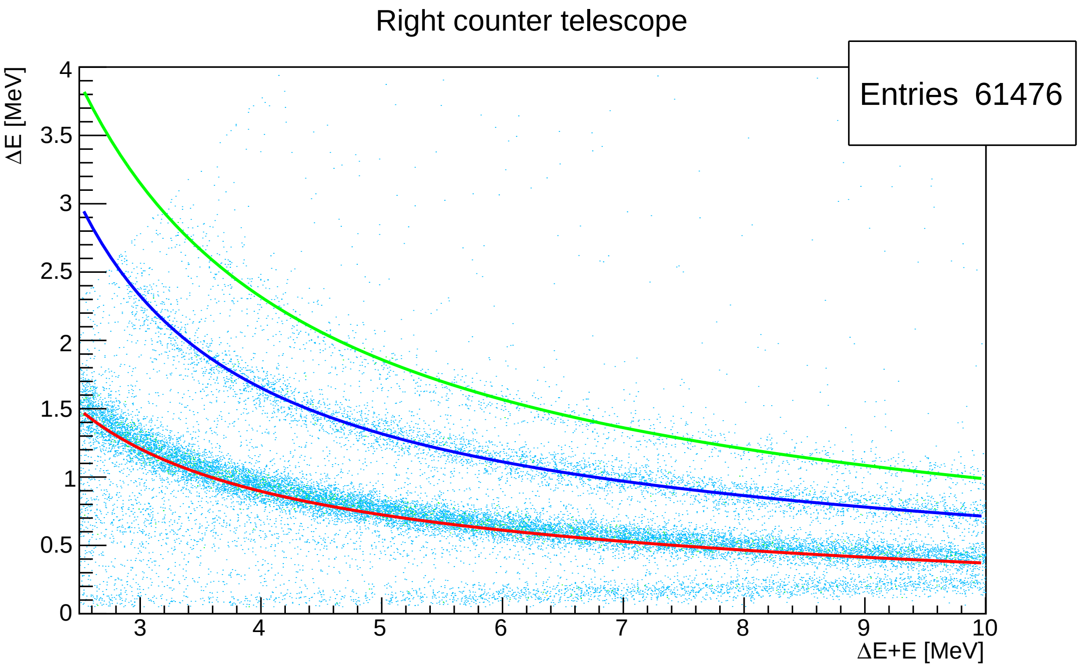

(b) Right counter telescope

Figure 5.20: Based on a Monte Carlo simulation of the experiment, the mean, μ of the energy deposit is decided for each energy bin, E.

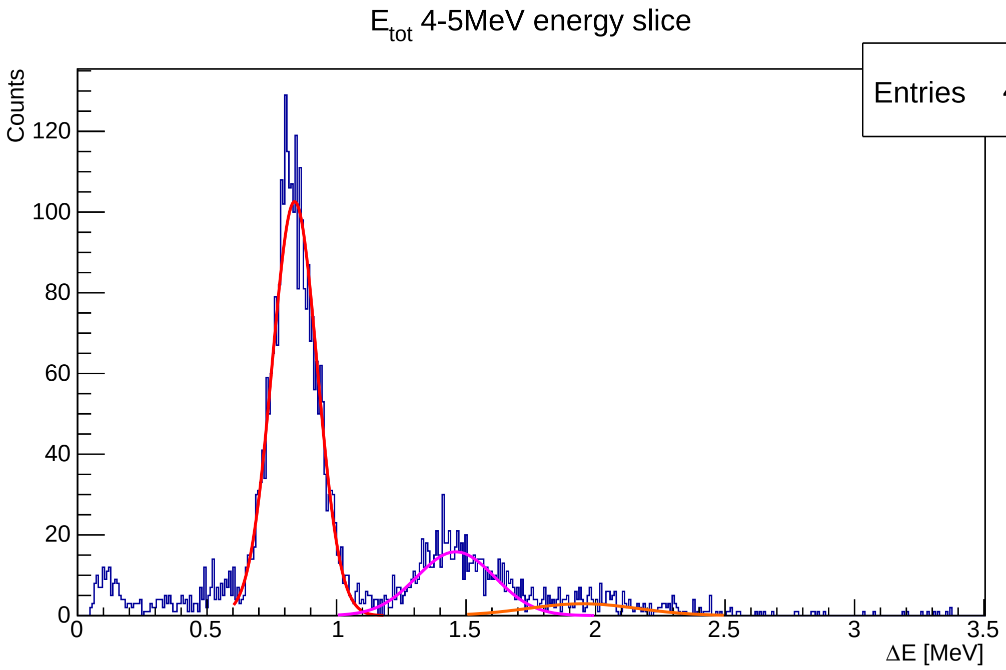

Figure 5.21: ΔE-projection of the $\Delta E - E$ plot for the right counter telescope. Choosing a 3σ cut would select 99% of protons and 2% of deuterons.

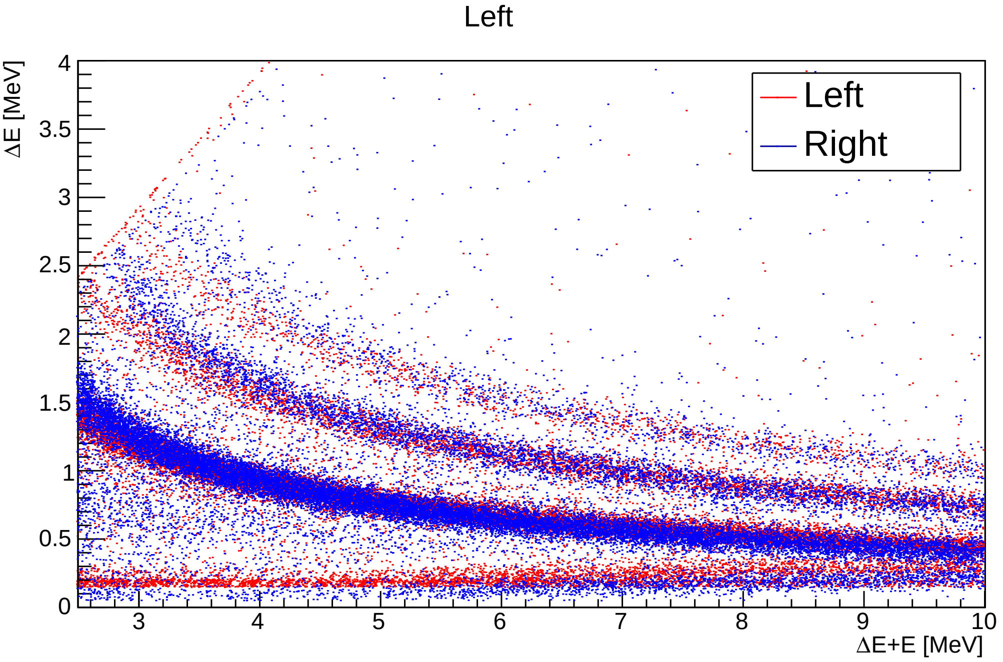

Figure 5.22: There were slight differences in the left and right counter telescope's silicon thicknesses and this is reflected in the slight offset between the two ΔE-E plots for left and right.

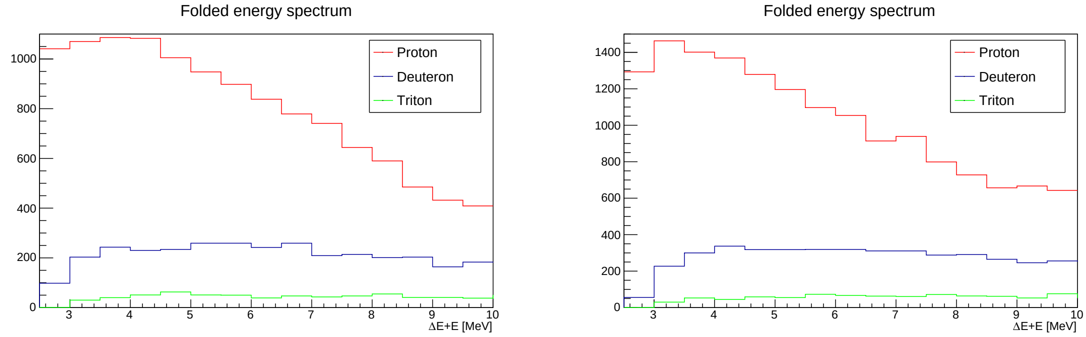

(a) Left counter telescope (b) Right counter telescope

Figure 5.23: Folded charged particle count and energy spectrum from 2.5 to 10 MeV, which may include a negligible amount of punch through particles near the 10 MeV region.

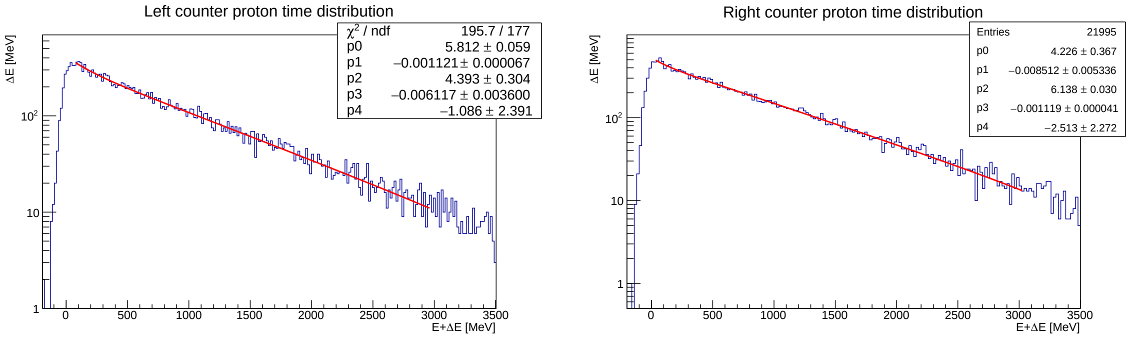

(a) Left counter telescope (b) Right counter telescope

Figure 5.24: The lifetime of muon capture can be verified using proton data selected from the ΔE-E plot

5.7.1 Artificial neural network classifier

(ANN) or deep learning is one of the many algorithms of machine learning. It is not a procedural type algorithm but it tries to train itself from existing known datasets to predict or classify other similar datasets. Neural networks are good with analysis of big datasets which is prevalent in nuclear and particle physics where data sizes regularly reach terabyte or petabyte levels. Generally, it starts with a hypothesis or model, $h(\bar{x}, \theta)$ of the dataset, $\bar{x}$ where θ is a vector of the parameters of the model. The algorithm also requires a training dataset includes truth infomation and is used to calculate the error of the model. This is the feed-forward part of the algorithm. After obtaining the error of the model, the algorithm will try to minimize this error by adjusting the parameters' weights and biases in the backpropagation or learning process.

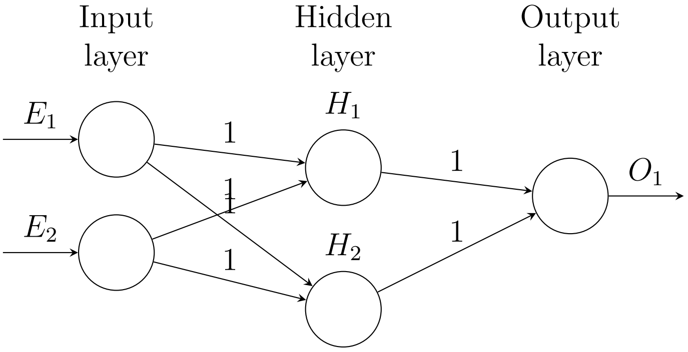

The architecture of a neural network is modelled after the neurons of a biological brain. It consists of neurons and synapses which are the nodes and connections of the artificial neural network. An ANN usually has an input layer which contains nodes that represent the input variables of the network. It may or may not contain intermediate layer(s) that are used to automate processes that identify hidden features of the dataset. These hidden layers are important to the network to be able to process linear nonseparable problems. A simple example of a linear nonseparable dataset would be the output of the XOR gate. It is not possible to separate the output of the XOR gate with one linear equation. Following the hidden layer(s) is the final output layer which provides the parameters of the model that could fit the dataset.

For simplicity, consider a model with two variables, $\bar{x} = [x_1, x_2]^T$. A possible function $h(\bar{x}, \theta$ with $\theta = [\theta_0, \theta_1, \theta_2]^T$ is maybe possible to classify the data such that

$$h(\bar{x}, \theta) = \begin{cases} 1, \text{ if } \theta_0 + \theta_1 x_1 + \theta_2 x_2 < 0 \\ 0, \text{ otherwise} \end{cases} \tag{5.5}$$

This describes a linear equation that divides the plane into two halves and essentially categorizes the datset. Given a new data point, $\bar{x_n} = [x_n, x_n]^T$, the machine learning model will be able to predict the correct category which the data point belongs to.

5.7.2 Feed-forward network

A feed-forward network has connections between nodes of different layers. It has no connections between nodes in the same layer and information traverses only in the forward direction from the input to the output layer. The are no rules in determining the umber of hidden layers in the network and its optimization is more of an art that comes from experience. We can translate the neural network as a series of vector and matrix operations for ease in applying it in computer programs, $f(w^T\bar{x}+\bar{b}) = \bar{y}$. The nodal activation function $f(Z)$, where $Z = \Sigma_k w_k x_k + b_k$ can be of many types such as sigmoid, tanh, or Restricted Linear Unit(ReLu). In the context of this work, the sigmoid function is used.

$$f(Z) = \frac{1}{1+e^{-Z}} \tag{5.6}$$

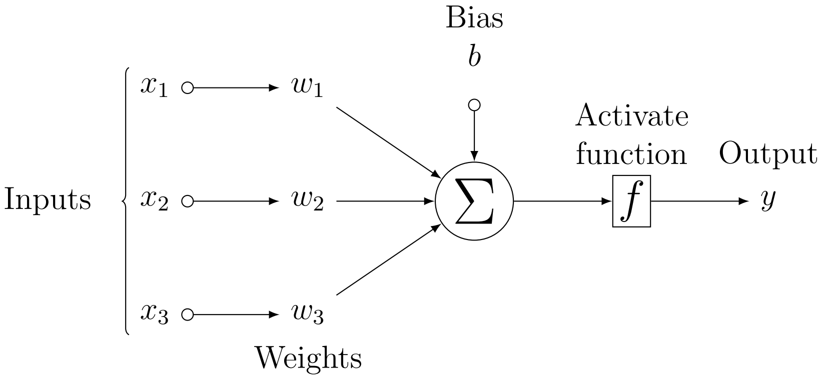

Instead of using a linear activation function like in linear regression, we instead use a sign function. Recall the definition of the sign function:

$$sign(w^T x_i = \begin{cases} 1, & \text{if } w^T x_i > 0 \\ 0, & \text{if } w^T x_i = 0 \\ -1, & \text{if } w^T x_i < 0 \end{cases} \tag{5.7}$$

For classification tasks, the output probabilities are required over a set of mutually exclusive labels, e.g. signal and background.

$$\Sigma_i P_i = P_s + P_b = 1 \tag{5.8}$$

This is achievable using a special output layer called a softmax layer.

$$y_i = \frac{e^{Z_i}}{\Sigma_j e^{Z_j}} \tag{5.9}$$

5.7.3 Training and error

We know the correct answer so it is possible to provide feedback to the network. It is convenient to define the error function to be

$$E = \frac{1}{2}\Sigma_i (t_i - y_i)^2 \tag{5.10}$$

where t_i is the truth value for the ith training sample and y_i the value computed by the neural network. The error is reduced as much as possible to zero and the model parameters, $\bar{\theta}$ is the read out. This is not an easy problem that can be solved by a system of linear equations since the activation functions used are nonlinear. In addition, there might not be a solution to the feed-forward matrix equation. Gradient descent is used for minimizing the error, or to search for the global minimum in the multidimensional space of model parameters, $\bar{\theta}$. The derivative or gradient of the error is used to determine the direction. The starting point of the algorithm is determined randomly and moves to a new parameter value in the direction of the error gradient with some step size. This step size is equivalent to the learning rate of the algorithm and is difficult to determine. In machine learning jargon, the learning rate or delta is one of the hyperparameters that need to be set in addition to the input parameters. If the learning rate is set to small, the learning process could take a very long time to converge and if set too high, the gradient descent might diverge from the solution. The rule for modifying weights during the training phase of the neural network with sigmodal nodes is

$$\Delta w_k = \Sigma \epsilon (x_k)_i y_i (1 - y_i)(t_i - y_i) \tag{5.11}$$

5.7.4 Backpropagation

Using the gradient descent method or some other error minimization, it is possible to find the path of steepest descent by figuring out how fast the error changes when weights are changed for the neural network. Backpropagation modifies the weights of the connections after each trainig sample,

$$\Delta w_{ij} = -\Sigma_{k \in dataset} \epsilon (y_i)_k (y_j)_k (1 - (y_j)_k) \frac{E_k}{(y_j)_k} \tag{5.12}$$

The batch gradient descent method demonstrated above is sensitive to saddle points and thus might lead to premature convergence before finding the global minima. The stochastic gradient descent method can be used to overcome this problem as it estimates the error hypersurface for a single training data point but it may not be a good approximation of the error hypersurface. Therefore to reach a compromise, the mini-batch gradient descent method is used by running the gradient descent on a smaller subset of the dataset and estimating the error hypersurface. The ROOT analysis package implemented the Broyden-Fletcher-Golfarb-Shanno(BFGS) method that is powerful iterative method for solving unconstrained nonlinear optimization problems like the one for neural networks. This optimization or learning method will be used to perform classification and unfolding in this work.

5.7.5 Data classification

Firstly, the network architecture is described. There are two input nodes, the energy deposit in the thin detector and the energy deposit of the particle in the thick detector. There are 12 hidden nodes in the only one hidden layer. Each node in the hidden layer would represent a line in 2-D space since there are only two input nodes used which also represents the input space. There would be several different lines with the form $h(w, x) = w_0 x_0 + w_1 x_1$. where the weight and bias values are changed during training. These are then combined in the output node. There is only one softmax output node that provides the value of the neural network evaluation which we then select a NN cut of between zero and one and should be able to obtain a clean classification of particles.

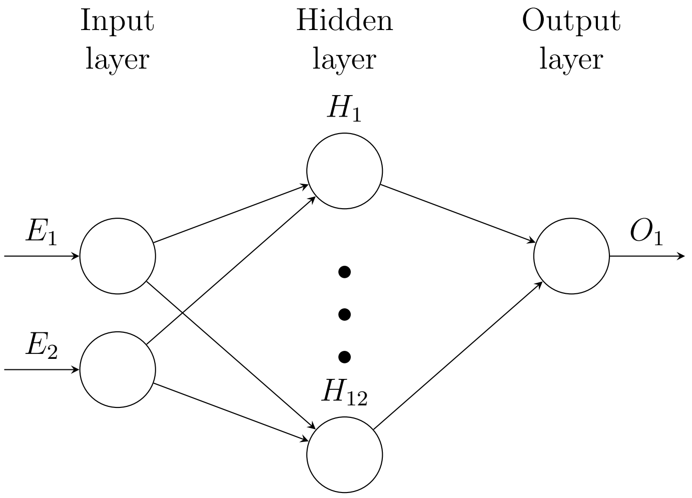

Training data is generated using Monte Carlo. Electrons, protons, muons, pions, protons, deuterons, tritons and alphas are all generated with various energy ranges and with a uniform distribution. Punch through protons are also generated but they are labelled as background. The signal and background datasets are determined separately during each training session as different charged particles can be treated as signal in different training sessions. The neural network is trained using the Monte Carlo truth dataset for 5000 epochs, which is the number of training and test cycles.

5.8 Evaluation using Monte Carlo

First, it is desirable to make sure that we trained the neural network properly but applying it also on another Monte Carlo generated dataset. This way, it is possible to evaluate the correctness of the classification, especially near the particle punch through area, for protons, is about 10 MeV. In principle it should be possible with any charged particle detectable by the silicon detectors.

Hence, there is some chance of energy misindentification after 10 MeV for protons. It is estimated to be less than 5% at energies less than 12 MeV. This rises to an average of 10% from 12 to 16 MeV. The main advantage of the neural network method is the ability to select non-punch through charged particles. The identification for protons near and in the punch through regions are important for the counter telescopes since there is no other way of extending the proton energy spectrum. First a test distribution with known truth values are generated using Monte Carlo. The same neural network classification code will also be used for data level classification.

5.9 Unfolding

Unfolding is necessary to obtain the true initial particle energy. Muons that hit the surface of the target mostly but there is a skin-effect and some of the muons reach deeper into the material. The target material is passive so there is no way to know experimentally where inside the material the muon is captured by the nuclei. Particles emitted after muon decay or nuclear capture would also lose energy inside

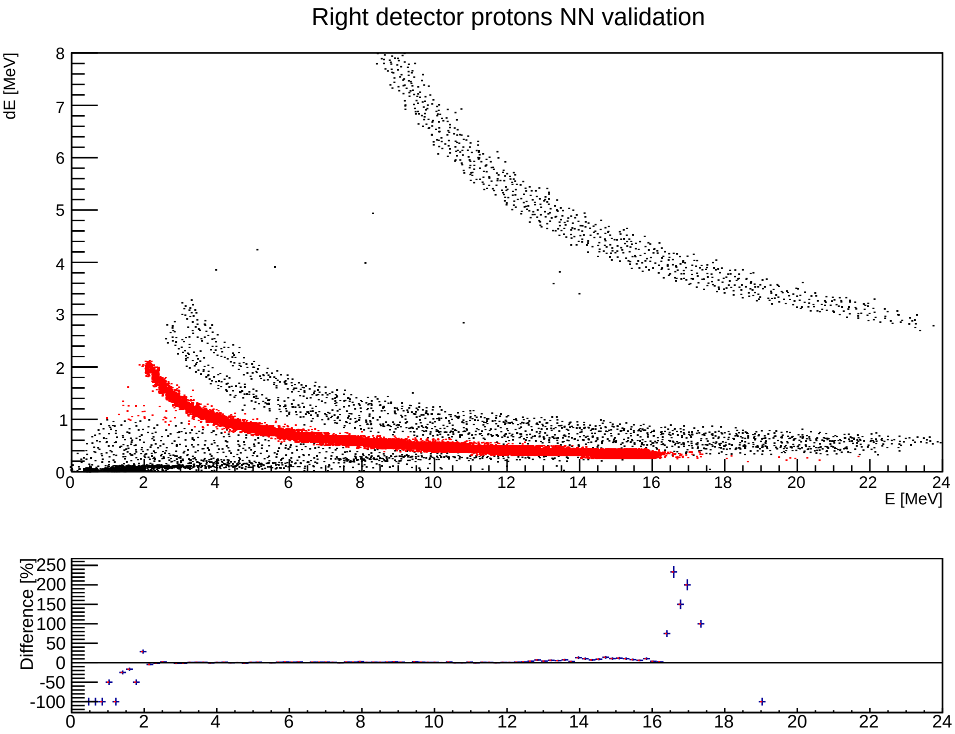

Figure 5.25: The classification was done very well up to the punch through area where it started to show some signs of deviation from the truth values.

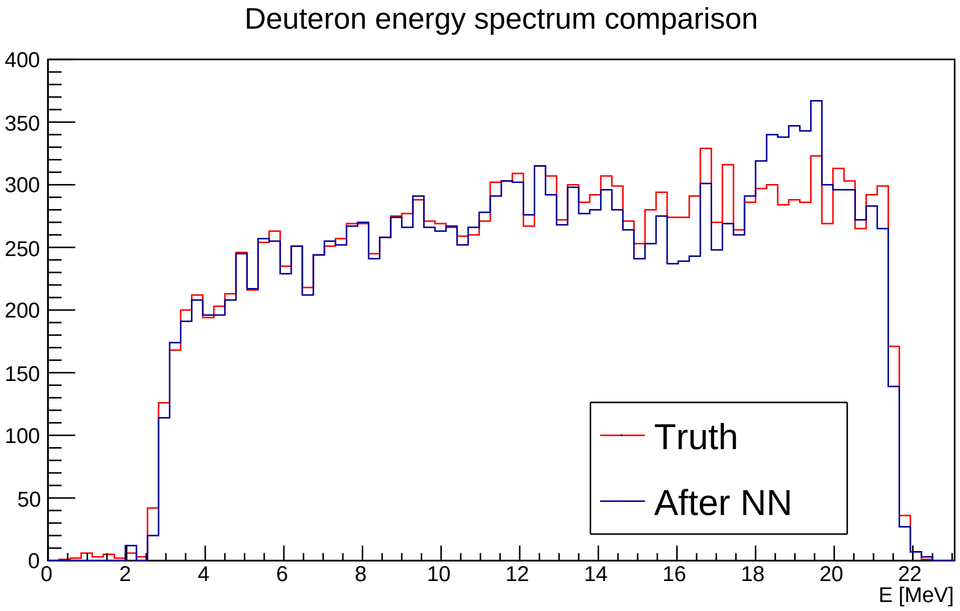

Figure 5.26: A comparison of the proton truth dataset and the test dataset after classification.

the material. In this case, we are more interested in charged particles so they actually lose more energy due to the Coulomb interaction. Monte carlo simulations show that protons lose about 1 to 3 MeV for energies less than 10MeV. The main purpose of the AlCap experiment was to find out this true proton energy spectrum so it is important to perform deconvolution or unfolding of the counter telescope energy measurement. It may be more difficult to smear a theoretical model of the energy spectrum since we have very little idea of how exactly it looks like and the detector effects may be too complicated to just apply a noise smear.

5.9.1 Bayesian inference

Bayes' rule is used to infer model parameters from data.

$$P(\text{model}|\text{data}) = \frac{P(\text{data}|\text{model})P(\text{model})}{P(\text{data})} \tag{5.13}$$

which means the posterior probability of a physical model is equal to the likelihood function of the data, $P(\text{data}|\text{model})$ multiplied by the prior probability of the model normalized by current observations of the data. The $P(\text{data}|\text{model})$ can be obtained from Monte Carlo simulations of experimental conditions. It is important to use conditions and setup the Monte Carlo simulation to be as close as possible to the conditions of the experiment. This includes knowledge of the beam profile and energies. Unfortunately for passive targets like aluminium, it is not possible to know with high certainty the muon stopping depth. During the experimental runs, the beam was tuned such that it stopped near the middle of the target, so the Monte Carlo simulation should also obtain similar results. The geometrical orientations of all detectors, shields and positions should also be modelled as precisely as possible.

From muon beam measurements, the profile was measured as shown in Figure.5.3. The muon beam energy right before hitting the aluminium target is measured to be 1.39 MeV with a energy spread of 0.211 MeV based on the muon punch through energies. Together with this measured beam profile, it is possible to obtain the muon stopping depth in the target using Monte Carlo. This is shown in Figure.5.27. The muon stopping positions are assumed to be the charged particles emission initial positions. For the purposes of generating the response matrix, a uniform energy distribution from 0 to 18 MeV is used as the initial energies of the charged particles. These assumptions are then tested by generating a few Monte Carlo events using known energy distributions. Such response matrices includes the geometrical acceptance since they were generated with appropriate geometry.

A test of the Bayesian method is done by generating particles emitted from the muon stopping target region of the Monte Carlo simulation with known energy distribution. The unfolding algorithm used should be able to recover the original truth energy distribution.

The response matrix in Figure.5.28 is obtained from a Monte carlo simulation with initial conditions obtained from the entrance detector and verified from other muon beam scan measurements.

Several test results with the said known energy distributions are shown in Figure.5.29. Although the initial energy of protons are uniformly distributed, the measured test spectra was correctly unfolded to recover the truth energy.

The $\Delta E + E$ projection of the particle bands that were identified earlier using likelihood probability cuts are the energies of the charged particle that have been

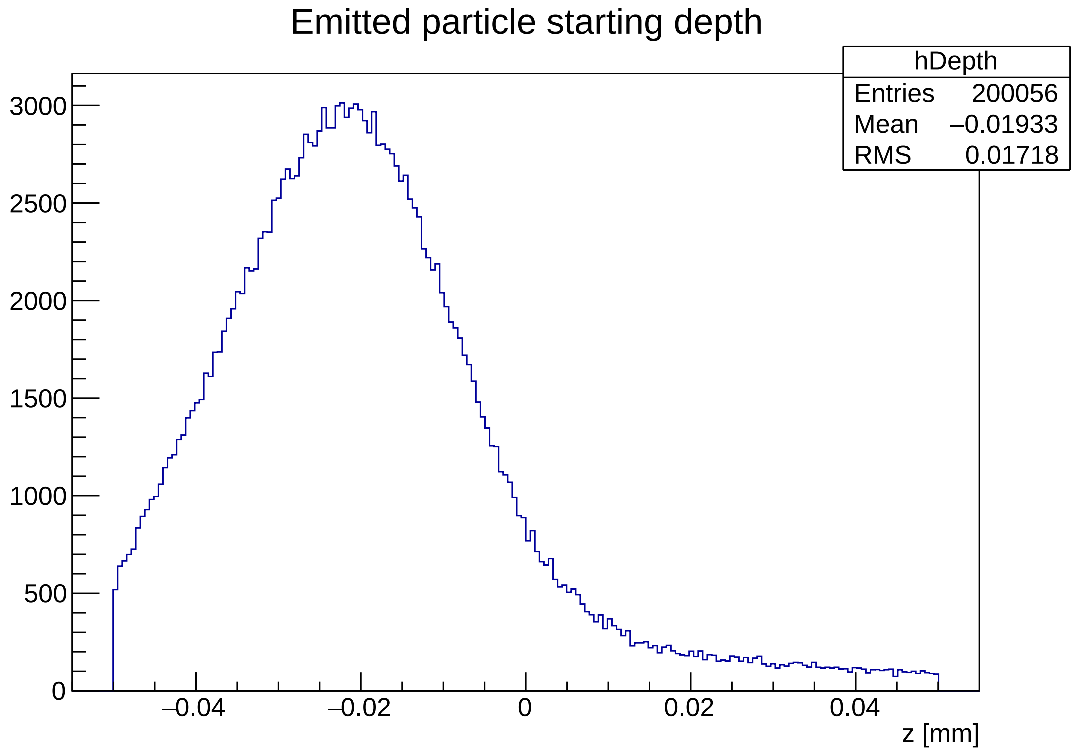

Figure 5.27: The estimated muon stopping depth in the Al target.

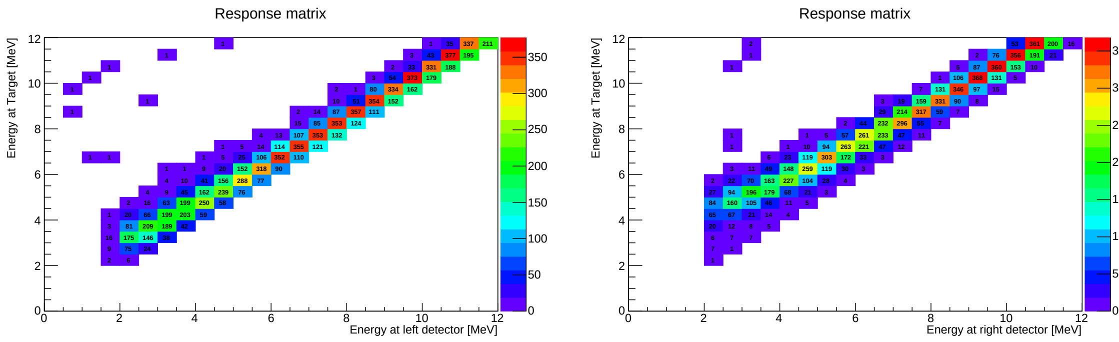

(a) Left (b) Right

Figure 5.28: The response matrices for the counter telescopes that maps true to measured values for protons. Bin size is set to 500 keV.

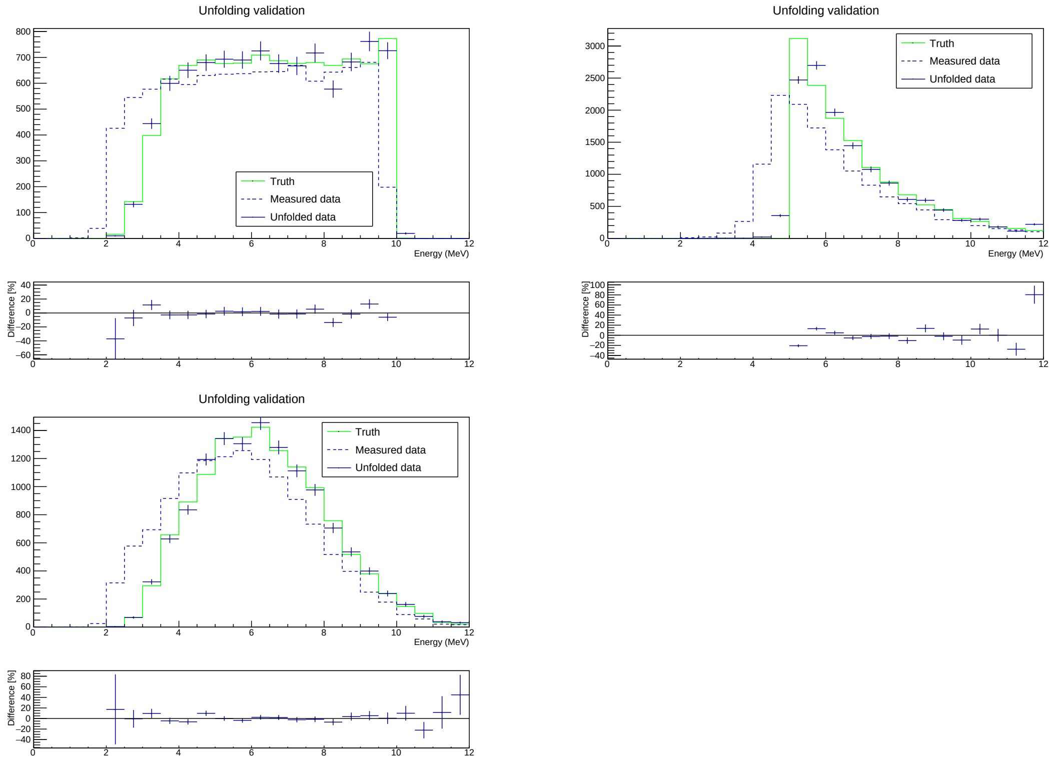

Figure 5.29: A test with a Monte Carlo uniform, exponential and gaussian distributions

convoluted with noise and detector effects as well as reduced when those particles lost energy while traversing through the alumnium target. The following figures 5.30, 5.31, 5.32 show the Bayesian unfolding results using the RooBayes packages in RooUnfold[44].

5.9.2 Artificial neural network unfolding

The multilayer perceptron neural network has been used in particle physics for quite some time[45] for event classification and function approximation. In addition, neural networks has been used to unfold photon and neutron spectra[46] although the network used was a much simpler one. Recently it has also been used in pulse analysis[47] from solid state detectors at the FAIR facility in Germany.

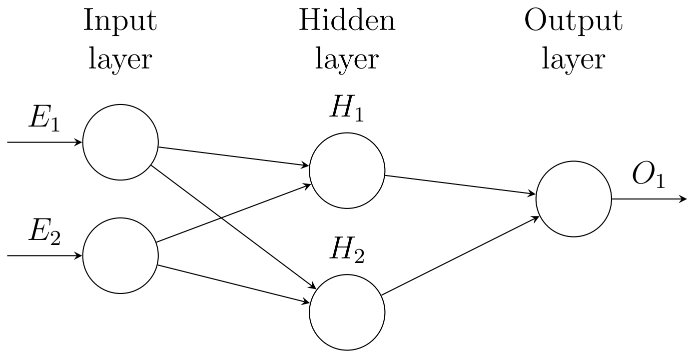

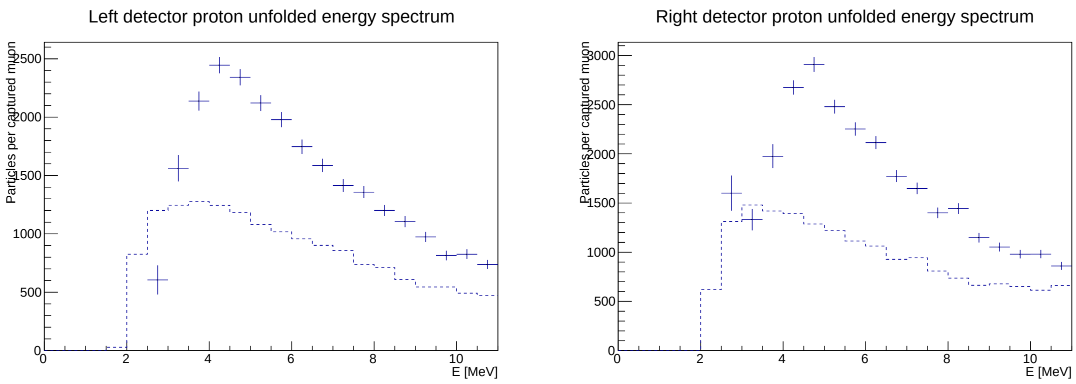

Figure 5.30: Left and right counter unfolding with Bayesian inference. Total number of protons emitted between 2.5 and 10 MeV per stopped muon as seen by the left counter is 24218(277) and the right counter 27764(324).

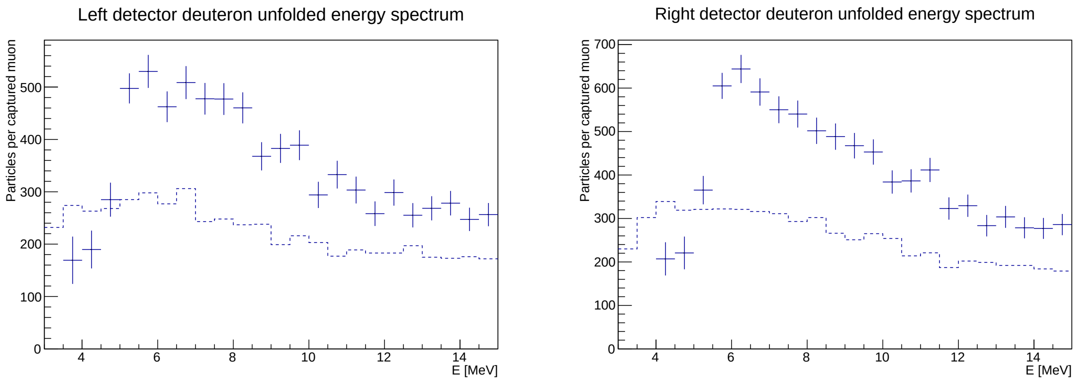

Figure 5.31: Left and right counter unfolding with Bayesian inference. Total number of deuterons emitted between 2.5 and 15 MeV per stopped muon as seen by the left counter is 5491(117) and the right counter 6018(114).

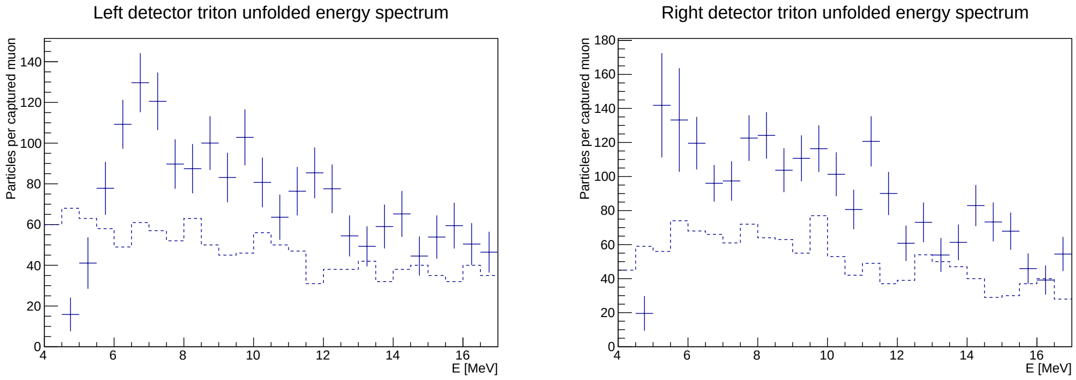

Figure 5.32: Left and right counter unfolding with Bayesian inference. Total number of tritons emitted between 2.5 and 10.5 MeV per stopped muon as seen by the left counter is 1038(44) and the right counter 1286(59).

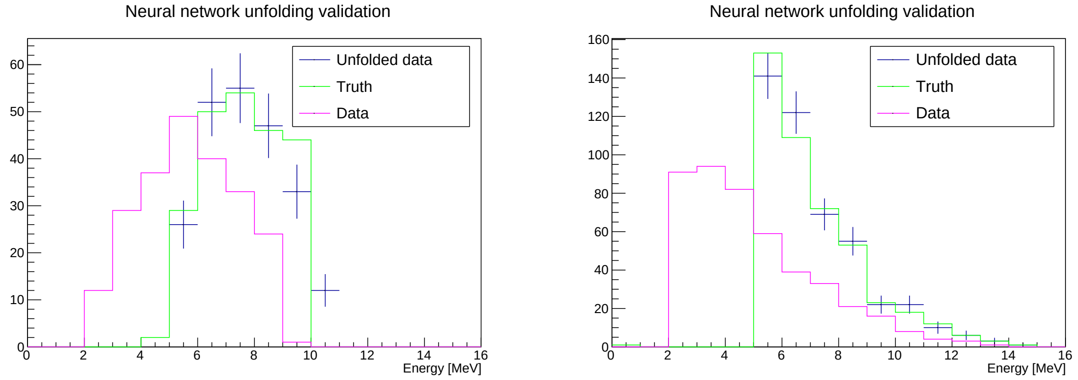

(a) Uniform (b) Exponential

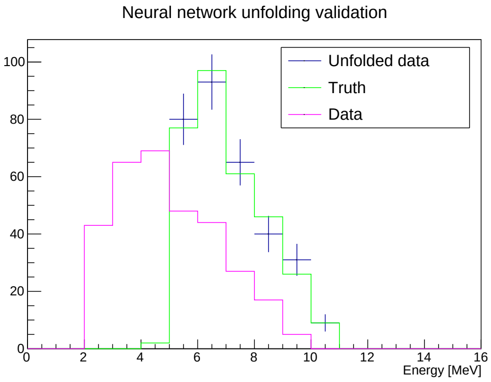

(c) Gaussian

Figure 5.33: Tests with uniform, exponential and gaussian distribution. Similar tests with Bayesian but using neural network.

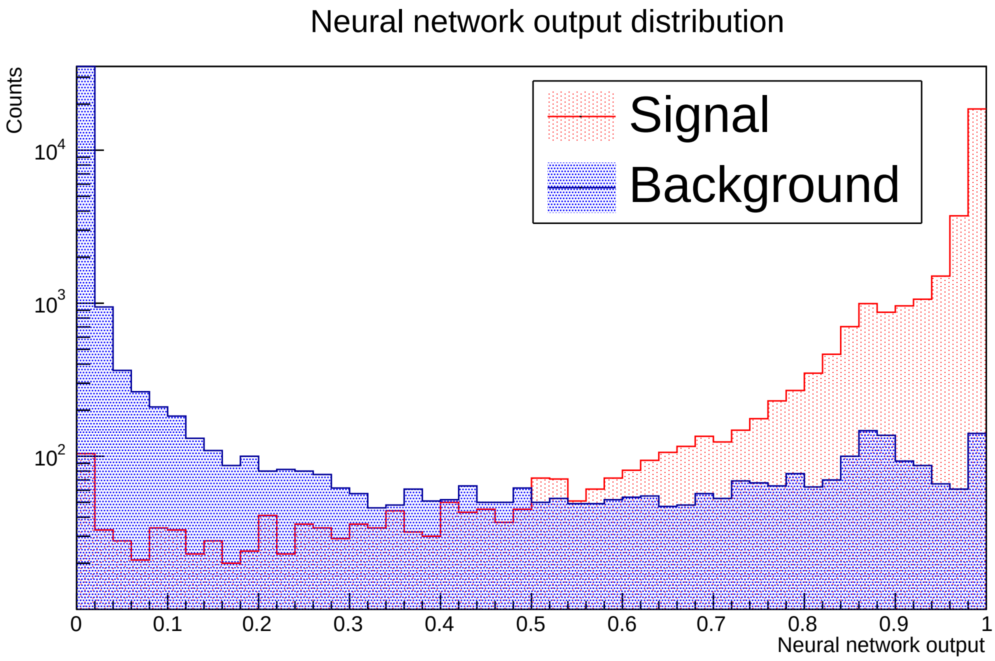

(a) Background and signal distribution

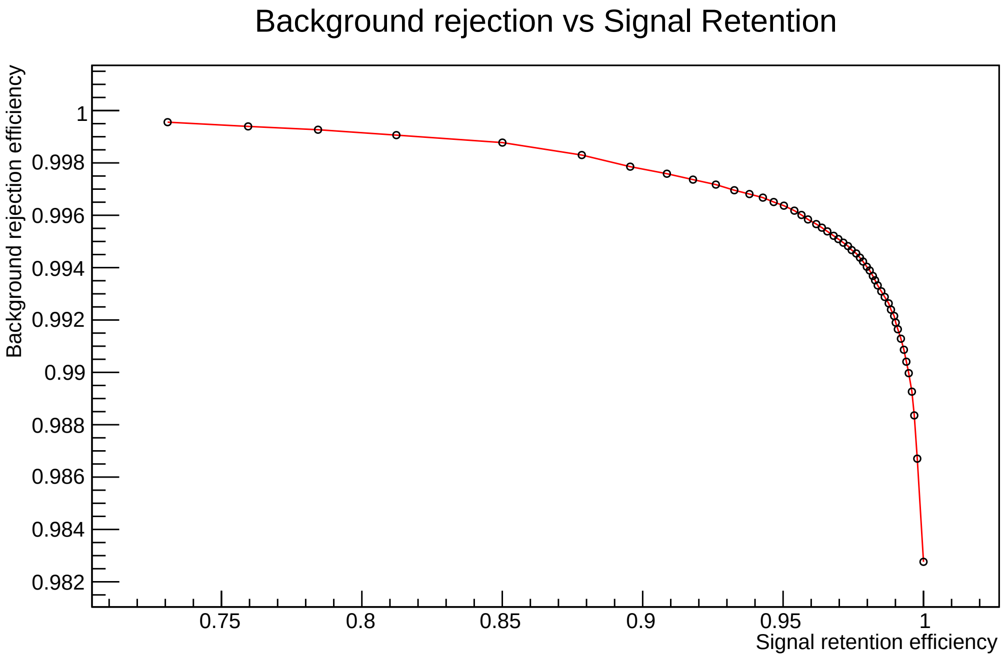

(b) Optimal point for signal retention is 0.48.

Figure 5.34: Distribution of background and signal protons as identified by the neural network on Monte Carlo truth dataset.

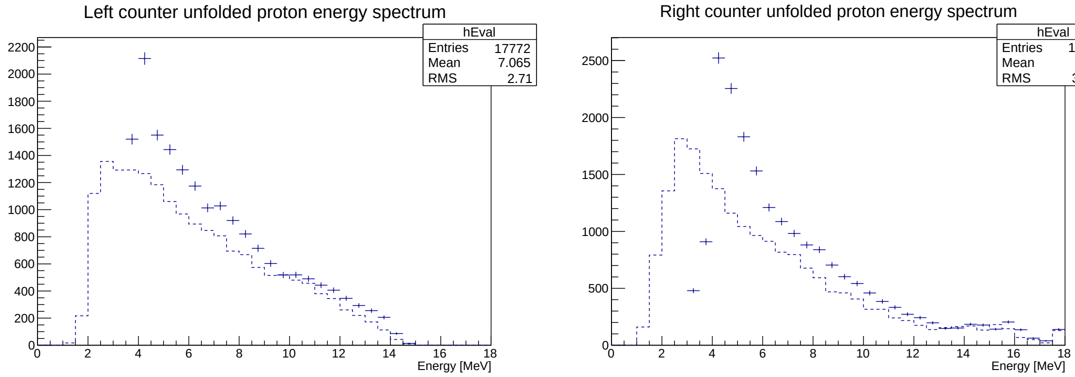

Figure 5.35: Protons from the left and right counter as picked out by the neural network. Left 14912(122) and Right 14378(120).

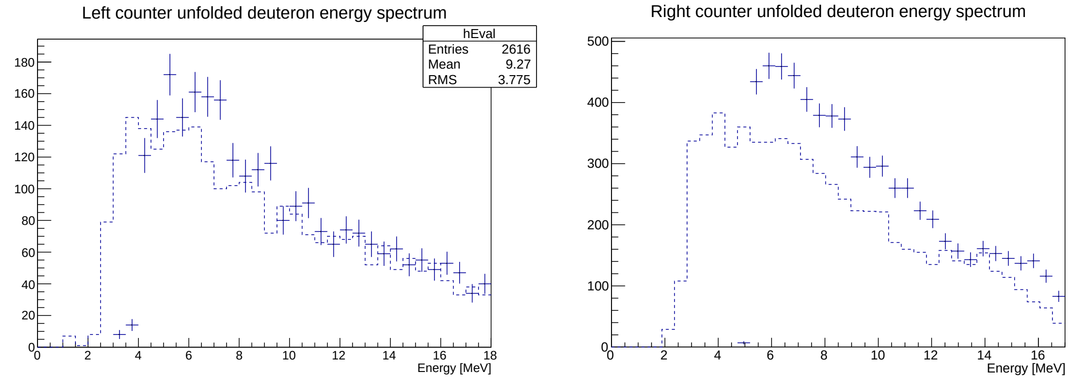

Figure 5.36: Folded and unfolded deuteron spectra from the left and right counter. Left 4033(64) and Right 4240(65).

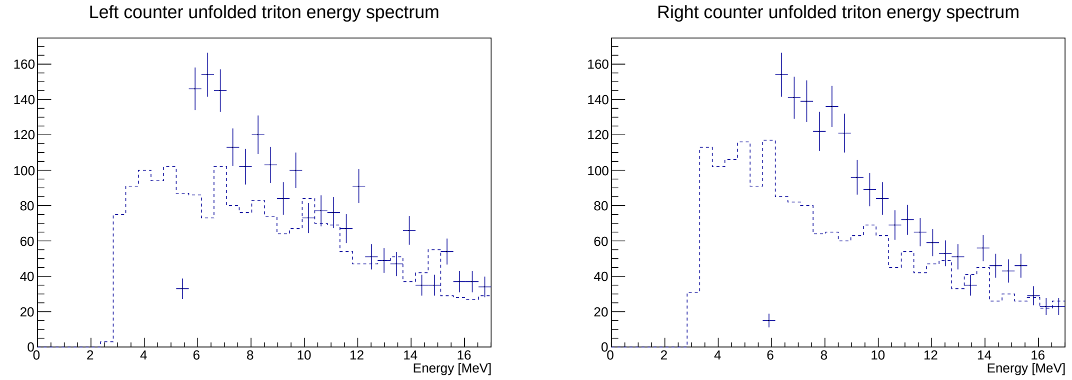

Figure 5.37: Folded and unfolded triton spectra from the left and right counter. Left 1173(34) and Right 1097(33).

Chapter 6

Results

6.1 R2015b results

Number of stopped muons obtained from the counting 2p-1s x-rays from the germanium detector is 1.042×10^8. This number is used for figuring out the number of charged particle emission per stopped muon. The number of muons that are captured is 60.9% of stopped muons[15]. The energy spectrum is then fit with Equation.2.5. For the most part, the function worked well for protons as the data points have sufficient statistics to trace out a clear shape. It is clear both the left and right counter telescopes see a proton peak energy at 4 MeV and a threshold energy of 2.5 MeV. It partially worked for deuterons, where the function worked in the energies after the 6 MeV peak but not so much for lower energies due to insufficient statistics. The threshold energy for deuterons is estimated to be at about 4 MeV. However, the statistics for tritons are insufficient for fitting with Equation.6.1, the low energy spectrum shape is not sufficiently clear for the minimization algorithm, MINUIT to work.

$$p(T) = A\left(1 - \frac{T_{th}}{T}\right)^{\alpha} e^{-\frac{T}{T_0}} \tag{6.1}$$

From the unfolded charged particle energy spectrum, the total emitted particle number is then estimated. Assuming isotropic emission from the target region, it is possible to estimate the total number of charged-particle emission by multiplying with a geometrical scaling factor,

$$F = \frac{4\pi R^2}{A} \tag{6.2}$$

where the distance of the right counter from the center of the target, R_{right} =120.8 mm

Particle	$A \times 10^{-5}$	T_{th} [MeV]	α	T_0 [MeV]
Proton left	31.2(13.2)	2.9(0.2)	0.17(0.03)	3.12(0.44)
Proton right	16.3(1.75)	2.71(0.03)	0.55(0.07)	4.37(0.20)
Deuteron left	5.89(1.32)	4.02(0.12)	0.82(0.14)	5.92(0.45)
Deuteron right	2.88(0.49)	3.59(0.12)	0.62(0.13)	7.90(0.75)

Table 6.1: Fit parameters used for fitting unfolded proton and deuteron energy spectrum in Figures.6.1 and 6.2.

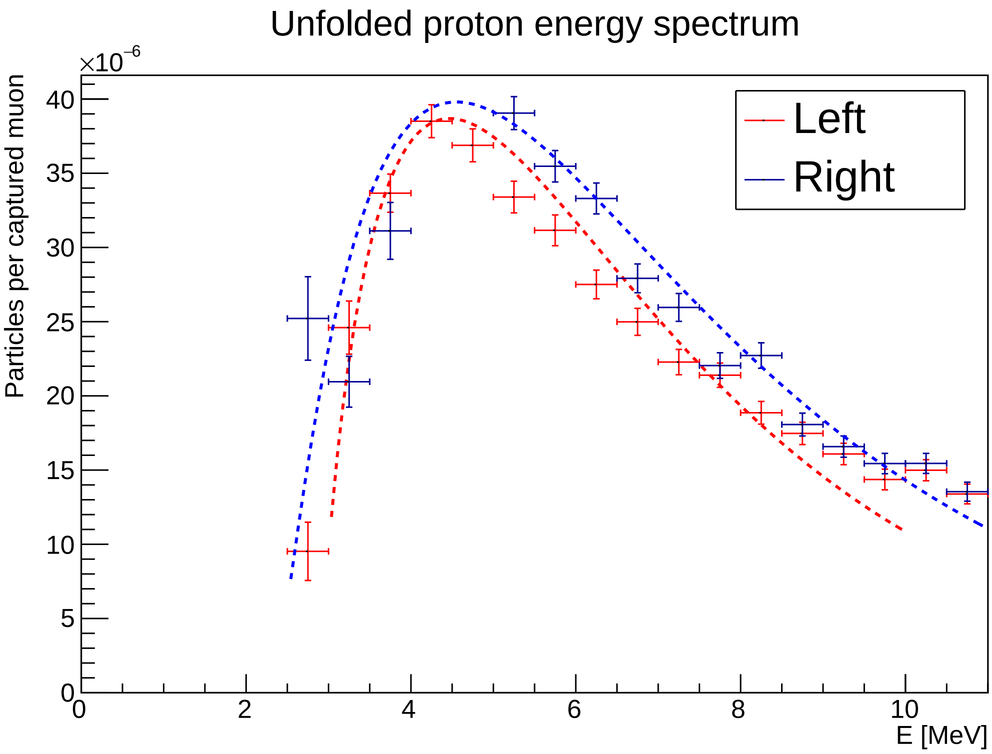

Figure 6.1: Left and right counter proton energy spectrum together with fitting.

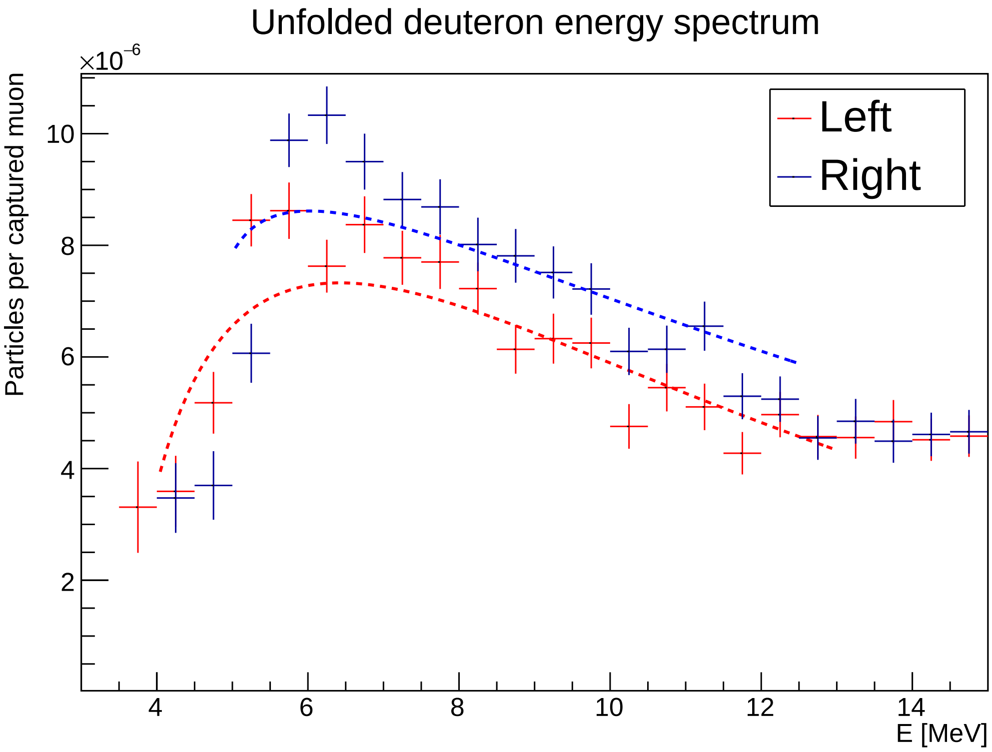

Figure 6.2: Left and right counter deuteron energy spectrum together with fitting.

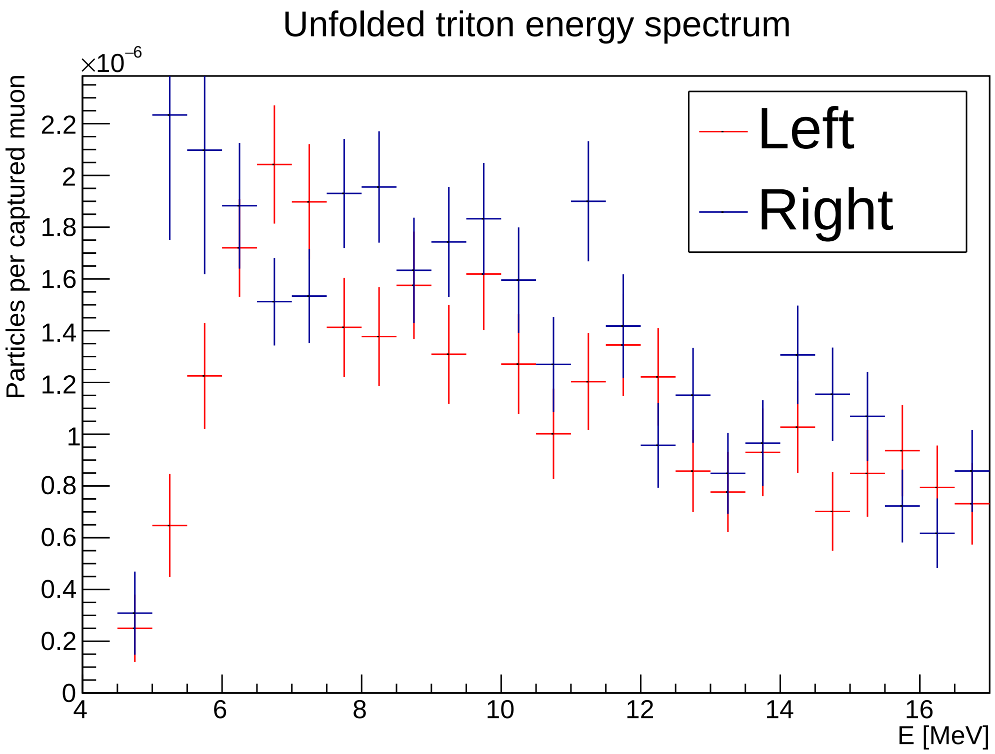

Figure 6.3: Left and right counter triton energy spectrum. The statistics were too low for fitting to work.

Particle	Left counter	Right counter
proton	24218(277)	27764(324)
deuteron	5491(117)	6018(114)
triton	1038(44)	1287(60)

Table 6.2: Total charged particle emission estimated from particles detected from the left and right detectors. We consider the rate of muon nuclear capture to be 60.9% and from there the number of muons captured in the Al100 dataset is 6.33×10^7. The left and right counter telescopes are not exactly the same distance apart.

and respectively for the left counter, R_{left} =137.1 mm and the total surface area of a silicon detector, $A = 2500\text{mm}^2$.

The whole procedure is repeated for neural network unfolding. The number for protons is different from the Bayesian method but it is within systematic errors.

6.1.1 Comparison with R2013 results

Figure.6.4 shows the comparison between current and previous results. The results largely agree in the energy bins after 4 MeV.

6.2 Systematic errors

Systematic error is estimated to be about 4.0%.

Particle	Left counter	Right counter
proton	3.53(0.07)	3.14(0.06)
deuteron	0.80(0.02)	0.68(0.02)
triton	0.15(0.01)	0.15(0.01)

Table 6.3: Charged particle emission rates per captured muon using the Bayesian method.

Particle	Left counter [%]	Right counter [%]
proton	2.18(0.04)	1.63(0.03)
deuteron	0.59(0.01)	0.48(0.01)
triton	0.17(0.01)	0.13(0.01)

Table 6.4: Charged particle emission rates per captured muon using the neural network method.

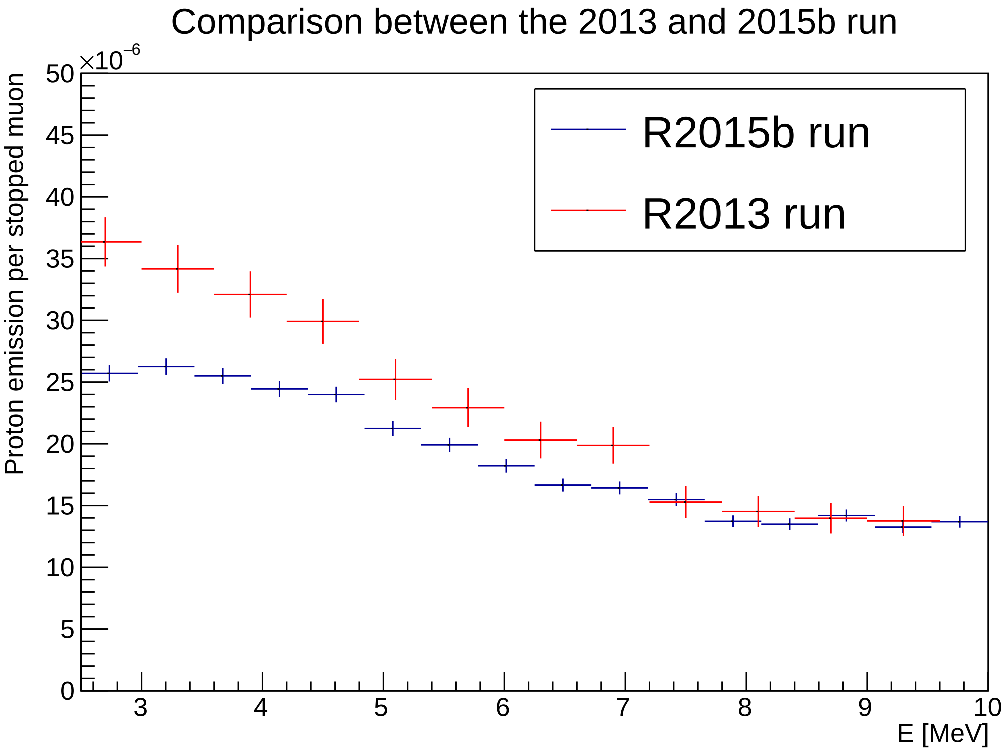

Figure 6.4: Comparison between the R2013 and R2105b proton energy spectrum.

Sources	Value
Stopped muon count	1.9%
Unfolding	2.6%
Particle misidentification	2%
Detector nonlinearity	1%
Pion contamination	0.4%
Lead contamination	0.3%
Pileup	0.1%

Table 6.5: Summary of systematic errors

6.2.1 Stopped muon count

One major contribution to the uncertainty may come from the choice of choose the time cuts for reducing semiprompt photons in the germanium energy spectra. Currently the time cut used is $-200 < t < 200$s where it retains 98% of counts. The prompt photons are gaussian distributed so using the properties of the gaussian distribution centered at zero with a σ =84 ns we may increase up to 99.7% of photons detected in the prompt spectra at the expense of also including some semiprompt photons. This can be done by setting $t < |3\sigma|$. Likewise, we could reduce the semiprompt contributions by selecting a cut with $t < |2\sigma|$, but we lose much more prompt photons, about 7% off from the current time cut of 200 ns. Therefore the germanium time cut systematics is estimated to be 1.7%.

The muons are optimized to stop in the center of the muon stopping target, therefore photons would also be required to traverse at most 100 μm of material to reach the vacuum and possibly reach the germanium detector. The total attenuation coeffient for a 400MeV photon in aluminium is 0.029 cm^2/g and if we consider just muonic aluminium 2p-1s x-ray photon, about 0.2% of it will be attenuated, probably reabsorbed by the material, or scattered away.

6.2.2 Pion contamination

Negative pions may come into the vacuum chamber together with the muons from the beam line. They have a very short lifetime of 26 ns so it is expected that there is a negligible number of them actually contributing a significant amount of background. Using nonrelativistic calculations, It is estimated that only 0.4% of pions remain in the beam after traversing the total length of 16 m or about 160 ns if they have a momentum of approximately 35 MeV. Only 1% of negative pions that interact with a nucleus would actually cause an emission of a proton. They do form pionic atoms and decay into muons and muon neutrinos but this number should also be negligible.

6.2.3 Pileup and constant fraction time

A second pulse which piles up with an earlier one might produce a constant fraction time of earlier than actual as shown in Figure;6.5. The constant fraction algorithm starts at the peak and goes left in search for the time where it is 20% of the peak value but get that at a time which is 800 ns instead of 2200 ns if there is no pileup of the main peak. As a result, the time between thin and thick detector needs to be much more forgiving than it could have, as evidenced by the right counter telescope time. The thin left counter has a total count rate of $280s^{-1}$ and the measurement dead time is about 3 μs which gives a total pileup error of about 0.1%.

6.2.4 Nonlinearity and saturation

Germanium detector linear energy response is important when identifying peaks although there is some linearity in the low and high energy detection extremes. It is estimatied that the deviation from this linearity since a integral nonlinearity of more than 0.07% is equivalent to a energy measurement drifting of about 1 keV. Using a simple quadratic fit for the two germanium channels the difference between the calculated energy values at 511 keV are then less than 0.14 keV for the low gain

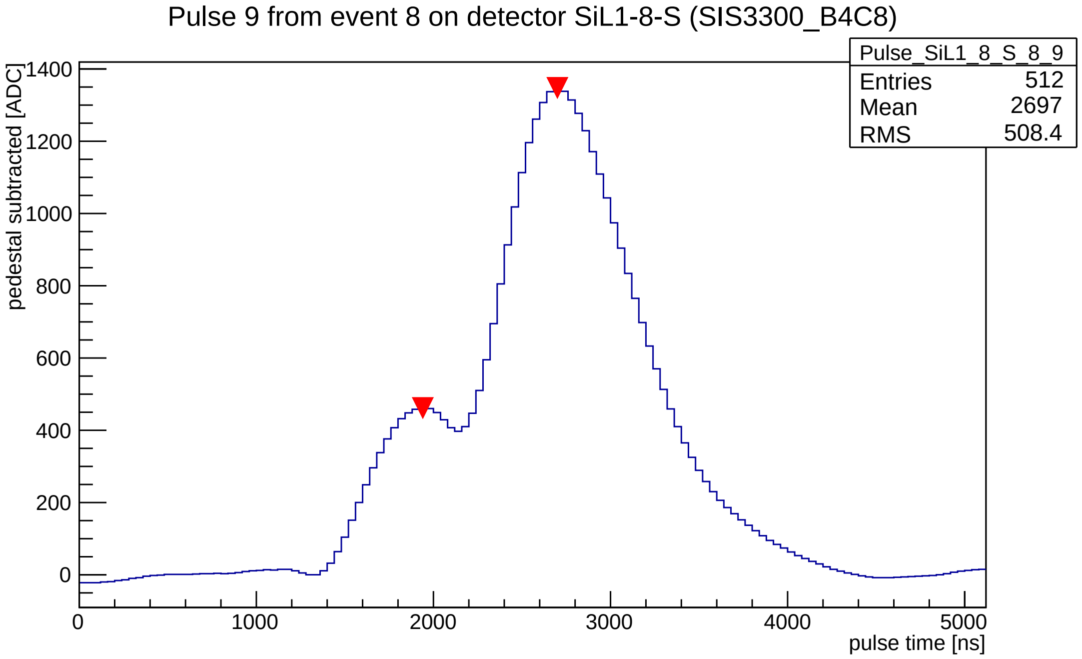

Figure 6.5: An example event in the left thin silicon where pileup between two pulses occurred.

channel and 0.001 keV for the high gain channel. This shows that the germanium detector is effectively linear in the energy regions of interest.

Silicon detectors display saturated pulses at energies more than 2 MeV. It is especially pronounced in the left counter telescope where the alpha band could not extend higher when it should be as compare to the right counter telescope. Hence, charged particles with less than 4.5 MeV energy would be measured less.

6.2.5 Lead and steel contamination

Lead is used as the primary background shielding in the vacuum chamber. Its primary purpose was to reduce muon scatters to the left and right counter telescope. This lead shield is placed between the entrance counter and detector regions, with a hole in the middle that allows muons passing through the entrance detector to reach the aluminium stopping targets shown in the picture in Figure.3.1. There is also shielding of the target mount. The target holder itself is also wrapped with lead and this is where charged particle emission from lead could occur. Muons from the beam can scatter off lead, producing x-rays and electrons in addition to getting captured and emitting neutrons and charged particles. Lead signature peaks can be seen in the germanium detector and properly taken account of but it is difficult to separate charged particles from lead in the counter telescopes. These charged particles contribute to the detector uncertainty. As a comparison, the capture rate, Λ_C of lead is $130 \times 10^5 s^{-1}$ compared to aluminium, $8.50 \times 10^5 s^{-1}$ is about 15 times more. From the germanium detector energy spectra, the number muons stopping in lead can be inferred since there are many lead peaks seen by the detector. It is expected that the lead contamination is limited as the muon beam is centered on the stopping target but there is some small percentage of 0.3% stopping in the lead shielding and mounting of the target. This number is obtained from Monte Carlo simulation. In the simulation, there was a collimator that helps to limit the beam size such that the muons mainly hit the aluminium target. But due to scattering of muons, this small percentage of muons are stopped in lead and x-ray peaks from lead are seen in the germanium detector.

6.2.6 Unfolding

During muon beam scans, stripped silicon detectors were used with strip sizes of 3.125 mm. There is therefore a measurement uncertainty due this is detector granularity. The muon stopping distribution might be between ±1.5625 of this value. Within this uncertainty range, the unfolded spectra maintains its spectral shape and the fluctuations should be minimal within the energy bins as shown in Figure.6.6. In the Monte Carlo simulation, the horizontal and vertical profile of the muon beam is varied, up to the maximum uncertainty values. Then an integral is taken and the total number of charged particles is tallied and compared with the central value. The first few bins have very high uncertainty since they start with much less statistics and unfolding requires more counts to provide good prediction of truth values. For energy bins near and higher than the peak value of 4.5 MeV, the change in the horizontal or vertical components of the muon beam profile in the simulation did not have much effect on the unfolding. This produces a slightly different response matrix that changes the results of unfolding.

The main contribution to systematic errors comes from this uncertainty of the Monte Carlo simulation. Slight changes in the muon beam parameters introduces much errors in the low statistics part of the energy spectra of the charged particles. These are typically in the lower energy regions below 3 MeV. Figure.6.6 show the stability of the spectral shape after varying the central value of the muon beam by 1 mm. This choice of 1 mm is still within the errors of the muon beam scan as the size of the strip is 3.125 mm. The total integral of the spectrum changes at maximum of about 2% when varied in this way. This accounts for the slight discrepancy between the unfolded data points for the left and right counters. Similar studies where done on the deuteron spectrum, and the maximum fluctuation from the central value is about 2.6%, which is shown in Figure.6.7.

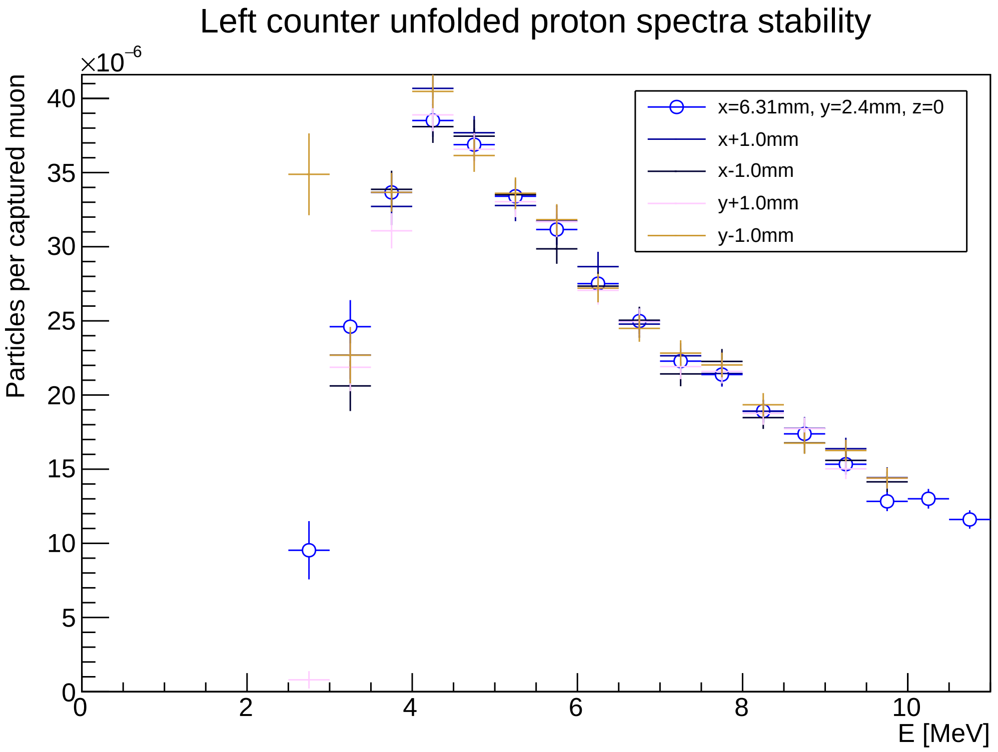

(a) Left counter telescope

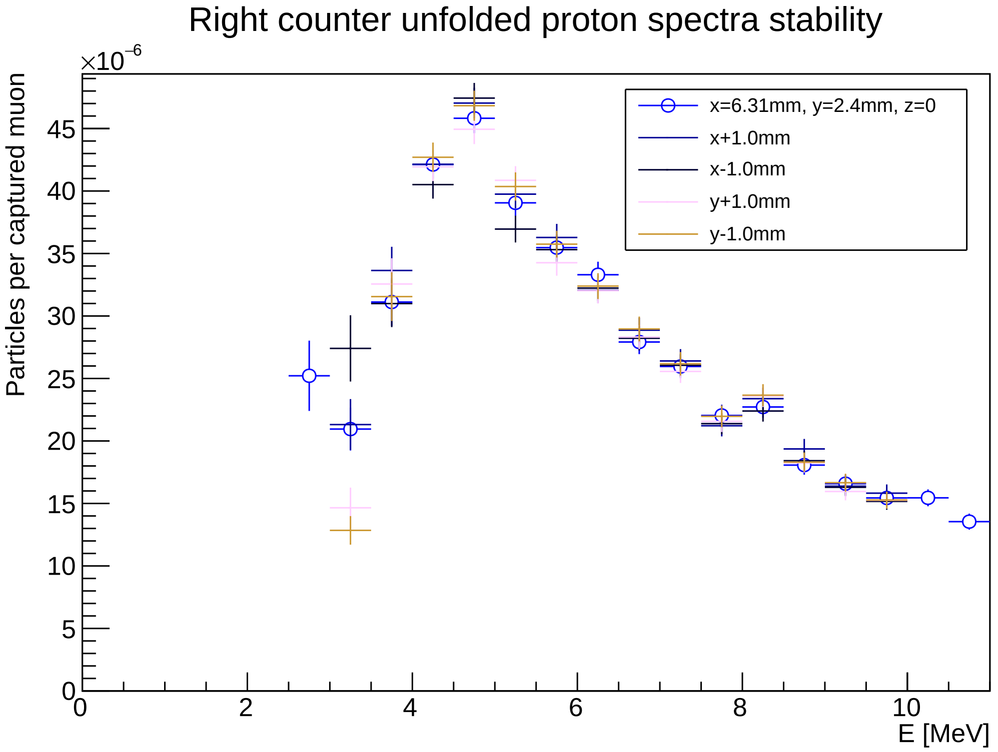

(b) Right counter telescope

Figure 6.6: Study of the stability of unfolded proton spectra with muon beam profile variations within uncertainty.

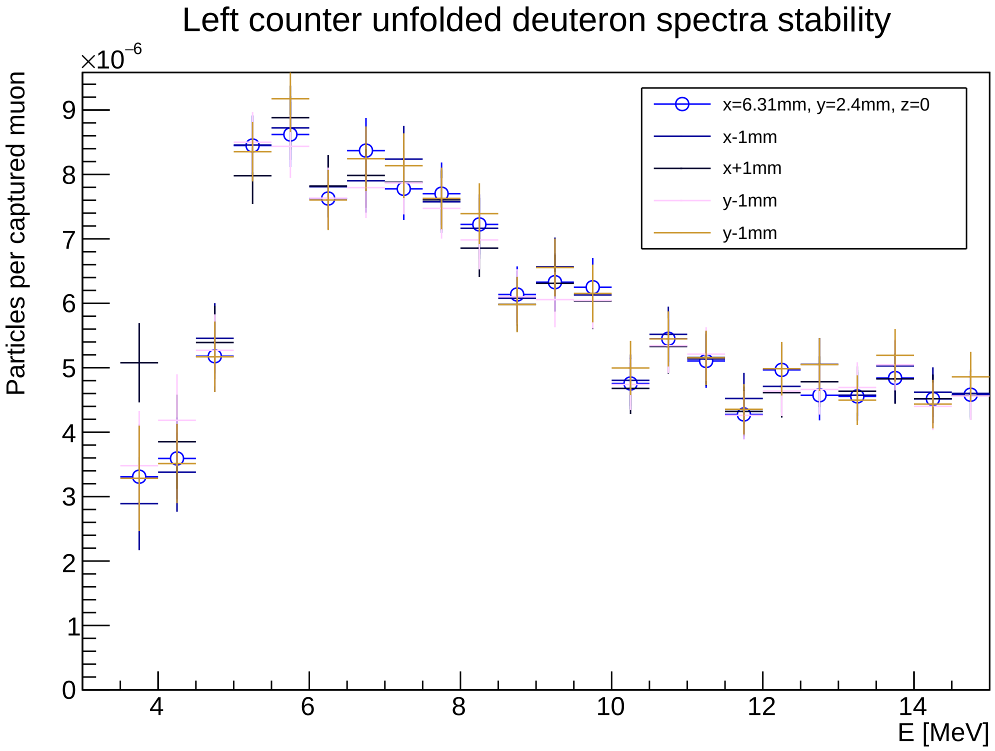

(a) Left counter telescope

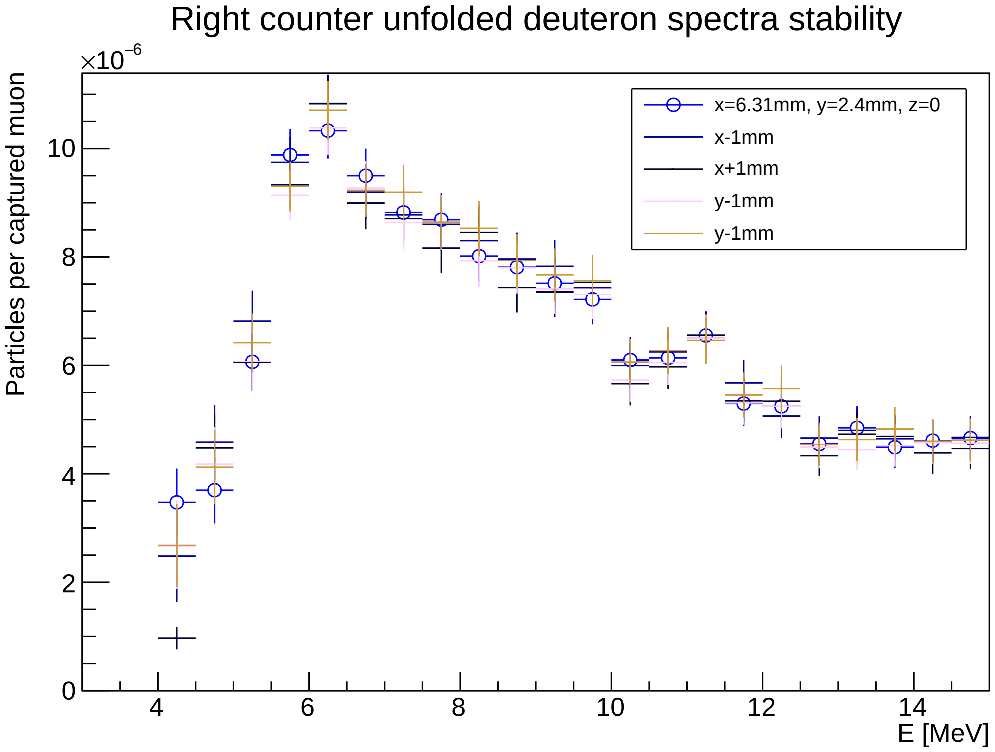

(b) Right counter telescope

Figure 6.7: Study of the stability of unfolded deuteron spectra with muon beam profile variations within uncertainty.

Chapter 7

Discussion

7.1 Nuclei identification

Figure.7.1 shows a compilation of the number of muons counted from different peaks measured by the germanium detector. In general, the x-ray peaks from muonic aluminium agree with each other to within errors. The errors however, are large in comparison to the 2p-1s peak.

AlCap R2015b also observed many peaks from neutron emission. Many peaks from ^{26}Mg nuclear excited state transitions to the ground state were identified and counted. This provided strong evidence that ^{26}Mg was formed and the way it was formed is somewhat hinted upon. The 1808keV and 1127keV transitions were seen and counted whereas the 1003keV and 2510keV were detected but could not be used for counting as they have lower intensity. Multiple lines from ^{27}Mg where also seen, which are the 983 keV, 1696 keV and 953 keV lines. They tell a story of ^{27}Mg forming at least up to the third nuclear excited state and that there are many being formed since the intensities of these gamma lines are in the order of a few percent only. It is consistent with the capture of muons in natural ^{27}Al which then transmutes into ^{27}Mg before emitting a neutron to form ^{26}Mg.

However, gamma rays from ^{26,25}Na were too weak and doppler shifted to be identified. It is expected that they should exist if charged particle emission occurs, for example if a proton is emitted after ^{27}Mg or ^{26}Mg forms, it should transmute into ^{26,25}Na. Granted, the rate of proton emission is much smaller than compared to neutron emission and the stronger sodium peaks are obscured by many background x-ray and gamma peaks as ^{26}Na has many lines under 1000 keV. The higher energy gamma peaks although having less lead background does suffer somewhat from doppler shifting, smearing out whatever visible bump that might appear. It would be helpful to be able to understand the mechanics of proton emission and precisely when in the reaction chain protons start to be emitted.

7.2 Charged particle rate and spectrum

In general, the unfolded spectra seen by the left and right counter telescopes show very good agreement with each other with the proton emission spectrum showing the best since it has collected the highest statistics. Equation.2.5 could be used to fit to this energy distribution with numbers in Table.6.1. The spectrum peaks around 4 MeV with a exponential decay parameter of 2.8 MeV which is a faster

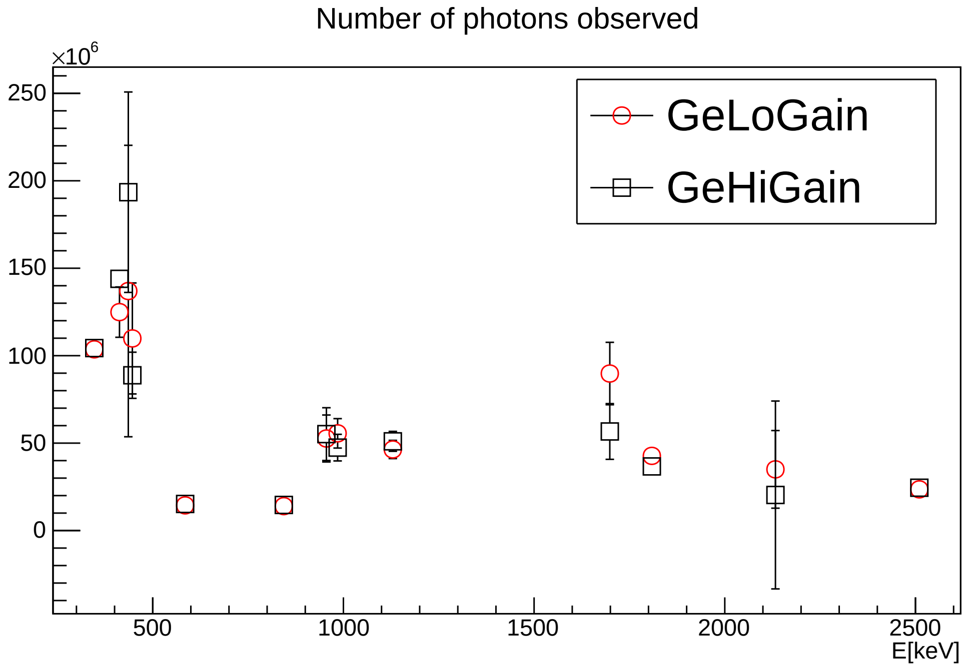

Figure 7.1: Summary of number of stopped muons obtained from the various peaks considered in the previous sections.

drop compared to the silicon result[32]. The energy range used in this run extended further to 10MeV so there were no reliance on the fit function but reproduced the result anyway. This further constrains the fit parameters and reduces the uncertainty for protons emitted at energies higher than 10 MeV. Hence a complementary muon normalization method could be developed for COMET that can work alongside other proposed methods like measurement of x-rays using germanium detectors.

It is instructive to model the proton emission half-life of ^{26}Mg which is the daughter nuclei after nuclear muon capture in ^{27}Al. The Q-value of proton emission from ^{26}Mg has a positive value so energetically, the process is favourable. In contrast to neutron emission, protons need to overcome the Coulomb barrier of the nucleus, so some idea of the height of the barrier is crucial to understanding the process of emission. Firstly, the nuclear separation between a proton and the ^{26}Mg nuclei, $R = 1.25(1^{1/3} + 25^{1/3}) = 4.91$fm is calculated. Assuming a Woods-Saxon[48] potential for the nuclear force, we have, together with the Coulomb potential, the barrier height is1.80 MeV. This barrier is sufficiently low such that the proton does not need to tunnel through as the energy transfer from muons typically provide up to 10 MeV. It explains the absence of protons below 2 MeV.

7.3 Neural network

A simple neural network was used in the particle identification and unfolding of the charged particle spectra but the results differ by about 20% from the more conventional Bayesian method used in the RooUnfold package. There is a possibility that the input nodes for the network were insufficient, however, adding more nodes such as time or germanium detector energy and time information might slow down

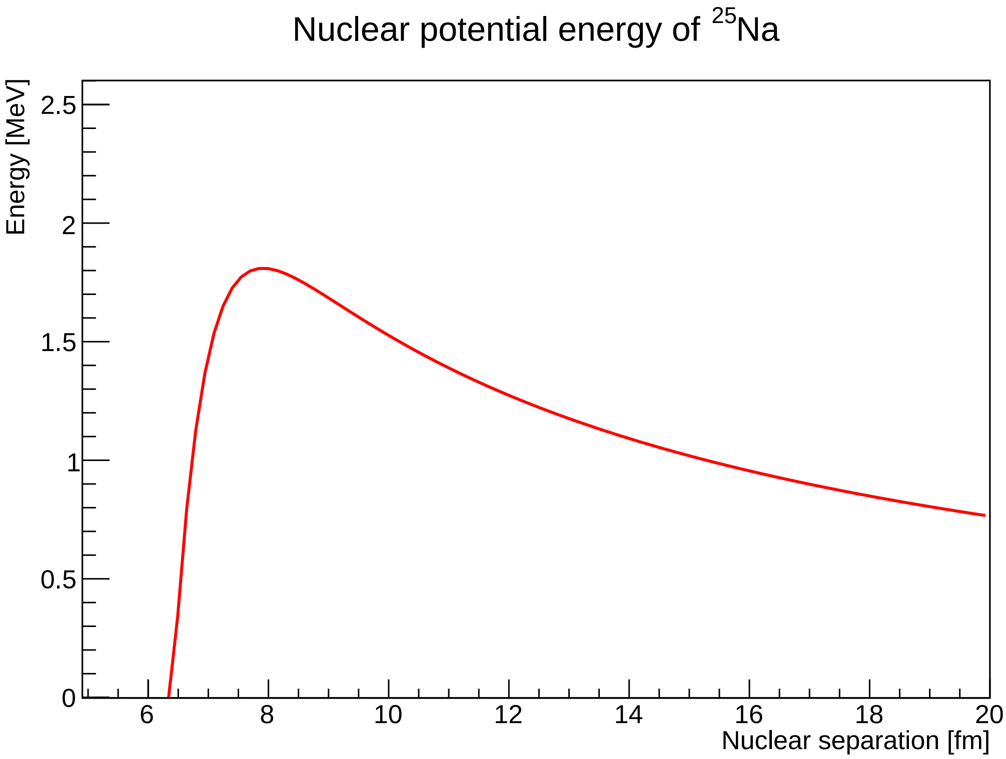

Figure 7.2: Nuclear potential energy using the Woods-Saxon nuclear strong interaction model and the Coulomb potential.

the training time significantly. In addition, since the choice of initial condition for the neural network is random, the output is at time different, but this problem can be mitigated by recording the weights and biases that had produced acceptable results. The results can then be reproduced.

7.4 Alternative muon normalization method for COMET

In the 2013 work, it has already been shown that the COMET CDC did not require additional absorbers to reduce the number of protons entering it. Therefore, after the 2015 run, better detector resolution and muon beam characterisation provided the opportunity to use the proton and possibly deuteron emission rates as another way of obtaining the muon stopping rates. This number can be used to complement existing methods for muon normalization which might included 2p-1s muonic x-ray, 1808keV gamma and DIO measurements.

7.4.1 Muon normalization with protons

The proton spectra from the previous chapter is used to update the monte carlo simulation physics list of ICEDUST, which is the main simulation framework of the COMET experiment. The idea is that we know the muon nuclear capture rate, 60.9% and the rate of proton or deuteron charged particle emission, we can use the CDC

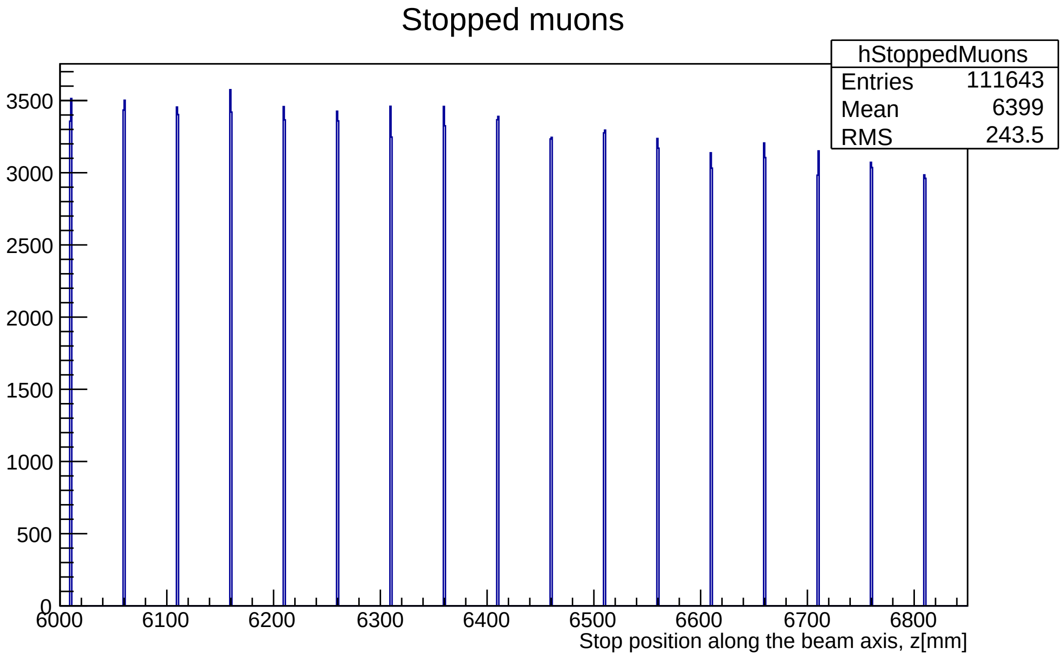

Figure 7.3: Stopped muon positions at the aluminium muon stopping targets in the middle of the COMET Phase-I CDC.

to count the number of protons after tracking and estimate the number of muons stopped in the aluminium muon stopping targets in the middle of the CDC. The CDC also has very large acceptance compared to semiconductor detectors. This can be an alternative method to the more straight forward x-ray measurement technique that can be done with a germanium detector or from counting reconstructed tracks of DIO electrons. The problem with using just the germanium detector is that the beam background radiation from neutrons and gamma rays may be too significant and difficult to reduce. This is in addition to braking radiation from beam electrons that creates a lot of x-ray photons since there are a lot of material in the detector and beamline that a total background determination may be very difficult. The geometrical acceptance of the germanium detector is also very small at about 1% if it is to be placed 3.5 m downstream from the center of the CDC. Figure.7.3 shows the stopping positions of the muons inside the aluminium stopping targets. These are candidate regions for proton emissions.

Extensive work has been done in the previous chapter where the unfolded charged particle spectra were obtained. Other charged particles like deuterons, tritons and alphas have much less chance to escape the muon stopping target as they might lose too much kinetic energy to scattering in the target itself.

7.4.2 Physics simulation framework

The COMET ICEDUST simulation is the common framework used by the COMET collaboration to generate Monte Carlo datasets. It contains beamline and detector construction that is being actively being developed and validated. The physics truth datasets are based on the GEANT4 framework but they do not have realistic models for low energy hadronic physics which is relevant to lepton conversion experiment such as COMET. For this purpose, the proton spectrum and emission rate obtained experimentally from AlCap can be used to update the physics such that the simulation can match the experiment much closer. In ICEDUST, the `G4HadronicInteraction` class inherited from `GEANT4` is overridden with the `COMETMuonMinusBoundDecayOrConversion` class which essentially updates the physics models for use in low energy physics experiments. The results from the AlCap experiment and theoretical work by Czarnecki[49] provides the physics basis for it.

The GEANT4 `G4HadronicInteraction` class was updated with the AlCap proton emission energy spectrum[50]. This modification is only relevant for muons stopping in an aluminium nuclei. If the muon stops in other nuclei, the default GEANT4 spectrum is used instead. Using ICEDUST simulated protons that are created in the target region, the Monte carlo truth energy spectrum is obtained.

If the magnetic field strength inside the CDC is assumed to be constant at 1 T, it is possible to estimate the momentum of the proton emitted from the muon stopping targets that would be sufficient to reach at least the first layer of the drift chamber. This minimum momentum is about 149.25 MeV if the proton is emitted right in the middle of a target. However, some protons would need more energy to travel to the first layers depending on the direction of emission. The upper limit to the detection efficiency, $\epsilon_{\text{detector}}$ of protons using the CDC is 0.262, where the estimation does not include the noise consideration, number of hit layers and also particle misidentification amongst other inefficiencies, Figure.7.4 shows protons tracks that originates from the muon stopping target. This number is in addition to the low proton emission rate of 3.5% per stopped muon.

The COMET Phase-I proton beam current is $0.4\,\mu$A or 2.5×10^{12}Hz. Hence, the accumulated time for a possible measurement of the 100 proton tracks as shown in Figure.7.4 is $16\,\mu$s, or seven protons in the time between beam spills. This is of course a time-averaged value but it is useful for estimating the hit occupancy of the CDC during the 700 ns measurement time window.

$$N_{\text{protons}} = N_{\mu} \cdot f_{\text{capture}} \cdot \epsilon_{\text{detector}} \cdot \epsilon_{\text{tracking}} \tag{7.1}$$

From Equation.7.1 the number of stopped muons, N_{μ}, is inferred. The tracking efficiency, $\epsilon_{\text{tracking}}$ is estimated to be the same as the tracking efficiency for signal electrons. One of the major background to this measurement is from beam pions that stop in the target which is about 1% of the number of stopped muons. Pions may interact with neutrons in the nuclei and emit protons, these protons might contribute to the proton measurement background however, this number is negligible and perhaps smaller than other systematic contributions.

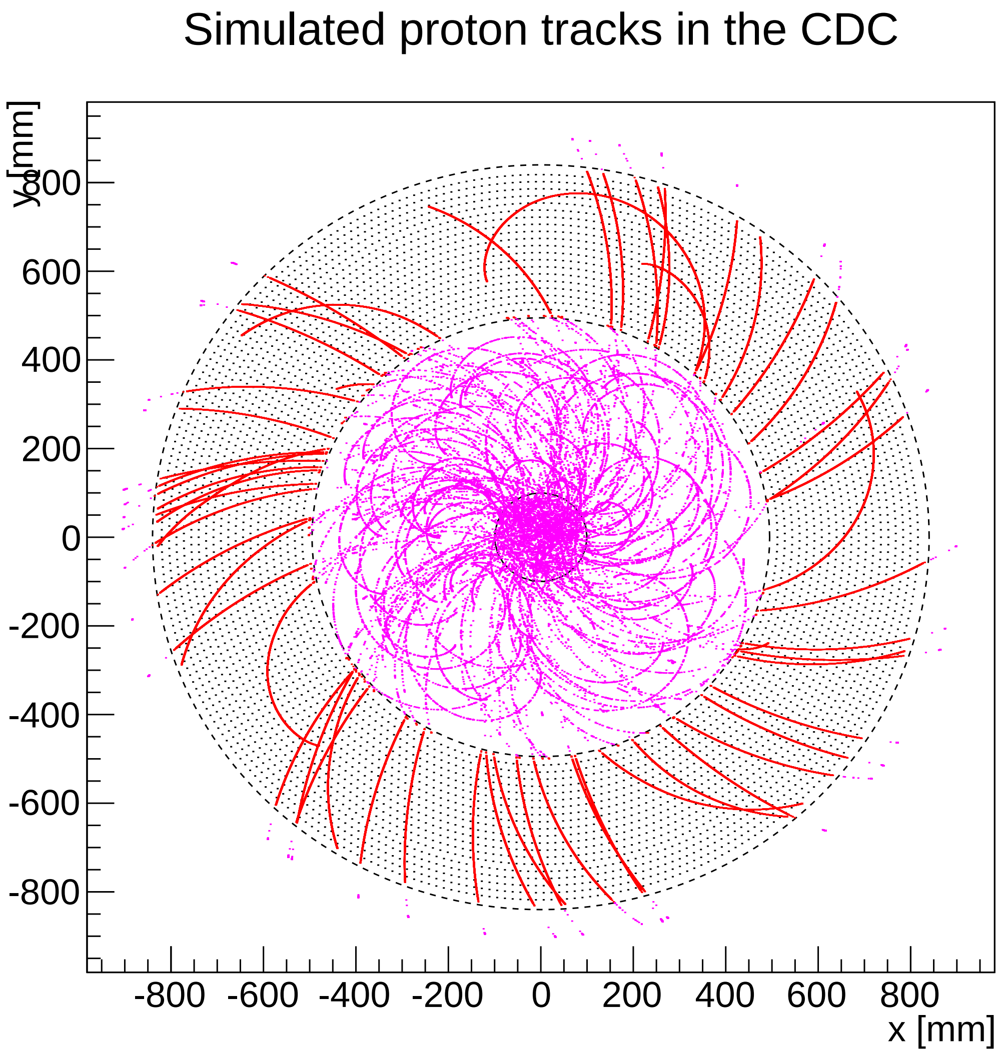

(a) Perpendicular to the beam

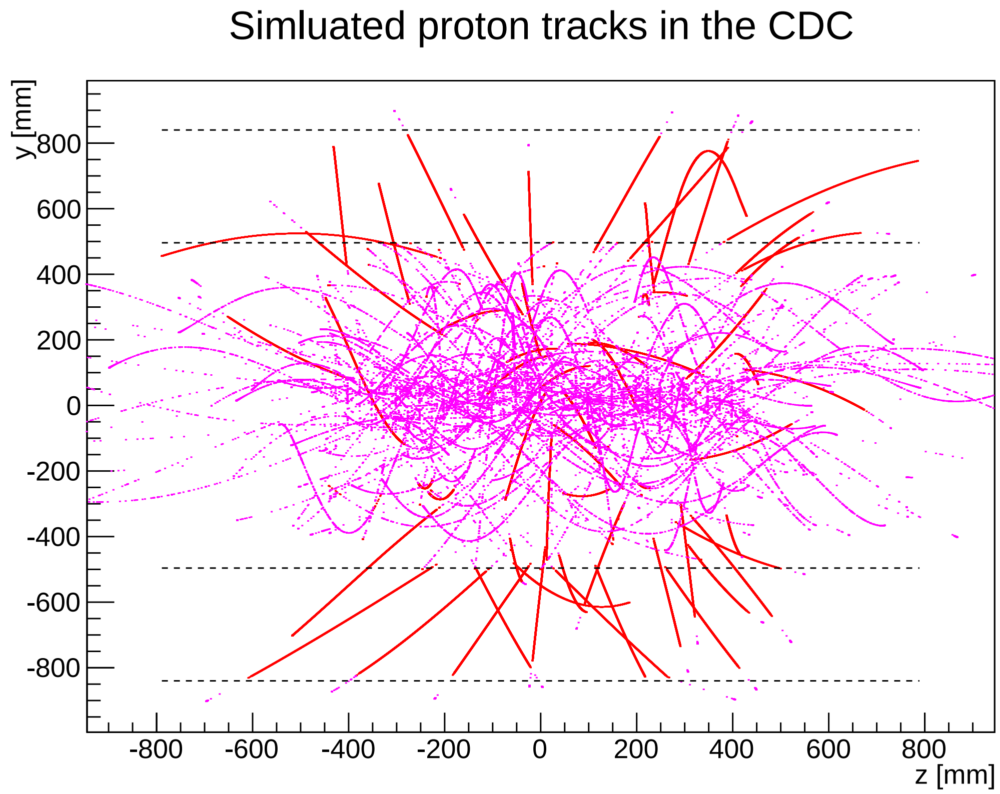

(b) Along the beam axis

Chapter 8

Conclusions

The AlCap experiment performed at PSI measured charged particle emission rates and explored muon normalization methods. These measurements are important in understanding the intrinsic physics backgrounds in modern muon to electron conversion experiments. The R2015b run took place in PSI with the aim of bettering the measurement obtained previously. The experiment stopped a total of 1.04×10^8 muons, an improvement from an earlier run. Various muonic x-ray and nuclear capture gamma transitions were observed but the muonic x-ray 2p-1s transition still has the lowest uncertainty and therefore still the ideal muon normalization method. The other x-ray and gamma peaks from aluminium and magnesium was also evaluated. Different methods for particle band selection and unfolding were used, namely the Bayesian method and neural network methods. The Bayesian method reproduced R2013 results but the neural network method had about a 20% discrepancy.

The charged particle emission rates after nuclear muon capture using the Bayesian method are

- protons $3.33 \pm 0.20\%$
- deuterons $0.74 \pm 0.05\%$
- tritons $0.15 \pm 0.02\%$

Using the proton spectra and rates, it is possible to suggest a new way for muon normalization for the COMET Phase-I experiment. The proton detection rate assuming no inefficiencies in track reconstruction and detector noise is about 0.5% for each muon stopped. This method is immune to beam flash that happens during every beam spill.

Nomenclature

ANN	Artificial neural network
BFGS	Broyden-Fletcher-Golfarb-Shanno
BSM	Beyond Standard Model
CDC	Cylindrical Drift Chamber
CLFV	Charged Lepton Flavor Violation
COMET	COherent Muon to Electron Transition
CyDet	Cylindrical Detector
DIO	Decay In Orbit
FWHM	full width at half maximum
GUT	Grand Unified Theories
J-PARC	Japan Proton Accelerator Research Complex
LHC	Large Hadron Collider
ODB	Online Database
POT	Protons On Target
ReLu	Restricted linear unit
RMD	Radiative Muon Decay
SES	Single Event Sensitivity
SM	Standard Model
SUSY	Supersymmetry
TAP	TAnalysedPulses
TPI	TPulseIslands

Bibliography

[1] Yu. Budyashov, V. G. G. Zinov, A. D. Konin, A. I. Mukhin, and A. M. Chatrchyan. Charged particles from the capture of negative muons by the nuclei 28si, 32s, 40ca, and 64cu. *JETP*, 33:11, 1971.

[2] Nam Hoai Tran. *A study of proton emission following nuclear muon capture for the COMET experiment*. PhD thesis, Osaka University, 2014.

[3] A. Wyttenbach *et al.* Probabilities of Muon Induced Nuclear Reactions Involving Charged Particle Emission. *Nucl. Phys. A*, 294:278–292, 1978.

[4] D. Measday. The nuclear physics of muon capture. *Phys. Rept.*, 354:243–409, 2001.

[5] Y. Fukuda, T. Hayakawa, E. Ichihara, K. Inoue, K. Ishihara, H. Ishino, Y. Itow, T. Kajita, J. Kameda, S. Kasuga, K. Kobayashi, Y. Kobayashi, Y. Koshio, M. Miura, M. Nakahata, S. Nakayama, A. Okada, K. Okumura, N. Sakurai, M. Shiozawa, Y. Suzuki, Y. Takeuchi, Y. Totsuka, S. Yamada, M. Earl, A. Habig, E. Kearns, M. D. Messier, K. Scholberg, J. L. Stone, L. R. Sulak, C. W. Walter, M. Goldhaber, T. Barszczxak, D. Casper, W. Gajewski, P. G. Halverson, J. Hsu, W. R. Kropp, L. R. Price, F. Reines, M. Smy, H. W. Sobel, M. R. Vagins, K. S. Ganezer, W. E. Keig, R. W. Ellsworth, S. Tasaka, J. W. Flanagan, A. Kibayashi, J. G. Learned, S. Matsuno, V. J. Stenger, D. Takemori, T. Ishii, J. Kanzaki, T. Kobayashi, S. Mine, K. Nakamura, K. Nishikawa, Y. Oyama, A. Sakai, M. Sakuda, O. Sasaki, S. Echigo, M. Kohama, A. T. Suzuki, T. J. Haines, E. Blaufuss, B. K. Kim, R. Sanford, R. Svoboda, M. L. Chen, Z. Conner, J. A. Goodman, G. W. Sullivan, J. Hill, C. K. Jung, K. Martens, C. Mauger, C. McGrew, E. Sharkey, B. Viren, C. Yanagisawa, W. Doki, K. Miyano, H. Okazawa, C. Saji, M. Takahata, Y. Nagashima, M. Takita, T. Yamaguchi, M. Yoshida, S. B. Kim, M. Etoh, K. Fujita, A. Hasegawa, T. Hasegawa, S. Hatakeyama, T. Iwamoto, M. Koga, T. Maruyama, H. Ogawa, J. Shirai, A. Suzuki, F. Tsushima, M. Koshiba, M. Nemoto, K. Nishijima, T. Futagami, Y. Hayato, Y. Kanaya, K. Kaneyuki, Y. Watanabe, D. Kielczewska, R. A. Doyle, J. S. George, A. L. Stachyra, L. L. Wai, R. J. Wilkes, and K. K. Young. Evidence for oscillation of atmospheric neutrinos. *Phys. Rev. Lett.*, 81:1562–1567, Aug 1998.

[6] William J. Marciano, Toshinori Mori, and J. Michael Roney. Charged lepton flavor violation experiments. *Annual Review of Nuclear and Particle Science*, 58(1):315–341, 2008.

[7] L. Calibbi, A. Faccia, A. Masiero, and S. K. Vempati. Lepton flavor violation from supersymmetric grand unified theories: Where do we stand for meg, prism/prime, and a super flavor factory. *Phys. Rev. D*, 74:116002, Dec 2006.

[8] A. de Gouvêa. (charged) lepton flavor violation. *Nuclear Physics B - Proceedings Supplements*, 188(Supplement C):303 – 308, 2009. Proceedings of the Neutrino Oscillation Workshop.

[9] W. Bertl, R. Engfer, E.A. Hermes, G. Kurz, T. Kozlowski, J. Kuth, G. Otter, F. Rosenbaum, N.M. Ryskulov, A. van der Schaaf, P. Wintz, and I. Zychor. A search for μ-e conversion in muonic gold. *The European Physical Journal C - Particles and Fields*, 47(2):337–346, Aug 2006.

[10] G. Feinberg, P. Kabir, and S. Weinberg. Transformation of muons into electrons. *Phys. Rev. Lett.*, 3:527–530, Dec 1959.

[11] G. Danby, J-M. Gaillard, K. Goulianos, L. M. Lederman, N. Mistry, M. Schwartz, and J. Steinberger. Observation of high-energy neutrino reactions and the existence of two kinds of neutrinos. *Phys. Rev. Lett.*, 9:36–44, Jul 1962.

[12] A. M. Baldini, Y. Bao, E. Baracchini, C. Bemporad, F. Berg, M. Biasotti, G. Boca, M. Cascella, P. W. Cattaneo, G. Cavoto, F. Cei, C. Cerri, G. Chiarello, C. Chiri, A. Corvaglia, A. de Bari, M. De Gerone, T. Doke, A. D'Onofrio, S. Dussoni, J. Egger, Y. Fujii, L. Galli, F. Gatti, F. Grancagnolo, M. Grassi, A. Graziosi, D. N. Grigoriev, T. Haruyama, M. Hildebrandt, Z. Hodge, K. Ieki, F. Ignatov, T. Iwamoto, D. Kaneko, T. I. Kang, P.-R. Kettle, B. I. Khazin, N. Khomutov, A. Korenchenko, N. Kravchuk, G. M. A. Lim, A. Maki, S. Mihara, W. Molzon, Toshinori Mori, F. Morsani, A. Mtchedilishvili, D. Mzavia, S. Nakaura, R. Nardò, D. Nicolò, H. Nishiguchi, M. Nishimura, S. Ogawa, W. Ootani, S. Orito, M. Panareo, A. Papa, R. Pazzi, A. Pepino, G. Piredda, G. Pizzigoni, A. Popov, F. Raffaelli, F. Renga, E. Ripiccini, S. Ritt, M. Rossella, G. Rutar, R. Sawada, F. Sergiampietri, G. Signorelli, M. Simonetta, G. F. Tassielli, F. Tenchini, Y. Uchiyama, M. Venturini, C. Voena, A. Yamamoto, K. Yoshida, Z. You, Yu. V. Yudin, and D. Zanello. Search for the lepton flavour violating decay $\mu^+ \to e^+\gamma$ with the full dataset of the meg experiment. *The European Physical Journal C*, 76(8):434, Aug 2016.

[13] H.C. Chiang, E. Oset, T.S. Kosmas, Amand Faessler, and J.D. Vergados. Coherent and incoherent (μ^-, e^-) conversion in nuclei. *Nuclear Physics A*, 559(4):526 – 542, 1993.

[14] E. Fermi and E. Teller. The capture of negative mesotrons in matter. *Phys. Rev.*, 72:399–408, Sep 1947.

[15] T. Suzuki, D.F. Measday, and J. P. Roalsvig. Total nuclear capture rates for negative muons. *Phys. Rev. C*, 35, 1986.

[16] J. L. Lathrop, R. A. Lundy, V. L. Telegdi, R. Winston, and D. D. Yovanovitch. Measurements of muon disappearance rates vs time in c, mg, al, si, and p. *Phys. Rev. Lett.*, 7:107–109, Aug 1961.

[17] Robert W Huff. Decay rate of bound muons. *Annals of Physics*, 16(2):288 – 317, 1961.

[18] H. PRIMAKOFF. Theory of muon capture. *Rev. Mod. Phys.*, 31:802–822, Jul 1959.

[19] Kenneth W. Ford and John G. Wills. Muonic atoms and the radial shape of the nuclear charge distribution. *Phys. Rev.*, 185:1429–1438, Sep 1969.

[20] T.A. Filippas, P. Palit, R.T. Siegel, and R.E. Welsh. Negative muon capture rates in high-z elements. *Physics Letters*, 6(1):118 – 120, 1963.

[21] K.P. Jackson, C.U. Cardinal, H.C. Evans, N.A. Jelley, and J. Cerny. $^{53}\mathrm{co}^{m}$: A proton-unstable isomer. *Physics Letters B*, 33(4):281 – 283, 1970.

[22] S. Hofmann, W. Reisdorf, G. Münzenberg, F. P. Heßberger, J. R. H. Schneider, and P. Armbruster. Proton radioactivity of151lu. *Zeitschrift für Physik A Atoms and Nuclei*, 305(2):111–123, Jun 1982.

[23] O. Klepper, T. Batsch, S. Hofmann, R. Kirchner, W. Kurcewicz, W. Reisdorf, E. Roeckl, D. Schardt, and G. Nyman. Direct and beta-delayed proton decay of very neutron-deficient rare-earth isotopes produced in the reaction58ni+92mo. *Zeitschrift für Physik A Atoms and Nuclei*, 305(2):125–130, Jun 1982.

[24] S. M. Grimes, R. C. Haight, and J. D. Anderson. Measurement of sub-coulomb-barrier charged particles emitted from aluminum and titanium bombarded by 15-mev neutrons. *Nuclear Science and Engineering*, 62(2):187–194, 1977.

[25] S. M. Grimes, R. C. Haight, K. R. Alvar, H. H. Barschall, and R. R. Borchers. Charged-particle emission in reactions of 15-mev neutrons with isotopes of chromium, iron, nickel, and copper. *Phys. Rev. C*, 19:2127–2137, Jun 1979.

[26] E. Maglione, L. S. Ferreira, and R. J. Liotta. Proton emission from deformed nuclei. *Phys. Rev. C*, 59:R589–R592, Feb 1999.

[27] V.I. Goldansky. On neutron-deficient isotopes of light nuclei and the phenomena of proton and two-proton radioactivity. *Nuclear Physics*, 19(Supplement C):482 – 495, 1960.

[28] M. Pfützner, E. Badura, C. Bingham, B. Blank, M. Chartier, H. Geissel, J. Giovinazzo, L.V. Grigorenko, R. Grzywacz, M. Hellström, Z. Janas, J. Kurcewicz, A.S. Lalleman, C. Mazzocchi, I. Mukha, G. Münzenberg, C. Plettner, E. Roeckl, K.P. Rykaczewski, K. Schmidt, R.S. Simon, M. Stanoiu, and J.-C. Thomas. First evidence for the two-proton decay of 45fe. *The European Physical Journal A - Hadrons and Nuclei*, 14(3):279–285, Jul 2002.

[29] J. Giovinazzo, B. Blank, M. Chartier, S. Czajkowski, A. Fleury, M. J. Lopez Jimenez, M. S. Pravikoff, J.-C. Thomas, F. de Oliveira Santos, M. Lewitowicz, V. Maslov, M. Stanoiu, R. Grzywacz, M. Pfützner, C. Borcea, and B. A. Brown. Two-proton radioactivity of $^{45}\mathrm{Fe}$. *Phys. Rev. Lett.*, 89:102501, Aug 2002.

[30] B. Blank, A. Bey, G. Canchel, C. Dossat, A. Fleury, J. Giovinazzo, I. Matea, N. Adimi, F. De Oliveira, I. Stefan, G. Georgiev, S. Grévy, J. C. Thomas, C. Borcea, D. Cortina, M. Caamano, M. Stanoiu, F. Aksouh, B. A. Brown, F. C. Barker, and W. A. Richter. First observation of ^{54}Zn and its decay by two-proton emission. *Phys. Rev. Lett.*, 94:232501, Jun 2005.

[31] H. Morinaga and W.F. Fry. Nuclear capture of negative μ mesons in photographic emulsions. *Il Nuovo Cimento*, 10(3):308–318, 1953.

[32] S. Sobottka and E. Wills. Energy Spectrum of Charged Particles Emitted Following Muon Capture in Si^{28}. *Phys. Rev. Lett.*, 20:596–598, 1968.

[33] K. S. Krane, T. C. Sharma, L. W. Swenson, D. K. McDaniels, P. Varghese, B. E. Wood, R. R. Silbar, H. D. Wohlfahrt, and C. A. Goulding. Energetic charged-particle spectrum following μ^- capture by nuclei. *Phys. Rev. C*, 20:1873–1877, Nov 1979.

[34] Chikai Ishii. An Analysis of the Charged Particles Emitted Following Negative Muon Absorptions in Photographic Emulsions. *Progress of Theoretical Physics*, 21(5):663–675, may 1959.

[35] Paul Singer. Nuclear surface effects in muon capture. *Phys. Rev.*, 124:1602–1609, Dec 1961.

[36] A. W. J. Edmonds. *An Estimate of the Hadron Production Uncertainty and a Measurement of the Rate of Proton Emission after Nuclear Muon Capture for the COMET Experiment.* PhD thesis, UCL (University College London), 2015.

[37] L.A. Schaller, T. Dubler, K. Kaeser, G.A. Rinker, B. Robert-Tissot, L. Schellenberg, and H. Schneuwly. Nuclear charge radii from muonic x-ray transitions in f, na, al, si, p, s and k. *Nuclear Physics A*, 300(2):225 – 234, 1978.

[38] W. Wagner, M. Seidel, E. Morenzoni, F. Groeschel, M. Wohlmuther, and M. Daum. Psi status 2008—developments at the 590mev proton accelerator facility. *Nuclear Instruments and Methods in Physics Research Section A: Accelerators, Spectrometers, Detectors and Associated Equipment*, 600(1):5 – 7, 2009.

[39] F. Foroughli. πe1 secondary beam line. *PSI Technical note*, 1997.

[40] Design, commissioning and performance of the pibeta detector at psi. *Nuclear Instruments and Methods in Physics Research Section A: Accelerators, Spectrometers, Detectors and Associated Equipment*, 526(3):300 – 347, 2004.

[41] U. Fano. Ionization yield of radiations. ii. the fluctuations of the number of ions. *Phys. Rev.*, 72:26–29, Jul 1947.

[42] B.G. Lowe. Measurements of fano factors in silicon and germanium in the low-energy x-ray region. *Nuclear Instruments and Methods in Physics Research Section A: Accelerators, Spectrometers, Detectors and Associated Equipment*, 399(2):354 – 364, 1997.

[43] V. Tishchenko, S. Battu, S. Cheekatmalla, D.B. Chitwood, S. Dhamija, T.P. Gorringe, F. Gray, K.R. Lynch, I. Logashenko, S. Rath, and D.M. Webber. Data acquisition system for the mulan muon lifetime experiment. *Nuclear Instruments and Methods in Physics Research Section A: Accelerators, Spectrometers, Detectors and Associated Equipment*, 592(1):114 – 122, 2008.

[44] Tim Adye. Unfolding algorithms and tests using RooUnfold. (arXiv:1105.1160):313–318. 6 p, May 2011. Comments: 6 pages, 5 figures, presented at PHYSTAT 2011, CERN, Geneva, Switzerland, January 2011, to be published in a CERN Yellow Report.

[45] Hermann Kolanoski. Application of artificial neural networks in particle physics. *Nuclear Instruments and Methods in Physics Research Section A: Accelerators, Spectrometers, Detectors and Associated Equipment*, 367(1):14 – 20, 1995. Proceedings of the 7th International Wire Chamber Conference.

[46] R. Koohi-Fayegh, S. Green, N.M.J. Crout, G.C Taylor, and M.C. Scott. Neural network unfolding of photon and neutron spectra using an ne-213 scintillation detector. *Nuclear Instruments and Methods in Physics Research Section A: Accelerators, Spectrometers, Detectors and Associated Equipment*, 329(1):269 – 276, 1993.

[47] J.L. Flores, I. Martel, R. Jiménez, J. Galán, and P. Salmerón. Application of neural networks to digital pulse shape analysis for an array of silicon strip detectors. *Nuclear Instruments and Methods in Physics Research Section A: Accelerators, Spectrometers, Detectors and Associated Equipment*, 830(Supplement C):287 – 293, 2016.

[48] Roger D. Woods and David S. Saxon. Diffuse surface optical model for nucleon-nuclei scattering. *Phys. Rev.*, 95:577–578, Jul 1954.

[49] A. Czarnecki, et al. *Phys. Rev. D*, 85:025018, 2012.

[50] Benjamin Edward Kriker. *Sensitivity and background estimates for phase-II of the COMET experiment.* PhD thesis, Imperial College London, 2017.